

THESIS

TIP VORTEX AND CRENUATION
EFFECTS IN A COMPRESSOR
CASCADE WITH MOVING ENDWALL

Barry W. St. Germain
Captain, USAF

AFIT/GAE/ENY/99M-02

DTIC QUALITY INSPECTED 2

19990409 059

The views expressed in this thesis are those of the author and do not reflect the official policy or position of the Department of Defense or the U.S. Government.

AFIT/GAE/ENY/99M-02

TIP VORTEX AND CRENULATION EFFECTS
IN A COMPRESSOR CASCADE WITH MOVING ENDWALL

THESIS

Presented to the Faculty of the Graduate School of Engineering
of the Air Force Institute of Technology
Air University
In Partial Fulfillment of the
Requirements for the Degree of
Master of Science in Aeronautical Engineering

Barry St. Germain

Captain, USAF

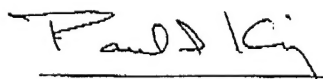
March 1999

Approved for public release; distribution unlimited

TIP VORTEX AND CRENULATION EFFECTS
IN A COMPRESSOR CASCADE WITH MOVING ENDWALL

Barry St. Germain, B.S., M.A.S.
Captain, USAF

Approved:



Paul I. King (Committee Chairman)

4 Feb 99

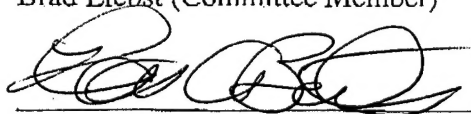
date



Brad Liebster (Committee Member)

4 FEB 99

date



Thomas Butler, LtC USAF
(Committee member)

4 Feb 99

date

Acknowledgments

This thesis is the final product of a long period of hard work. Without the help of a large number of people, I would have never been able to complete this project. I would like to take this opportunity to thank everyone involved in this research thesis.

I want to thank Dr Paul I. King for the tremendous aid he provided during the course of this thesis. His inputs and experience were crucial to the final outcome and helped keep me focused on the important objectives of my research. Also worthy of the task were Dr Brad Liebst and LtC (Dr) Jeff Little, whose advice and constructive criticisms enabled me to write a proper report of my research. Special mention goes to LtC Tom Buter who was there every step of the way.

The AFIT laboratory technicians Mr. Jay Anderson, Mr. Andrew Pitts, Mr. Charles McNeely, Mr. Daniel Rioux, and Mr. Mark Deriso were very helpful. My special thanks goes to Mr. McNeely, whose computer expertise aided greatly in re-writing the wind tunnel data acquisition software.

Without a doubt, my greatest thanks goes to my family. My wife, Jacqueline was always understanding although taking care of year-old twins made AFIT look like a cakewalk. The value of children is that Maria and Spencer will always be able to show me what is truly important in life.

Thank you all,

Barry St. Germain

Table of Contents

	Page
Acknowledgments.....	ii
List of Figures.....	vi
List of Tables	ix
List of Symbols.....	x
Abstract.....	xv
I. Introduction.....	1-1
Background.....	1-1
Summary of Previous Research.....	1-1
Objective.....	1-3
II. Flow Description.....	2-1
Flowfield in a Linear Cascade with Moving Endwall.....	2-1
Compressor Cascade.....	2-1
Blade Crenulation Performance.....	2-2
Methods of Studying Crenulation Effects.....	2-3
Total Pressure Loss Coefficients.....	2-4
Turning Angle.....	2-6
III. Experimental Apparatus.....	3-1
Air Supply System.....	3-1
Settling Chamber.....	3-2
Test Section and Moving Wall Section.....	3-2
Data Acquisition System.....	3-5
Central Computer.....	3-5
Pressure Measurement Subsystem.....	3-5
Velocity and Temperature Measurement Subsystem.....	3-6
Probe Traverse Control.....	3-7

IV. Experimental Procedure.....	4-1
Hotwire Calibration.....	4-1
Hotwire Calibration Procedure.....	4-2
Calibration Verification.....	4-2
Pressure System Calibration.....	4-3
Data Acquisition.....	4-3
System Preparation.....	4-3
Tailboard Balancing.....	4-3
Pressure Collection.....	4-4
Temperature Collection.....	4-4
Probe Controller.....	4-4
Hotwire Data Collection.....	4-4
Total Pressure Rake Data Collection.....	4-5
Data Reduction.....	4-6
Hotwire Data Reduction.....	4-6
Total Pressure Rake Data Reduction.....	4-6
Error Analysis.....	4-7
Equipment and Instrumentation Accuracies.....	4-7
Estimated Error for the Pressure Loss Coefficient.....	4-7
V. Results and Discussion.....	5-1
Introduction.....	5-1
Velocity Vector Flowfield.....	5-2
Contour Plot Analysis.....	5-3
$\phi = 0.40$	5-3
$\phi = 0.52$	5-4
$\phi = 0.62$	5-5
$\phi = 0.72$	5-6
Turning angles.....	5-7
Summary.....	5-9
VI. Conclusions and Recommendations.....	6-1
Conclusions.....	6-1
Recommendations.....	6-3
References.....	BIB-1
Figures.....	7-1

Appendix A. Hotwire Information.....	A-1
Origin of the Governing Equations.....	A-1
Calibration Procedure.....	A-3
Hotwire Transformation Equations.....	A-7
Appendix B. Pressure Rake Information.....	B-1
Pressure System Start-up.....	B-1
Passage Total Pressure Loss Calculations.....	B-3
Appendix C. Data Reduction Codes.....	C-1
Appendix D. Equipment Listing.....	D-1
Vita.....	8-1

List of Figures

Figure	Page
2-1. Linear Compressor Cascade with Moving Endwall Flowfield Description (McMullan, 1996:7-1).....	7-1
2-2. Cascade Nomenclature (adapted from Cohen et al., 1987).....	7-1
2-3. Crenulated Blade Geometry (McMullan, 1996:7-3).....	7-2
3-1 Air Supply System and Diffuser/Stilling Chamber (Costello, 1993:69).....	7-3
3-2 Cascade Test Section (Peter, 1995:7-6).....	7-4
3-3. Blade Profile NACA 64-A905 (Peter, 1995:7-8).....	7-5
3-4 Rotor and Test Section Integration (Peter, 1995:7-4).....	7-6
3-5 Total Pressure Rake Testing Region.....	7-7
3-6. Cascade Coordinate System (Peter, 1995:7-5).....	7-8
4-1. Hotwire Calibration Raw Voltage Data.....	7-9
4-2. Hotwire Geometry (Bruun, 1995:148)	7-9
4-3. Hotwire 1 Voltage Variation with Fluid Temperature Change.....	7-10
4-4. Hotwire 2 Voltage Variation with Fluid Temperature Change.....	7-10
4-5. Cross-Section of Rotor and Middle Blade Passage (McMullan, 1996:7-5)..	7-11
5-1. Velocity vectors - v-w components $\phi = 0.52$ (Crenulated Blade).....	7-12
5-2. Velocity vectors - v-w components $U_x = 164.3$ ft/s (Crenulated Blade-no rotor).....	7-13
5-3. Velocity vectors - v-w components $\phi = 0.52$ (Regular Blade).....	7-14
5-4. Velocity vectors - v-w components $U_x = 164.3$ ft/s (Regular Blade-no rotor).....	7-15

5-5.	Local total pressure loss contour plot $\phi = 0.40$ (Crenulated Blade).....	7-16
5-6.	Local total pressure loss contour plot $\phi = 0.40$ (Regular Blade).....	7-17
5-7.	Local velocity contour plot $\phi = 0.40$ (Crenulated Blade).....	7-18
5-8.	Local velocity contour plot $\phi = 0.40$ (Regular Blade).....	7-19
5-9.	Local total pressure loss contour plot $\phi = 0.52$ (Crenulated Blade).....	7-20
5-10.	Local total pressure loss contour plot $\phi = 0.52$ (Regular Blade).....	7-21
5-11.	Local velocity contour plot $\phi = 0.52$ (Crenulated Blade).....	7-22
5-12.	Local velocity contour plot $\phi = 0.52$ (Regular Blade).....	7-23
5-13.	Local total pressure loss contour plot $U_x = 164.3$ ft/s (Cren. Blade-no rotor).....	7-24
5-14.	Local total pressure loss contour plot $U_x = 164.3$ ft/s (Reg Blade-no rotor).	7-25
5-15.	Local velocity contour plot $U_x = 164.3$ ft/s (Cren. Blade-no rotor).....	7-26
5-16.	Local velocity contour plot $U_x = 164.3$ ft/s (Regular Blade-no rotor).....	7-27
5-17.	Local total pressure loss contour plot $\phi = 0.62$ (Crenulated Blade).....	7-28
5-18.	Local total pressure loss contour plot $\phi = 0.62$ (Regular Blade).....	7-29
5-19.	Local velocity contour plot $\phi = 0.62$ (Crenulated Blade).....	7-30
5-20.	Local velocity contour plot $\phi = 0.62$ (Regular Blade).....	7-31
5-21.	Local total pressure loss contour plot $\phi = 0.72$ (Crenulated Blade).....	7-32
5-22.	Local total pressure loss contour plot $\phi = 0.72$ (Regular Blade).....	7-33
5-23.	Local velocity contour plot $\phi = 0.72$ (Crenulated Blade).....	7-34
5-24.	Local velocity contour plot $\phi = 0.72$ (Regular Blade).....	7-35

5-25.	Local flow turning angle (degrees) $\phi = 0.52$ (Crenulated blade).....	7-36
5-26.	Local flow turning angle (degrees) $U_x = 164.3$ ft/s (Crenulated blade-no rotor).....	7-37
5-27.	Local flow turning angle (degrees) $\phi = 0.52$ (Regular blade).....	7-38
5-28.	Local flow turning angle (degrees) $U_x = 164.3$ ft/s (Reg. blade-no rotor)...	7-39
5-29.	Total pressure loss coefficient comparisons (Region and passage).....	7-40

List of Tables

Table	Page
3-1 Blade Surface Coordinates and Mean Camber Line.....	3-3
3-2 Cascade Specifications.....	3-4
4-1 Component Accuracies.....	4-7

List of Symbols

Symbol

AFIT	Air Force Institute of Technology
AR	Blade aspect ratio
ASME	American Society of Mechanical Engineers
DF	Diffusion Factor
NACA	National Advisory Council for Aeronautics
NEAT	New England Affiliated Technologies
PSI	Pressure Systems Inc.
A	Hot-wire calibration constant, or Area (m^2)
A_w	Hotwire area (m^2)
B	Hot-wire calibration constant
C_p	Specific heat of air at constant pressure (J/kg K)
C_x	Axial velocity of cascade airflow (m/s)
D	Hotwire diameter (m)
I	Current (Amps)
Nu	Nusselt number
P_{rake}	Rake-measured local total pressure (Pa or psi)
P_{static}	Static pressure (Pa or psi)
P_{t1}	Inlet total pressure (Pa or psi)
R	Universal gas constant (J/kg K)
R_1	Wheatstone bridge resistance (Ohms)

R_L	Probe and cable resistance (Ohms)
R_w	Hotwire resistance (Ohms)
Re	Reynolds number
S_1	Sutherland constant
T_0	Reference temperature (K or R)
T_a	Temperature of ambient fluid (K or R)
T_f	Film temperature (K or R)
T_{static}	Static temperature (K or R)
T_{total}	Total temperature (K or R)
T_w	Hotwire temperature (K or R)
U	Rotor edge velocity (m/s or ft/s)
V	fluid flow velocity (m/s or ft/s), or Voltage (Volts)
V_1	air inlet velocity (m/s or ft/s)
V_2	air outlet velocity (m/s or ft/s)
V_{e1}	Effective velocity of hotwire 1 (m/s or ft/s)
V_{e2}	Effective velocity of hotwire 2 (m/s or ft/s)
V_{eff}	Effective velocity (m/s or ft/s)
V_{local}	Local velocity (m/s or ft/s)
V_w	Hotwire voltage (Volts)
a	point of maximum camber
b	temperature loading factor
c	blade chord (in or cm)

f	yaw parameter
g	yaw parameter
h	blade span (in or cm), or convection heat coefficient (Watts/m ² K)
i	incidence angle (degrees)
k	cooling ratio, or heat conduction coefficient (Watts/m K)
k ₀	reference heat conduction coefficient (Watts/m K)
\dot{m}_{center}	mass flow rate in the center region (kg/s)
\dot{m}_{local}	local mass flow rate (kg/s)
\dot{m}_{root}	mass flow rate in the root region (kg/s)
\dot{m}_{tip}	mass flow rate in the tip region (kg/s)
n	Hot-wire calibration constant
q	heat transfer (Watts)
rpm	revolutions per minute
p/s	pressure surface
s	blade pitch
s/s	suction surface
t	blade tip clearance (in or cm)
u	axial velocity component (m/s or ft/s)
v	pitchwise velocity component (m/s or ft/s)
w	spanwise velocity component (m/s or ft/s)
x	axial coordinate (in)

y	pitchwise coordinate (in)
z	spanwise coordinate (in)
ΔA	incremental area (m^2)
ΔP_{local}	difference between local total pressure and inlet total pressure (Pa or psi)
Δy	incremental pitchwise distance (in)
Δz	incremental spanwise distance (in)
α	angle between hot-wire normal axis and fluid velocity (degrees)
α_1	air inlet angle (degrees)
α_1'	blade inlet angle (degrees)
α_2	air outlet angle (degrees)
α_2'	blade outlet angle (degrees)
$\overline{\alpha}_1$	Hotwire 1 angle relative to probe axis (degrees)
$\overline{\alpha}_2$	Hotwire 2 angle relative to probe axis (degrees)
ε	deflection angle (degrees)
ϕ	flow coefficient, (C_x/U)
ζ	stagger angle (degrees)
δ	deviation angle (degrees), incremental change in ϖ
γ	ratio of specific heats
μ	viscosity ($N \cdot s/m^2$)
μ_0	reference viscosity ($N \cdot s/m^2$)

ρ	density (kg/m^3)
θ	blade camber angle, flow angle to hotwire probe axis (degrees)
$\overline{\omega}$	mass averaged total pressure loss coefficient
$\overline{\omega}_{\text{center}}$	mass averaged total pressure loss coefficient for the center region
$\overline{\omega}_{\text{local}}$	mass averaged local total pressure loss coefficient
$\overline{\omega}_{\text{passage}}$	mass averaged total pressure loss coefficient for the passage
$\overline{\omega}_{\text{region}}$	mass averaged total pressure loss coefficient for a region
$\overline{\omega}_{\text{root}}$	mass averaged total pressure loss coefficient for the root region
$\overline{\omega}_{\text{tip}}$	mass averaged total pressure loss coefficient for the tip region

Abstract

The effects of changing Reynolds number and flow coefficients on the velocity and pressure flowfields within a linear cascade with moving endwall were investigated in this experimental thesis. All flowfield measurements were taken at a constant compressor blade tip gap clearance of 1.0 % chord and endwall speed of 318.6 ft/s (97.1 m/s), with flow coefficients of 0.40, 0.52, 0.62 and 0.72. All data acquisition occurred in a plane 23 % chord downstream of the trailing edge plane of the linear cascade. Hotwire probes determined the complete passage, three-dimensional flowfield behind both crenulated and regular blade geometries. Examination of vector plots revealed that the mid-span crenulations aligned the flow axially, increasing the wake mixing and reducing the spanwise flow evident in the regular blade's wake region. A total pressure rake measured the pressure flowfield behind the blades, showing that the crenulated blade geometry produced larger, less intense areas of total pressure loss than for the regular blades. Overall, the crenulated blade tested showed equal passage total pressure losses, increased wake mixing, reduced wake deficit and a reduced flow turning angle compared to a regular blade of similar overall dimensions.

TIP VORTEX AND CRENULATION EFFECTS IN A COMPRESSOR CASCADE WITH MOVING ENDWALL

I. Introduction

Background

Improving the performance of the axial compressor contained in aircraft turbine engines is an important research topic. Increased knowledge of two major sources of losses in the compressor, the rotor blade wake and the blade tip region, aids in the analysis and design of future engine components. Wake flowfield characteristics and total pressure losses are strong indicators of compressor blade efficiency. In order to study these effects, linear cascade wind tunnels and rotating compressor rigs are used to test blade configurations and designs. These research tools produce flowfields helpful in the determination of velocity and pressure distributions found in the blade region.

Summary of Previous Research

Several methods have been devised to study the compressor blade wake and blade tip regions. Herzig et al., (1954) used a moving belt to simulate wall movement relative to the blades. His experiment identified a vortex created by the wall boundary layer being scraped off the suction side of the blade tip. Peter (1995) showed an excellent progression

of this phenomenon by steadily increasing the rotational velocity of a rotor used to model endwall motion.

Using stationary compressor cascades, Kang and Hirsh (1993a, 1993b), Storer (1989) and Kunz et al., (1993) have performed research in the blade region, determining the effect tip clearance has on the velocity and pressure fields in the blade passage. Veasart (1989), DeCook (1991), Costello (1993), and Spacy (1993) used stationary cascades to analyze the effect of blade crenulations on several parameters, including total pressure losses, velocity contours and flow turning angles, using various blade configurations and flow conditions. Blade crenulations are notches of variable geometry cut into the trailing edge of the compressor blade. These two-dimensional results did not take into consideration the rotor blade movement relative to the engine wall as found in an axial compressor.

Dr. B. Lakshminarayana (1980), designed a rotating compressor rig with both tangential and radial data acquisition capabilities using either hot wire or pressure probes. Subsequent research such as Pouagare et al., (1982), Pandya and Lakshminarayana (1983), Sitram and Lakshminarayana (1983), Pouagare et al., (1985), Lakshminarayana et al., (1986) produced excellent three-dimensional results for many flow conditions providing information on the velocity flowfields and pressure distributions inside a compressor.

Using a linear cascade with moving endwall to model the relative motion of the rotor blade with respect to the engine annulus wall, Peter (1995) and McMullan (1996) investigated the effects of blade tip gap on total pressure losses for straight trailing edge

and crenulated blades. Peter (1995) also varied the rotor speed to investigate changes associated with endwall speed but chose an axial velocity that produced large flow coefficients, ϕ (axial flow velocity divided by the outer surface velocity of the moving endwall, or C_x/U), which better modeled start-up values of the engine but not steady engine operating conditions. McMullan (1996) used a single flow coefficient consistent with normal engine operation but in order to achieve this flow coefficient, the axial velocity chosen forced the flow Reynolds number under 1×10^5 , considered to be below what is encountered in actual engine operation. McMullan (1996) also mapped the three-dimensional vortex development caused by the moving endwall, showing the movement of the boundary layer vortex, scraped from the suction side by the moving endwall.

Objective

The objective of this research was to map the flow features contained in the linear cascade with moving endwall at conditions more closely resembling actual engine operating Reynolds numbers and flow coefficients to compare crenulated and conventional blade designs. Using a tip gap of 1.0% and a constant rotor speed, the axial velocity was varied to produce flow coefficients ranging from 0.4 to 0.72, and Reynolds numbers from between 9.72×10^4 to 1.78×10^5 . Limitations in the equipment of the cascade precluded higher values. A complete mapping of the flowfield in the exit plane of the blades was investigated using both hotwire and total pressure rake in order to determine if variations present would indicate performance differences.

A description of the general flowfield found within the cascade and governing equations for the investigated pressure loss coefficients is found in Chapter II. The

experimental apparatus used in this research, including the component and software modifications is described in Chapter III. Chapter IV contains the general procedures for equipment calibration, data acquisition and data reduction with references to appendices for specific checklists. Discussion of the results is found in Chapter V, while Chapter VI makes conclusions and recommendations for further research.

II. Flow Description

Flowfield in a Linear Cascade with Moving Endwall

The three-dimensional flowfield found in axial compressors is difficult to accurately model analytically. Although normally limited to two-dimensional analysis, Peter's (1995) research indicated that the linear cascade enhanced with the moving endwall can effectively model relative blade motion in the tip region. This region is where McMullan (1996) found an advantage to crenulated designs. The linear cascade is also an excellent tool to compare similar blades in a variety of flow conditions. The wake region of crenulated blades is a specific region of interest, where multiple vortices replace the vortex sheet normally shed by a blade with a straight trailing edge. Figure 2-1 shows the general flow characteristics contained in the linear cascade with the moving endwall included. An excellent discussion on the specifics of these flowfields is contained in McMullan (1996).

Compressor Cascade

The linear cascade used in this research is a row of eight identical compressor blades, equally spaced along the blade row, with the trailing edges of each blade parallel to one another, forming a plane parallel with the plane of rotation of the moving endwall. The description of a linear cascade is specified by the blade geometry and the flow conditions through the blades. Figure 2-2, from Cohen (1987), illustrates the nomenclature that is associated with a linear cascade. Blade geometry is defined by the blade chord (c), the pitch (s), the blade thickness distribution, stagger angle, blade inlet and exit angles (α_1' and α_2'), blade span (h), camber angle (θ), and aspect ratio (AR). The camber angle is the

difference between the inlet and exit blade angles. The aspect ratio is the span divided by the chord. Flow conditions in the cascade are defined by the air inlet velocity (V_1), and angle (α_1), outlet velocity (V_2) and angle (α_2), deflection angle (ϵ), incidence angle (i), and the deviation angle (δ). The flow's deflection angle is the difference between the inlet angle and outlet angle, the incidence angle is the difference between the air inlet angle and the blade inlet angle, and the deviation angle is the difference between the air outlet angle and the blade outlet angle.

Blade Crenulation Performance

Crenulation is a general reference to notches placed in the trailing edge of a blade. Figure 2-3 shows the specific crenulation geometry used in this research. Wennerstrom (1982) first suggested that blade crenulations had wake mixing advantages over straight trailing-edged designs. Subsequent researchers have shown increased wake mixing for crenulated geometries at various flow conditions and found that specific crenulation geometries worked better than others. Veasart (1989) found that two blade crenulation geometries (one with small crenulations the other with larger ones) improved wake mixing, reduced total pressure losses and increased turning angle. Using the same blades DeCook (1991) also found improved mixing and less total pressure loss but at a slight reduction in turning angle. DeCook used combinations of wall suction and turbulence levels to show the advantage of crenulations under those conditions. Looking at his reference plot with both suction and turbulence off, it is evident that the advantages of the crenulations concerning total pressure losses are not realized until distances on the order of chord length are realized. At the closest measurement plane to the trailing edge of the

cascade, the advantages are minimized. Spacy (1993) specified that the smaller crenulations were superior to the larger crenulation geometry blade. Costello (1993), using only the larger geometry blade, repeated DeCook's findings of improved mixing with a reduction in turning angle but found that only at large incidence angles did the crenulated blade show decreased total pressure losses.

Using a slightly redesigned blade with small, narrow crenulations similar to the small crenulation geometry of past research, Peter (1995) incorporated a moving endwall aspect to the study of crenulated blades, but did not directly compare conventional blades with his crenulated design at an identical flow condition. Investigating a variety of tip gaps, Peter inserted his crenulated design at one of the tip gap clearances, with all other data points using regular blades at other tip gap clearances. Graphs of the total pressure loss coefficients for each condition tested indicated that the value of the crenulated design loss coefficient were approximately equal to the regular blade loss coefficients. McMullan (1996) used Peter's blades and with the moving endwall found that the crenulated geometry decreased passage total pressure losses, primarily in the tip region of the cascade.

Methods of Studying Crenulation Effects

Two methods were used to show differences in the flowfields between straight trailing edged blades and creulated blades. Hotwire anemometry was used to show the wake vortices created by the blade crenulations in order to identify what impact they had on the overall flowfield. This data also allowed for the calculation of the local flow turning angles, from which the passage mass-averaged flow turning angles were computed.

Previous computations of the cascade turning angles only included a central portion of the passage, with the dimensions specified by the width of a single crenulation of the blade geometry in question. Since most compressor work calculations concern an averaged flow turning angle over the entire passage from hub to tip, this research used the entire passage between blades 4 and 5 in order to compute the turning angle. Pressure rake data was taken in the same plane as the hotwire velocity information, to determine passage total pressure loss coefficients. Local pressure loss coefficients, velocity variances and the local flow turning angles in this plane were presented as contour plots as additional comparisons.

Total Pressure Loss Coefficients

A means for comparing passage losses is the mass averaged total pressure loss coefficient, $\bar{\omega}$. This quantity is calculated for individual data points in the cascade passage and then mass averaged for an entire passage between two blades. For each data point:

$$\bar{\omega}_{local} = \frac{\Delta P_{local}}{\frac{1}{2} \rho_1 V_1^2} \quad (1)$$

Both terms in the denominator are computed starting with the total and static pressures obtained in the throat section along with the total temperature indicated by a probe in the stilling chamber. From the pressure ratio and total temperature, the static temperature can be computed (much like the exit plane computation seen in Equation 3). From this the inlet density and velocity are computed. The numerator is found by subtracting the local value of total pressure (obtained by total pressure rake), P_{rake} from the total pressure value

of the cascade inlet. The inlet total pressure (P_{t1}) was measured with a Pitot probe inserted into the air flow from the bottom of the tunnel throat.

$$\Delta P_{local} = P_{t1} - P_{rake} \quad (2)$$

In order to compute the passage value of \dot{m} , the local mass flow must also be computed. This requires several steps. First, the local static pressure, P_{static} is needed, taken from the average of nine static ports located at the same x location as the total pressure rake. The local static temperature is found from the isentropic relationship shown below. This assumes that the flow is adiabatic, so that the total temperature, T_{total} everywhere is the same as that measured in the stilling chamber.

$$T_{static} = T_{total} \left(\frac{P_{static}}{P_{rake}} \right)^{\frac{\gamma-1}{\gamma}} \quad (3)$$

γ is the ratio of specific heats, valued at 1.4 for air in these calculations.

$$\dot{m}_{local} = \rho V_{local} \Delta A \quad (4)$$

The local density is computed by rearranging the perfect gas law.

$$\rho = \frac{P_{static}}{RT_{static}} \quad (5)$$

with R being the gas constant for air, 287 J/kg-°K.

The velocity at each point is found using the total enthalpy definition for a calorically perfect gas.

$$C_p T_{total} = C_p T_{static} + \frac{V_{local}^2}{2} \quad (6)$$

Using the relationship that $C_p = \gamma R/(\gamma-1)$, solve Equation 6 for V_{local} . Veasart (1989)

determined the verity of these calculations for data methodology.

The local mass flow can be computed with ΔA representing the local area about the data point, equal to the spanwise data spacing times the pitchwise step size. In terms of the cascade test section coordinate system, $\Delta A = \Delta y \Delta z$.

The passage total loss coefficient, $\omega_{passage}$ is defined as the following:

$$\omega_{passage} = \frac{\sum_{y,z} (\omega_{local} \dot{m}_{local})}{\sum_{y,z} \dot{m}_{local}} \quad (7)$$

with the summation defined as the number of steps in y and the number of steps in z.

Turning Angle

The turning angle was mass-averaged by the following general equation.

$$A_{passage} = \frac{\sum_{y,z} (\rho_{local} V_{local} A_{local})}{\sum_{y,z} \rho_{local} V_{local}} \quad (8)$$

For this computation only, the variable ρ_{local} was considered constant, and was removed so that the local values of velocity determined by the hotwire are needed with the quantity A being replaced by the local values of the flow turning angle. The result is the passage mass-averaged flow turning angle.

III. Experimental Apparatus

The research for this thesis was completed in Building 640, Room 143 at the Air Force Institute of Technology using the AFIT Cascade Wind Tunnel Facility. This facility consists of five major components, the air supply system, the settling chamber, the cascade test section, the moving endwall rotor and data acquisition system.

Air Supply System

The cascade wind tunnel has two supply systems, outside air drawn in through a 30kW centrifugal blower and a 100+ psig permanent centralized supply system which is available via pipeline throughout Building 640. These sources may be used separately or in conjunction with one another. The mass flow demands of these experiments did not require use of the 30kW blower. The air mass flow from the building supply system was controlled by a flow rate control valve on the supply line, with an upper limit of approximately 230 ft/s (70 m/s). Normally the building supply is sustained by a single compressor. When the indicated pressure drops below a preset number (approximately 90 psig), a second, identical compressor automatically turns on in order to maintain the system above 90 psig. Moderate to high mass flow requirements cause an oscillation in the system, draining the supply until the second compressor comes on line which increases the pressure about the cut-in limit. After a preset period of time, the second compressor shuts off, whereupon the system once again starts to drop in pressure. This fluctuation causes a velocity fluctuation in the test section which can be avoided by using a dump valve in the back of Room 143, which exhausts air to the outside of the building. This

artificial demand on the system can be used to keep the system pressure below 90 psig, keeping both compressors operating at a stable rate. The lowest pressure the system can be operated on is 70 psig. Below this value the compressor's lubrication oil can be sucked out of the unit and into the pipeline.

Settling Chamber

The input air enters a 10 ft (3 m) diffuser which feeds into a large settling chamber which slows the air to approximately 10 ft/s (3 m/s). The settling chamber contains screens, filters and honeycomb meshes to straighten the flow, and a central styrofoam plug designed to prevent noise from the supply system from entering the test section. The flow continues through a ASME long radius bellmouth nozzle into the test section. Allison (1982) contains a more detailed description. Figure 3-1 illustrates the overall system.

Test Section and Moving Wall Section

The test section is the compressor cascade structure containing the blade row, mated with the moving wall section, as shown in Figure 3-2. The cascade is made up of eight NACA 64-A905 compressor blades. The coordinates of a representative blade are contained in Table 3-1, with the x values referring to distance from the leading edge along the blade chord, and y to the perpendicular distance from the blade chord. A representative blade is shown in Figure 3.3. Table 3-2 describes the cascade specifications as associated with the flowfield. The physical dimensions of the interior of the test section are 9 in (22.86 cm) high, 2 in (5.08 cm) wide, and 12 in (30.48 cm) deep. A throat section connects the test section to the stilling chamber. This throat section can be changed, with

Table 3-1. Blade Surface Coordinates and Mean Camber Line

Suction Surface x (cm)	Suction Surface y (cm)	Pressure Surface x (cm)	Pressure Surface y (cm)	Mean Camber y (cm)
3.751	0.000	3.751	0.000	0.000
3.677	0.015	3.675	0.007	0.011
3.527	0.046	3.524	0.021	0.033
3.303	0.089	3.373	0.035	0.062
3.193	0.111	3.184	0.052	0.081
3.008	0.152	2.994	0.069	0.110
2.709	0.214	2.693	0.099	0.156
2.410	0.269	2.392	0.127	0.198
2.108	0.315	2.093	0.149	0.232
1.803	0.342	1.798	0.160	0.251
1.498	0.345	1.503	0.158	0.251
1.308	0.336	1.318	0.151	0.244
1.118	0.320	1.133	0.142	0.231
0.929	0.297	0.947	0.129	0.213
0.740	0.267	0.761	0.113	0.190
0.551	0.228	0.575	0.092	0.160
0.362	0.179	0.388	0.065	0.122
0.287	0.157	0.313	0.053	0.105
0.212	0.131	0.238	0.040	0.086
0.138	0.101	0.162	0.026	0.063
0.065	0.063	0.086	0.010	0.037
0.029	0.040	0.047	0.002	0.021
0.012	0.025	0.026	-0.002	0.011
0.000	0.008	0.008	-0.003	0.003
0.000	0.000	0.000	0.000	0.000

various available throat sections determining the flow angle of the inlet air flow. The throat angle for this research was 31 degrees. Adjustable tailboards run along the top and bottom of the test section to allow for the balancing of the exit static pressure with ambient pressure.

Table 3-2. Cascade Specifications

Specification	Symbol	Value
Blade Span	h	1.988 in (5.05 cm)
Blade Chord	c	1.50 in (3.81 cm)
Blade Spacing	s	1.0 in (2.54 cm)
Blade Camber Angle	θ	30.51 deg
Blade Inlet Angle	α_1'	26.51 deg
Blade Outlet Angle	α_2'	4.00 deg
Diffusion Factor	DF	0.332
Point of Maximum Camber	a	0.5 chord
Stagger Angle	ξ	7.50 deg
Air Inlet Angle	α_1	31.0 deg
Average Air Outlet Angle	α_2	3.05 deg
Average Deviation Angle	δ	7.05 deg
Incidence Angle	i	4.49 deg
Average Deflection Angle	ϵ	27.95 deg
Inlet Velocity	V_1	Variable
Outlet Velocity	V_2	Variable

One side of the test section is easily removed to allow for either the positioning of a stationary endwall along the entire axial length of the test section or the moving endwall assembly, which consists of the endwall rotor and two aluminum half walls. The stationary endwall provides a tip gap of 0.012 in (0.0305 cm) while the moving endwall is constructed to allow a variety of tip gap clearances, although the tip gap for this research was maintained at 1.0 % of the blade chord.

The endwall rotor was designed so that 0.25 in (0.635 cm) of the rotor edge extends beyond the blade in both the upstream and downstream directions. Once the rotor is positioned properly, the half walls should be positioned with a 0.025 in (0.0635 cm) gap to minimize flow leakage. Tape fills the 0.05 in (0.127 cm) gap between the rotor and the

wall upstream while a Teflon scraper fills the 0.10 in (0.254 cm) gap between the rotor and the adjacent wall downstream, to minimize flow leakage in these areas. These wall clearances were designed to provide spacing for the rotor during its maximum vibration. Figure 3-4 shows the rotor mated with the test section. Updated equipment used to measure the motor rpm to rotor speed ratio found the ratio to be 1.24 which was later confirmed using a Cole-Palmer 08210 Series Phototachometer accurate within 1.0 rpms at speeds up to 20,000 rpms. For further information on the cascade section and moving endwall system refer to Peter (1995).

Data Acquisition System

The data acquisition system for this research was modified from previous efforts. The pressure, velocity, temperature, and probe traverse subsystems were all linked to a new central computer, which provided for either manual or automatic data acquisition. All desired information was available in near real time in a graphical interface controlled by the user. Details of the methodology and acquisition processes for each subsystem are explained more fully in Chapter IV.

Central Computer. The central computer was a Zenith Z-Station 510, with a 486-50 central processor, utilizing Labview software connected to a National Instruments MIO-16 Data Acquisition Board, which controlled all aspects of the data acquisition.

Pressure Measurement Subsystem. The pressure measurement subsystem was a Pressure Systems Inc. Model 8400 Pressure Scanner, three 32 port transducer blocks, a five-tube total pressure rake and barometer, and vacuum pump. The transducer blocks measure differential pressures from ambient conditions, and have plunger operated valves

which shift the blocks between acquisition and calibration modes. The Model 8400 contains an internal certified standard transducer used for calibration. The calibration mode may be used at any time in between data runs to ensure the accuracy of the system. The pressure scanner, operating at a 20 kHz scan rate, sampled each of the 96 ports 11 times and took the arithmetic mean of those 11 values. For this research, the total pressure of the stilling chamber, the nine static ports in the inlet throat, the first row of nine static ports in the blade wake (at 0.35 in (0.89 cm) behind the trailing edges of the blades), and the five rake total pressures were sampled. The total pressure rake measured the total pressure variations in the wake of the cascade with less than a 3.5 % area blockage. The reference ambient pressure was measured using an Endevco Model 4428A Pressure Indicator. Figure 3-5 shows the rake dimensions and testing window information.

Velocity and Temperature Measurement Subsystem. The velocity measurement subsystem consisted of a TSI Model IFA 100 Intelligent Flow Analyzer and a TSI Model 1241-T1.5 hotwire probe. Two Model 150 Constant Temperature Anemometer Modules were used to measure the voltages of the probes. The signals acquired by the IFA 100 were conditioned by two Model 157 Signal Conditioners. Data samples for the hotwire calibrator and tunnel hotwire experiments were computed using the average of 200 samples taken at 5 kHz. The voltages for all the temperatures read from thermocouples were processed and displayed on Omega DP25-TC Programmable Digital Thermocouple Meters. The temperature sensors were Omega T-type copper-constantan thermocouples. This temperature subsystem measured the ambient temperature of the laboratory and the total temperature of the stilling chamber.

Probe Traverse Control. The probe traverse was used to accurately position the hotwire and total pressure rake within the desired flowfield. The axes for the control system are shown in Figure 3-6. The positioning in the x-axis was performed manually with a handcrank. The location in the x direction was held constant for this research, in the plane of the first row of static ports downstream of the blade region. For movement in the y and z directions two Oriental Motor Company Stepper Motors were controlled by the Labview program running nuLogic, Inc., pcStep 4A Stepper Controller software. Chapter IV explains the data acquisition and reduction procedures in detail.

IV. Experimental Procedure

Systems Calibration

Hot Wire Calibration. Hot wire anemometry was used to determine the three velocity components of the flowfield in the linear cascade. An x-configured hot wire was used, with measurements taken in the yz-plane 0.35 in (0.89 cm) behind the trailing edge of both the crenulated and straight edged blades. The constant temperature method was used, so that the voltage required to keep the temperature of the hot wire constant was proportional to the heat transfer produced by the local flowfield over the wire. From Bruun (1995), the general power law equation used to determine the voltage-velocity relationship can be described as

$$Nu \left(\frac{T_f}{T_a} \right)^b = A + B Re^n \quad (9)$$

where Nu is the hotwire Nusselt number. A detailed description of the development of this equation is contained in Appendix A. The temperature ratio is known as the temperature loading factor, with the exponent b determined during the calibration procedure. Re is the Reynolds number also relative to the hotwire, raised to a power determined during the calibration process.

$$Re = \frac{\rho V_{eff} D}{\mu} \quad (10)$$

The characteristic length, D is the diameter of the hot wire sensor. The effective velocity, V_{eff} is a function of the flow velocity and angle relative to the hot wire.

$$V_{eff} = V \sqrt{\cos^2 \alpha + k^2 \sin^2 \alpha} \quad (11)$$

Hotwire Calibration Procedure. The procedure for the x-configured hotwire calibration is completed in two steps. The first step varies both flow angle and velocity at a constant fluid ambient temperature to determine the cooling ratio k and the values of A , B , and n . With the cooling ratio determined, the temperature of the calibrator flow is varied to calculate the loading factor, b .

Flow speed was varied from 30-70 m/s in 10 m/s increments, while the angle was varied from -40 to 40 degrees in 20 degree increments resulting in the raw voltage data for the two wires shown in Figure 4-1. With the known hotwire geometry (Figure 4-2), a least squares routine calculated the values of A , B , n , and k for each wire from equation with b set to zero since the value of k is independent of temperature. With the probe axis aligned with the flow, the temperature of the flow was increased and a data sample taken with the flow speed varying from 30-70 m/s. Figures 4-3 and 4-4 show the raw data of each wire as the temperature of the flow was increased over the expected conditions of the tunnel cascade. With this data, the least squares routine determined the value of the loading factor, b .

Calibration Verification. With the calibration coefficients determined, the accuracy of the resulting equation was checked by exposing the probe to a range of velocities and angles in the calibrator and measuring the resultant voltages. Within the calibrated region, velocities were accurate within ± 0.5 m/s and ± 0.6 degrees. Velocities measured above and below the calibrated region showed only slightly increased uncertainty. A detailed calibration procedure is contained in Appendix A, following the development of the governing equations.

Pressure System Calibration. The PSI 8400 pressure scanner was initialized and calibrated at the start of each day prior to all data acquisition. The process was completely automated except for making sure the vacuum pump was operating before the program was started. The calibration consisted of five point calibrations from -1.0 psid to +1.0 psid for two of the transducer blocks and -5.0 psid to +5.0 psid for the third transducer block. At any time, the system may be re-zeroed to account for temperature changes in the laboratory over time. Additional information is found in the PSI 8400 Pressure Scanner User's Manual (1993).

Data Acquisition.

System Preparation. The cascade wind tunnel was turned on at the beginning of each day prior to data acquisition to cleanse the system of water accumulation which could contaminate the pressure rake or damage the hotwire probe should water droplets transit the test section. The vent valve and/or drain valve at the rear of Rm 143 accomplished this task prior to direction of the air flow through the stilling chamber and cascade area. During software preparation, the tunnel and rotor were operated to allow the operating temperatures of each component to stabilize. Once this was accomplished the entire system was shut down in order to set the rotor tip gap and in the case of the hotwire allow for installation of the hotwire probe. The system was immediately restarted following any required actions in order to minimize the temperature drop. The entire system preparation period was approximately 1.5 hours.

Tailboard Balancing. The upper and lower tailboards (see Figure 3.2) were balanced using screw adjusters for optimum expansion of the flow. This was accomplished by

adjusting cascade exit pressure to ambient conditions and ensuring a uniform pressure distribution across the blade trailing edge area. Four water manometers were used to set one tailboard equal to ambient pressure and then matched opposing pairs of the static ports were compared using opposing manometer ports. During this research the tailboards were balanced to within 0.3 inches of water or 0.011 psig (75.84 Pa).

Pressure Collection. Data acquisition of all total and static pressures were made by the PSI 8400 pressure scanner. Since the raw data was psid, ambient pressure was added to the raw data to compute the absolute pressure values. The inlet total pressure was measured at the inlet throat from a Pitot tube inserted into the incident air flow from the bottom of the tunnel. Nine inlet and nine exit plane static ports were averaged to obtain the inlet and exit plane static pressure values.

Temperature Collection. All required temperatures were measured in voltages from the thermocouples by the Labview software, translated to temperatures and displayed on the Omega Digital Thermocouple Meters.

Probe Controller. The NEAT 310 of previous research was replaced by a PCStep 4A stepper controller which has a direct interface with the Labview controlling software. The position accuracy of this system is 0.0005 in (0.0013 cm).

Hotwire Data Collection. The testing window for this research was the same as McMullan (1996). Figure 4-5 shows the dimensions and relation to the blades of the cascade. Instead of centering the yz plane in the center of the passage between blades 4 and 5, however, for purposes of data reduction, the (0.0,0.0) location in the yz plane was placed at 0.5 in above blade 4 and as close to the root wall as the probe would allow.

During data acquisition, the probe stepper moved in the y direction from 0.0 to -2.0 inches and 0.0 to 1.80 inches in the z-direction. This was equivalent to -1.0 to 1.0 in y and -0.9 to 0.9 in z for McMullan's research. The general cascade coordinate system is seen in Figure 3-6. All data was taken in the yz plane, 0.345 in (.89 cm) behind the trailing edge of the compressor blades. With the x-configuration wire, the two-dimensional u-w velocities were measured, with the x-wires aligned in the xz plane, the probe was rotated 90 degrees counter-clockwise and another measurement taken, of the u-v velocities. For repeatability of the data, if the u-component at each location agreed within the uncertainty of the hotwire (0.5 m/s), that data point was considered valid. The v-w components of the flowfield were the velocity components of interest for this research. The grid spacing throughout the testing window was 0.04 in (0.10 cm) in both spanwise (Δz) and pitchwise (Δy) directions. Hotwire data collection instructions are contained in Appendix A.

Total Pressure Rake Data Collection. In order to assimilate previous research, the (0.0,0.0) location of the pressure rake was located in the center of the passage spanwise (z) at the y-location midway between blades 3 and 4. The rake probes were aligned parallel to the trailing edge of the blade trailing edges, with the front edge of the rake probes in the xz plane corresponding to the first row of static ports 0.35 in (0.89 cm) behind the blade trailing edges. Three rake passes were made at z-locations -0.605, 0.0, and 0.605 inches from y = 0.0 to -2.0 inches at 0.04 inch increments. Figure 3-5 shows the approximate rake placement and the overlap of the edge probes between the data runs. Appendix B contains instructions on the setup and collection of the pressure quantities.

Data Reduction

Hotwire Data Reduction. The raw voltages and measured temperatures from each data run were converted to the effective velocities across each wire which were transposed to the pertinent planar velocity components. Taking the v and w components computed at each data point, and the (y,z) location, the entire array was plotted as a field of vectors using Matlab. Additionally, with the u-v components of the flow known, the relative turning angle behind the blades was plotted as a contour mapping. This turn angle information was also used to compute the mass-averaged flow turning angle as described in Chapter II.

Total Pressure Rake Data Reduction. Data measured during the pressure rake data acquisition included, T_{total} , P_{t1} , P_{static} , and P_{rake} (5 values). Following the equations developed in Chapter II, Microsoft Excel was used to calculate the local pressure loss coefficient, and local mass flow. The regional mass averaged pressure loss coefficient was computed according to

$$\omega_{region} = \frac{\sum \left(\omega_{local} \cdot \dot{m}_{local} \right)_{region}}{\dot{m}_{tip} + \dot{m}_{center} + \dot{m}_{root}} \quad (12)$$

The center region was defined as the center three probe readings, while both the tip and root included the full five rake probe readings. Passage loss coefficients are merely the addition of the three regional values. Regional and passage loss values were calculated within the Excel spreadsheet, with computed data exported to MATLAB in order to construct contour plots of the local pressure loss coefficients and local velocity values.

Error Analysis

Equipment and Instrumentation Accuracies. Table 4-1 contains the equipment accuracies for the pressure transducers, digital barometer, and thermocouples taken from the operating manual of each component. The hotwire's accuracy was determined during the calibration verification.

Table 4-1 Component Accuracies

Component	Accuracy
Pressure Transducers	0.0005 psid
Digital Barometer	0.005 psia
Thermocouples	0.3°C
Hotwire velocity	0.5 m/s
Hotwire Angle	0.6 degrees

Estimated Error for the Pressure Loss Coefficient. The error of ϖ from the accuracies of the equipment and instrumentation is found from

$$Error = \frac{\varpi + \delta}{\varpi} - 1 \quad (13)$$

where δ is the effect of changing the measured values individually to account for their accuracy. For largest expected error analysis each error component is assumed to be in the same direction. From the appropriate values in Table 4-1, the estimated error due to equipment and instrumentation was estimated at 1.3%. Including the uncertainties associated with the thermal and centrifugal expansion of the rotor calculated by Peter (1995), of 2% and 1%, the total estimated error of the ϖ calculation was found as 4.3%.

V. Results and Discussion

Introduction

All data gathered for this research was accomplished in the yz-plane 0.35 in (0.89 cm) or 23.0 % chord behind the trailing edges of the compressor blades. The tip gap clearance was maintained at 1.0 % of the blade chord and the rotor was kept at a constant 2200 rpm, which translated into a rotor edge speed, U of 318.6 ft/s (97.1 m/s). This was the denominator for the computation of the flow coefficient, ϕ . The numerator for the flow coefficient, C_x (axial velocities) for this research were 125.6 ft/s (38.3 m/s), 164.3 ft/s (50.1 m/s), 197.2 ft/s (60.1 m/s), and 230 ft/s (70.1 m/s). The resultant flow coefficients were 0.40, 0.52, 0.62, and 0.72. The lowest flow coefficient has the same axial velocity as McMullan (1996), to serve as a comparison between the two data sets. Although the rotor speed is 2200 rpm not 1700 rpm, Peter (1995) found that at a given flow condition, the impact on passage total pressure loss coefficients from changes in rotor speed of the magnitude stated here are minimal.

The local velocities and local total pressure loss coefficients are presented here as contour maps for all flow coefficients. At $\phi = 0.52$, vector plots of the v-w velocity components of the flow were taken with the hotwire to show the differences in the overall flowfields. Local total pressure loss coefficients, local velocities, and local turning angles of the flow with a $C_x = 164.3$ ft/s (50.1 m/s) with the rotor removed and replaced with a flat, stationary endwall with both blade ends flush with the walls (no gaps) were produced to show the contrast in flow conditions with and without the presence of the rotor.

Although the modifications to the tunnel to include the moving endwall create an asymmetrical flowfield (an approximate 0.125 inch step increase in area as the flow enters the passage when the rotor is removed), the information is included here to show the differences in the existing flowfield with the rotor and without its presence.

Velocity Vector Flowfield

The velocity vector plots of Figures 5-1 and 5-3 show the differences between the crenulated and regular blades at the flow coefficient of 0.52. At the root section of both blade geometries the secondary vortex is just visible at the edge of the data field. Looking at the regular blade in Figure 5-3, there is a spanwise flow toward the blade root along the pressure side of the blade. Adjacent to the vortex created by the blade root, there is a spanwise flow toward the tip along the suction side of the blade. In contrast, for the crenulated blade in Figure 5-1, the two counter-rotating vortices disrupts the spanwise flow seen on the regular blade, so that crossflow effects are limited to each half of the blade span. In the tip region of both blades, the tip leakage vortex shown by McMullan (1996:Figure 5-16 and 5-33) at 0.1 in behind the trailing edge of the blades has largely dissipated only 0.25 in later. The strong vortex above Blade 4 ($y=0.5$ in) is due to the rotor induced flow interacting with the boundary layers of the blade and stationary wall. Since the flowfield between blades 4 and 5 is considered to be more representative in its modeling of a compressor tip region, all subsequent discussion will center on this area.

Looking at Figures 5-2 and 5-4, the effects of the asymmetry in the tunnel are obvious, with the strong vortex created in the tip region of both blades dominating the passage. Although the flowfield is unique to the modified configuration of the tunnel, two items

deserve mention. First, the addition of the rotor movement eliminates the strong vortex in the tip region of both flowfields and minimizes the w-component prevalent in both stationary endwall cases. Second, the effects of the rotor motion only extend about halfway across the test area, with the root section of both blades relatively unchanged with or without rotor movement. This is seen in all cases of the flow coefficients tested.

Contour Plot Analysis

$\phi = 0.40$. As discussed by previous researchers of crenulated blades a definitive characteristic of the crenulations is the larger area of pressure losses in the center of the passage produced by the vortices of the crenulations in Figure 5-5. Although the area of losses across the center passage is less in Figure 5-6 for the regular blades, the intensity is increased. For the crenulated blade the 0.20 contour dominates the center passage, whereas for the regular blade a more typical value for that area is 0.275. The tip region shows that the moving endwall interaction produces a virtually identical loss contour field in that region between the blades. Near the root, the presence of the crenulation closest to the wall is evident by the notch in the contour lines in that area. This location is also where, for the regular blade, the highest intensity loss, 0.575, is found. This value is 0.150 above what the peak loss value is for the crenulated blade, but the gradient is very steep in that region for the regular blade and the values drop off rapidly in the area around the peak value. Both of these plots compare favorably to McMullan's(1996) Figures 5-40 for the regular blade and Figure 5-42 for the crenulated blade, especially in the root region. The slightly higher peak values in each case in the tip region are certainly from the higher rotor speed. The vortex above blade 4 in the tip regions of Figures 5-5 and 5-6 are seen in

McMullan's contour plots and are mentioned here for future reference. In the velocity contour plots, Figures 5-7 and 5-8, the rotor speed effectively masks any effects the crenulation has on the flow in the tip region. The bumps or spikes in the 110 ft/s contour line of the tip region between blades 4 & 5 of these two figures is a function of the graphics resolution and not a flow phenomenon. These spikes show up periodically throughout the contour figures. The next topic is flow velocity reduction. This is included to compare how the crenulated and regular blades effect the axial velocity of the flow in various areas of the passage. The values of interest are the lowest velocity contour values found in a particular region. The central region of the crenulated blade of Figure 5-7 shows 110 ft/s at mid-span, with contours reducing to 80 ft/s at the extreme left portion of the root region. The regular blade in Figure 5-8 at mid-span shows 100 ft/s with contours slowing to 70 ft/s in the root region.

$\phi = 0.52$. Figures 5-9 and 5-10 show the local ω loss contours for this flow coefficient.

The loss coefficient values in the central passage behind both types of blades have changed little when compared to the flow coefficient of 0.40, but the peak intensity in the tip region has increased to 0.80. The rotor produces a contour field approximately the same extent and magnitude for both blade geometries in the tip region. In the root region, the peak value is 0.65 for the regular blade, still 0.15 above the crenulated blade. The next subject of interest in Figures 5-9 and 5-10 is that the vortex above blade 4 has disappeared for both blade geometries when compared to the $\phi = 0.40$ cases (Figures 5-5 and 5-6). The flow coefficient of 0.52 is the same as in McMullan's (1996) figures mentioned previously but the Reynolds number has increased from 9.72×10^4 to 1.27×10^5 . The boundary layer

interaction above blade 4 now looks more like what is contained between blades 4 and 5. In Figures 5-11 and 5-12, the velocity contour plots no longer show the vortex activity indicated in Figures 5-7 and 5-8 ($\phi = 0.40$). This is in contrast to the hotwire information presented in Figures 5-1 and 5-3 that still shows the presence of a vortex in that region. Since the velocity contour plot is local axial velocity, this indicates that at this flow condition, the vortex is present but the boundary layer removes any evidence of the velocity "islands". The velocity contours in the tip and central regions of Figures 5-11 and 5-12 show minor differences but are generally equivalent in their shapes and values.

The velocity reduction comparison in the root region is notably different. The crenulated blades of Figure 5-11 shows a small island of 110 ft/s below blade 4, while for the regular blades of Figure 5-12, in the same root region below blade 4 the velocity is reduced to 80 ft/s. A notch in the velocity contours above the tip of blade 5 (approximate coordinates $-0.45y, -0.75z$ of Figure 5-11) suggesting the presence of the crenulation has appeared in the tip area of blade 5 but with little affect on the overall flow. For this flow coefficient of 0.52, the attached blade stationary endwall contours are also included. Comparing Figures 5-13 to 5-16 to Figures 5-9 to 5-12 respectively, shows the velocity and pressure contours of both blade geometries insensitivity of the blade root areas to the presence of the rotor.

$\phi = 0.62$. The peak loss coefficient contour values in the tip region show little change from the flow coefficient of $\phi = 0.52$, with the addition of a few isolated spots with an increased ω loss value of 0.875 (as compared to the $\omega=0.80$ peaks found at $\phi = 0.52$). Comparison of the tip region pressure loss contours in Figures 5-17 and 5-18 show they

are extremely similar while the central passage shows the slightly larger area of loss for the crenulated case with lines of less intensity than that for the regular blade. In the root region, the peak value for the regular blade is 0.65, 0.15 higher than the crenulated blade, but the areas of the peak values are smaller than for $\phi = 0.52$. Figures 5-19 and 5-20 show again that in the tip region, the velocity contours are of approximately the same extents and magnitudes. Along the central region of the crenulated blade in Figure 5-19 the lowest velocity contour is 170 ft/s. In Figure 5-20, the central passage of the regular blade shows a contour of 160 ft/s. Moving along the regular blade toward the root shows a velocity "island" of 100 ft/s. The velocity "island" in the same location on the crenulated blade of Figure 5-19 shows a value of 130 ft/s. The small velocity "island" with a value of 120 ft/s located directly below the velocity contour notch of the root region corresponds to approximately the same value at the same location on the regular blade so no comparative advantage is mentioned.

$\phi = 0.72$. An excellent example in Oates (1985) indicates that this flow coefficient is at the upper limit of what is considered normal engine operating flow coefficients, but was included in this research to support a trend that developed. This will be clarified in the discussion section. Looking at the total pressure loss contours in the tip regions of Figures 5-21 and 5-22, the peak ω values of 0.875 at the extremity of the contour plot shows little change over the flow coefficient of $\phi = 0.62$ nor any contour differences between the crenulated and regular blades. Except for a small area of blade 5 in the central passage where both the regular and crenulated blades display a loss coefficient of $\omega = 0.35$, both central blade portions seem relatively unaffected by the changing axial

velocity. The crenulated blade still holds a slightly lower loss coefficient of 0.20 when compared to the regular blade's central passage peak value of 0.275 but at the cost of a larger area of influence. In the root region of Figure 5-22 the peak value for the regular blade is 0.575, lower by 0.075 than the peak value for the same region in Figure 5-18 ($\phi = 0.62$). The crenulated blade's peak value in the root region of Figure 5-21 was 0.50 with a smaller region of coverage than Figure 5-17 ($\phi = 0.62$). Figures 5-23 and 5-24 show a very steep velocity gradient in the tip region with little difference between the regular and crenulated blades. There is still a notch in the velocity contours in the tip region above blade 5 (See coordinates in $\phi = 0.52$ discussion). This notch in the velocity contours is repeated across the flow coefficients starting at $\phi = 0.52$ but with the increased axial velocity, the rotor has a reduced effect on scraping the tip leakage vortex toward the pressure side of blade 5, so the regular blade also is showing less velocity reduction in that area. Although less pronounced than Peter's (1995) figures showing the progression of the scraping of the tip vortex as rotor speed was increased, the same effect can be seen by keeping the rotor speed constant and reducing the axial velocity (reducing the flow coefficient), as evident in Figures 5-24, 5-20, 5-12, and 5-8 for the regular blades and Figures 5-23, 5-19, 5-11, and 5-7 for the crenulated blades.

Turning Angles

Figures 5-25 to 5-28 are contour plots of the local flow u-v velocity component angle relative to the probe axis, which is aligned with the tunnel's axial flow axis, x. For these plots, when comparing them to Figures 5-1 to 5-4, the positive sense is toward the top of the page. The crenulated blade geometry in Figures 5-25 and 5-26 show excellent

agreement once again in this data format in the region from the central passage to the root wall, regardless of rotor movement. In Figure 5-25, the relative endwall movement produced a fairly uniform contour region of -20 degrees in the tip area ($z=-0.9$). This is in contrast to the regular blade contours in Figure 5-27 where the turning angles were generally a maximum of -10 degrees. In general the reduction in turning angles for the crenulated blades in this region is attributed to the difference in the vortex development between the two blade geometries. First, the tip region of Figure 5-4 shows stronger vw-components (longer arrows meaning larger magnitude) of the vortex formed below blade 4 without the presence of the rotor, than the vw-components of the equivalent vortex created by the crenulated blade in Figure 5-2. With the rotor present and spinning at 2200 rpm, the crenulated blades in Figure 5-1 produce greater magnitude vw-components in the region of coordinate $z=-0.9$ when compared to the same location in Figure 5-2 for the regular blades. In the root region, the effect is not nearly as dramatic with the regular blade (with and without rotor) producing predominant values in between the blades of -2.0 degrees, whereas for the crenulated blades a larger portion of the root region between the blades show -4.0 degrees. The largest negative values of turning angle for both types of blades in the root region were -10 degrees. Using the procedure discussed in Chapter II for calculation of the turn angle, the passage mass-averaged turning angle for the crenulated blade at $\phi = 0.52$ was found to be 26.44 degrees. This is 1.33 degrees less than the regular blade, which produced a turning angle of 27.77 degrees. For the no rotor cases, with an axial velocity of 164.3 ft/s (50.1 m/s), the crenulated blades produced a

25.54 degree passage mass-averaged turning angle, while the regular blade for the no rotor case produced a 27.51 degree turning angle.

Summary

Figure 5-29 shows the passage and region loss coefficients for the crenulated and regular blades. Although the region loss coefficients are subject to interpretation, they are included to support the trend in the overall passage loss data. The passage loss coefficients for both blade geometries agree within 1.0 % at all flow coefficients, well within the error bounds computed earlier. The central passage loss coefficient is inconsequential to the overall losses but shows a smooth decrease as supported by Horlock (1973) that increased Reynolds number (or equivalently in this research, increased flow coefficient) will reduce the mass averaged passage loss coefficient. The overall passage loss coefficient does not follow this trend, impacted by the root and tip region which both increase from $\phi = .40$ to $\phi = 0.52$ and then decreases as the flow coefficient is increased beyond 0.52. The flow coefficient $\phi = 0.72$ was included in this research to support this trend. Looking at the root and tip walls of the tunnel cascade, the compressor blades are located at approximately 10 in (0.30 m) from the bellmouth exit of the stilling tank. This corresponds to a flat plate Reynolds number on the order of 6.5×10^5 for the inlet velocity of 125.6 ft/s (38.3 m/s) or $\phi = 0.40$. Kuethe and Chow (1986:231) state that for a flat plate, any Reynolds number above about 2×10^5 can be laminar, turbulent, or transitional depending on the flow and wall surface conditions. The Reynolds number for the tunnel walls at the compressor blade location is most probably in transition, causing the initial increase in the tip and root regional pressure loss coefficients.

As the inlet velocity is increased, the flow becomes turbulent, whereupon the loss coefficients start a steady decline, per Horlock's observations. The center region, free of boundary layer interaction, has a maximum Reynolds number of 1.78×10^5 and if approximated as a flat plate due to its low incidence angle, has maintained laminar flow throughout the range of flow coefficients. Figure 5-30, from White (1991:432), illustrates a typical skin friction coefficient, C_f , transitioning from laminar to turbulent at an approximate Reynolds number of 5×10^5 .

VI. Conclusions and Recommendations

Conclusions

The following conclusions were drawn from the results of this experimental study into the effects of changes in Reynolds number on the flow features of both regular and crenulated compressor blades within a linear cascade with moving endwall.

The analysis of the vw-component velocity vector plots produced from the hotwire show that the tip leakage vortex has largely dissipated 0.35 in (0.89 cm) or 23.0% chord behind the trailing edge of both the crenulated and regular blade rows, indicating that for a tip clearance of 1.0 % chord, this vortex is very weak. The dissipation of this vortex was seen by McMullan (1996) who observed that the tip leakage vortex weakens with reduced tip clearance. The blade root secondary flow vortex remains visible in both the crenulated and regular blade flowfields in the same plane. In the case of the regular blade, the flow interaction at the tip with the moving endwall created a steady velocity component along the suction side of the blade flowing spanwise toward the blade root, while the secondary vortex at the root creates a spanwise flow back toward the tip along the pressure side of the blade. The mid-span pair of crenulations of the crenulated blade produces rotating vortices that disrupt the spanwise flow that appears on the regular blade. This re-direction of the spanwise flow caused by the vortices of the crenulations contributes to the increased wake mixing seen by Veasart (1989), DeCook (1991), and Costello (1993). The flowfields without rotor movement confirm Peter's (1995) observations that for a

particular geometry the total pressure and velocity contours of the root and central regions of the passage remain relatively unchanged with endwall movement.

Examination of the tip region between blades 4 and 5 reveals that, at all flow coefficients tested, the local total pressure loss and local velocity contours are relatively insensitive to blade geometry at the rotor speed of 2200 rpms. Peter (1995) did not directly compare the two blade geometries at identical flow conditions but a close look in the tip region of the total pressure loss contours of, in order of tip clearances, Figures 27, 54, and 34 of his research, shows very little differences between Figure 54 (crenulated blade) and the other two plots at a rotor speed of 2000 rpms. McMullan (1996) showed that for a tip clearance of 1.0 % chord and rotor speed of 1700 rpms, the regular blade had a higher peak loss contour value and a larger region of loss influence into the passage over the crenulated design. This certainly indicates that at higher endwall velocities, geometry differences in the blade tips are overshadowed by the boundary layer interaction between the blade tip and the moving endwall. McMullan (1996) also found that the root region losses were similar for both regular and crenulated blades, a result that is supported by this research.

The local velocity contour plots indicated that at all flow coefficients tested, the wake reduction was less for the crenulated blade design. This has been seen by DeCook (1991) and Costello (1993). At the single flow coefficient of 0.52, the passage mass-averaged turning angle clearly indicated that the crenulated blade reduced the turning angle. This also has been seen in previous research but their computations only included a small portion of the central passage. The tip region of the turning angle contour plots do show

a difference between the blade geometries. The space provided by the crenulation in the tip region allows a larger portion of the relative endwall flow to sustain its downward momentum. In the case tested here the downward flow angle of the rotor air flow for the crenulated blade was twice that of the regular blade.

In summary, the crenulated blade, at the downstream location of 0.35 in (0.89 cm) or 23.0 % chord, for the flow coefficients and Reynolds numbers tested, showed no change in total pressure losses, a reduction in turn angle, increased wake mixing, and a reduction in wake deficit. The high rotor speed and the fact the data plane was so close to the trailing edges of the blade cascade is considered the reason that total pressure losses seen by McMullan (1996) were not observed in the present study. Endwall motion approaching the speeds seen in actual engine operation seems to mask any differences between the blade geometries.

Recommendations

Limitations in the moving endwall configuration when mated to the linear cascade precluded changing the angle of incidence of the blades. Since Costello (1993) saw the majority of the advantages in total pressure losses at high incidence angles for the crenulated blades, the rotor configuration should be modified to enable variable incidence testing. Another needed modification to the rotor is rotor speed, which at present is the limiting factor in having both a realistic flow coefficient for normal engine operation and a Reynolds number normal to engine operation. Changes in motor to rotor gear ratio were attempted but the tight clearances of the supporting framework of the stand and motor precluded any significant alterations. Even if the motor was operated at its top no-load

rated rpm of 2500 the rotor edge speed would be around 354 ft/s (108 m/s) so at a flow coefficient of 0.70 the Reynolds number would be just under 2×10^5 . In order to realize flow Reynolds numbers above 2×10^5 the motor must be more powerful than it's present one horsepower and be rated at a higher rpm than 2500.

References

- Allison, D.M., "Design and Evaluation of a Cascade Test Facility," MS Thesis GAE/AA/81D-2, Air Force Institute of Technology (AU), Wright-Patterson AFB, OH, June 1982.
- Bruun, H. H., Hot-Wire Anemometry (First Edition). Oxford University Press, Inc, New York, 1995.
- Cohen, H., Rogers, G.F.C. and Saravanamutto, H.I.H., Gas Turbine Theory (Third Edition). John Wiley and Sons, New York, 1987.
- Costello, M. J., "Off-Design Performance of Crenulated Blades in a Linear Compressor Cascade," MS Thesis GAE/ENY/93D-1, Air Force Institute of Technology (AU), Wright-Patterson AFB, OH, December 1993.
- DeCook, S.J., "Experimental Investigation of Trailing Edge Crenulation Effects on Losses in a Compressor Cascade," MS Thesis GAE/ENY/91D-1, Air Force Institute of Technology (AU), Wright-Patterson AFB, OH, December 1991.
- Herzig, H.Z., Hansen, A.G. and Costello, G.R., "A Visualization Study of Secondary Flows in Cascades," NACA Rep 1163, 1954.
- Horlock, J.H., Axial Flow Compressors. Robert E. Krieger Publishing Company, Huntington, New York, 1973.
- Kang, S. and Hirsch, C., "Experimental Study on the Three-Dimensional Flow Within a Compressor Cascade With Tip Clearance: Part I - Velocity and Pressure Fields," Transactions of ASME, Journal of Turbomachinery, V115, pp 435-443, July 1993.
- Kang, S. and Hirsch, C., "Experimental Study on the Three-Dimensional Flow Within a Compressor Cascade With Tip Clearance: Part II - The Tip Leakage Vortex," Transactions of ASME, Journal of Turbomachinery, V115, pp 435-443, July 1993.
- Kuethe, A. M., and Chow, C., Foundations of Aerodynamics (Fourth Edition). John Wiley and Sons, New York, New York, 1986.
- Lakshminarayana, B. "An Axial Flow Research Compressor Facility Designed for Flow Measurements of Rotor Passages," Journal of Fluids Engineering, Vol 102, December 1980, pp 402-411.

McMullan, R. J., "Influence of Tip Clearance on the Flowfield in a Compressor Cascade With a Moving Endwall," MS Thesis GAE/ENY/96D-5, Air Force Institute of Technology (AU), Wright-Patterson AFB, OH, December 1996.

Oates, G. D., Aerothermodynamics of Aircraft Engine Design Components, American Institute of Aeronautics and Astronautics, Inc., New York, New York, 1985.

Peter, L.J., "Influence of a Moving Wall on the Tip Clearance Vortex in an Axial Compressor Cascade," MS Thesis GAE/ENY/95D-19, Air Force Institute of Technology (AU), Wright-Patterson AFB, OH, December 1995.

Pougare, M., Galmes, J., and Lakshminarayana, B. "An Experimental Study of the Compressor Rotor Blade Boundary Layer," ASME Journal of Engineering for Gas Turbines and Power, Vol 107, No.2, April 1985 pp 364-373.

Pouagare, M., Murthy, K. N. S., and Lakshminarayana, B. "3-D Flow Field Inside the Passage of a Low-Speed Axial Flow Compressor," AIAA Paper 82-1006, 1982.

PSI 8400 Pressure Scanner User's Manual, Hampton, VA: Pressure Systems, Incorporated, March 1993.

Spacy, W.L. II, "Effects of Crenulations on Three-Dimensional Losses in a Compressor Cascade," MS Thesis GAE/ENY/93D-1, Air Force Institute of Technology (AU), Wright-Patterson AFB, OH, December 1993.

Veesart, J.L., "Wake Dissipation and Total Pressure Loss in a Two-Dimensional Compressor Cascade With Crenulated Trailing Edges," MS Thesis GAE/AA/89J-3, Air Force Institute of Technology (AU), Wright-Patterson AFB, OH, June 1989.

Wennerstrom, A.J., "Vane Configuration for Fluid Wake Re-energization," United States Patent Number 4,318,669 1982.

White, F. M., Viscous Fluid Flow (Second Edition). McGraw-Hill, Inc, New York, New York, 1991.

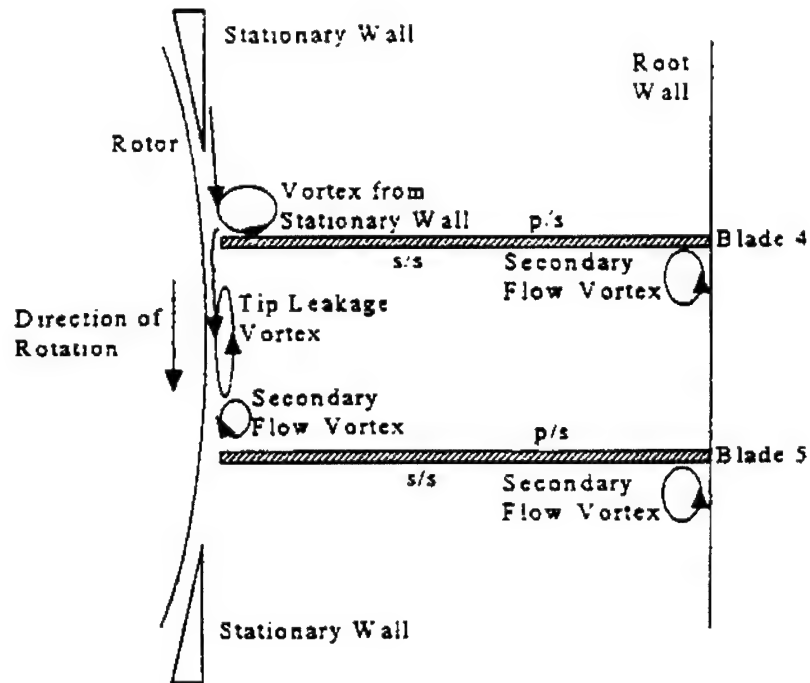


Figure 2-1. Linear Compressor Cascade with Moving Endwall Flowfield Description (McMullan, 1996:7-1)

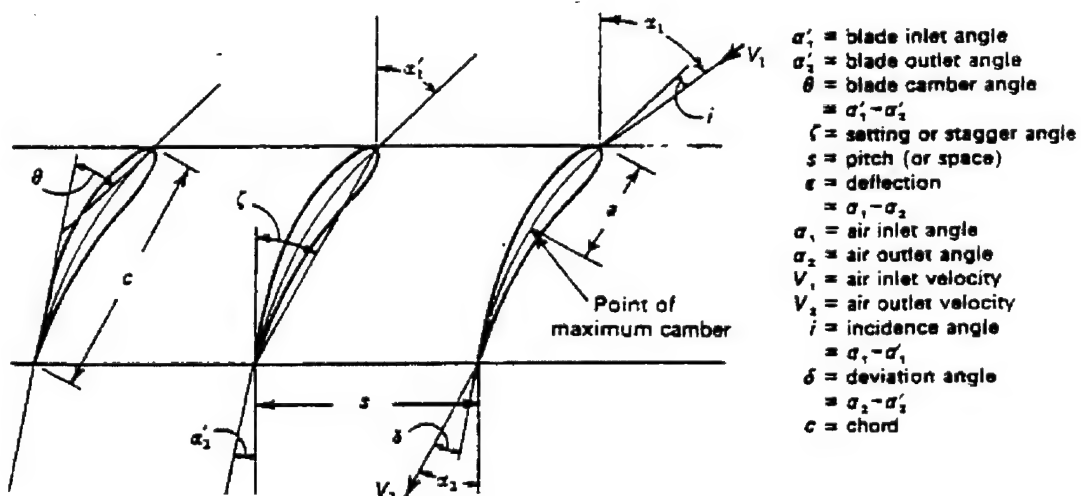


Figure 2-2. Cascade Nomenclature (adapted from Cohen et al, 1987)

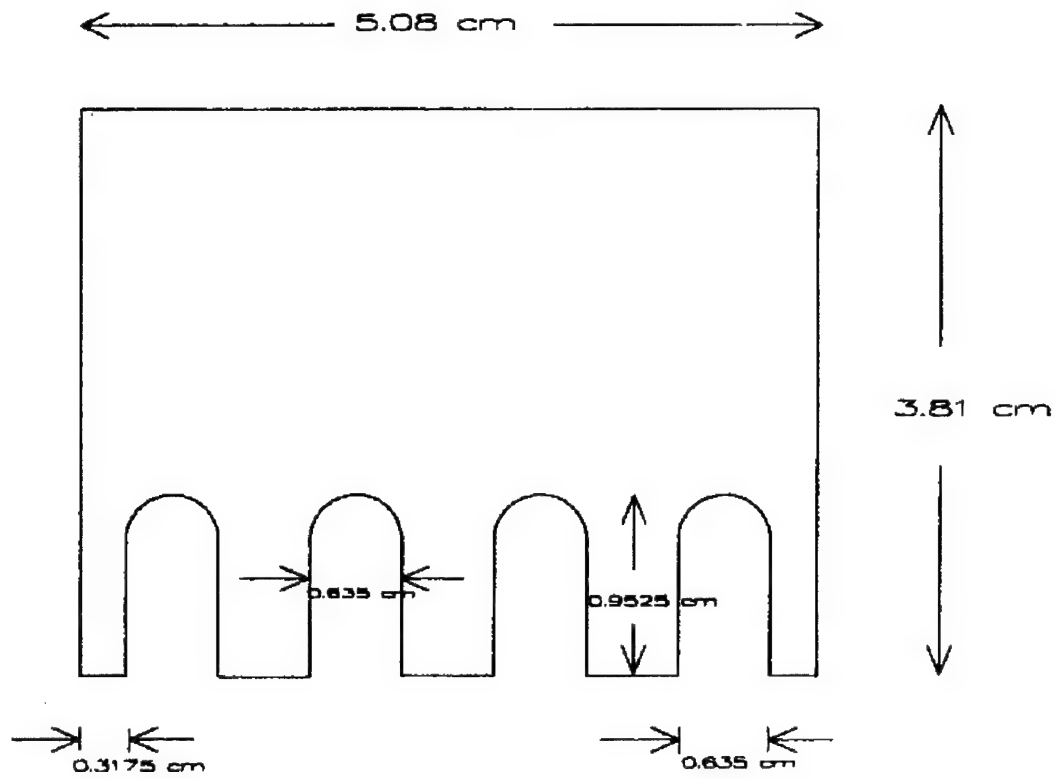


Figure 2-3. Crenulated Blade Geometry (McMullan, 1996:7-3)

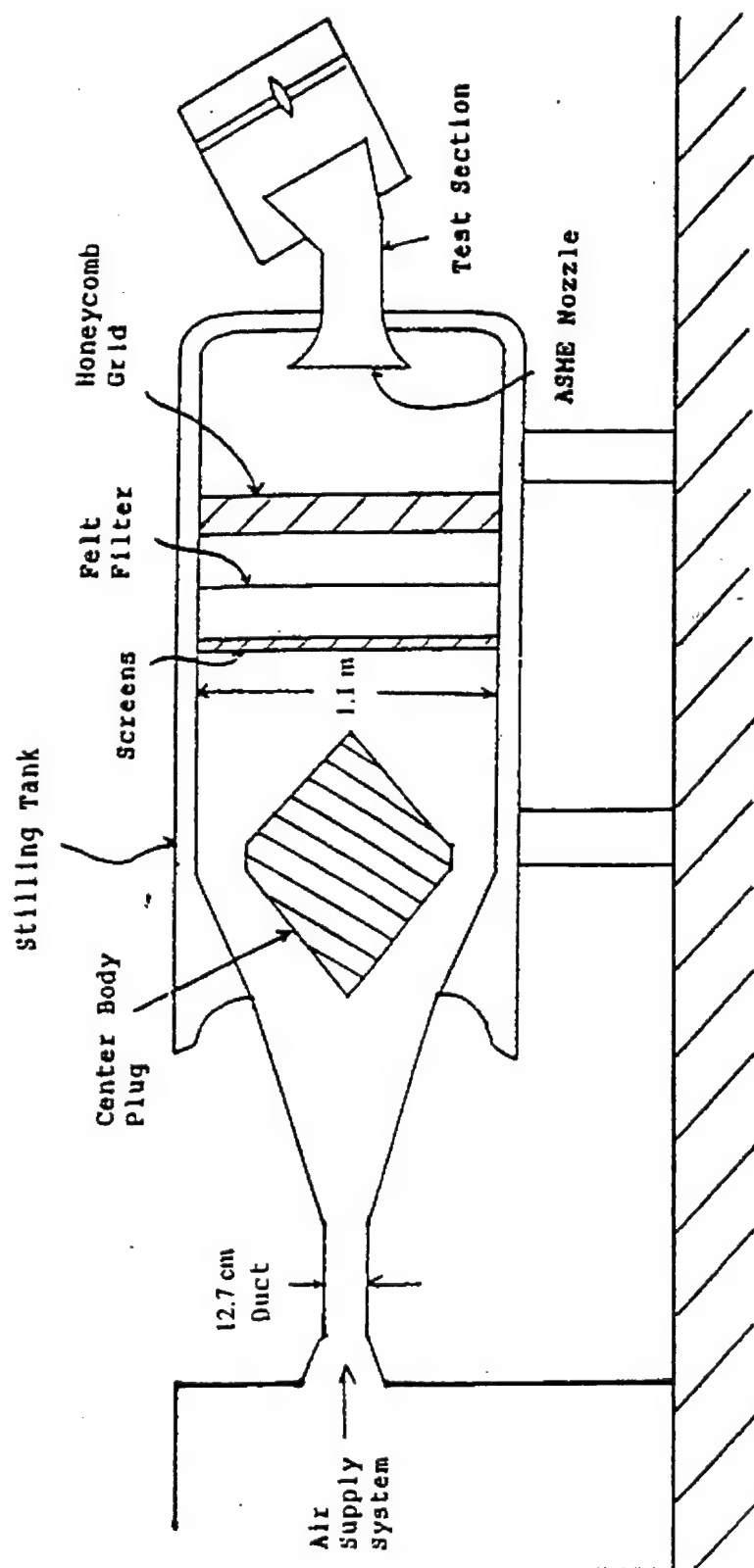


Figure 3-1. Air Supply System and Diffuser/Stilling Chamber (Costello, 1993:69)

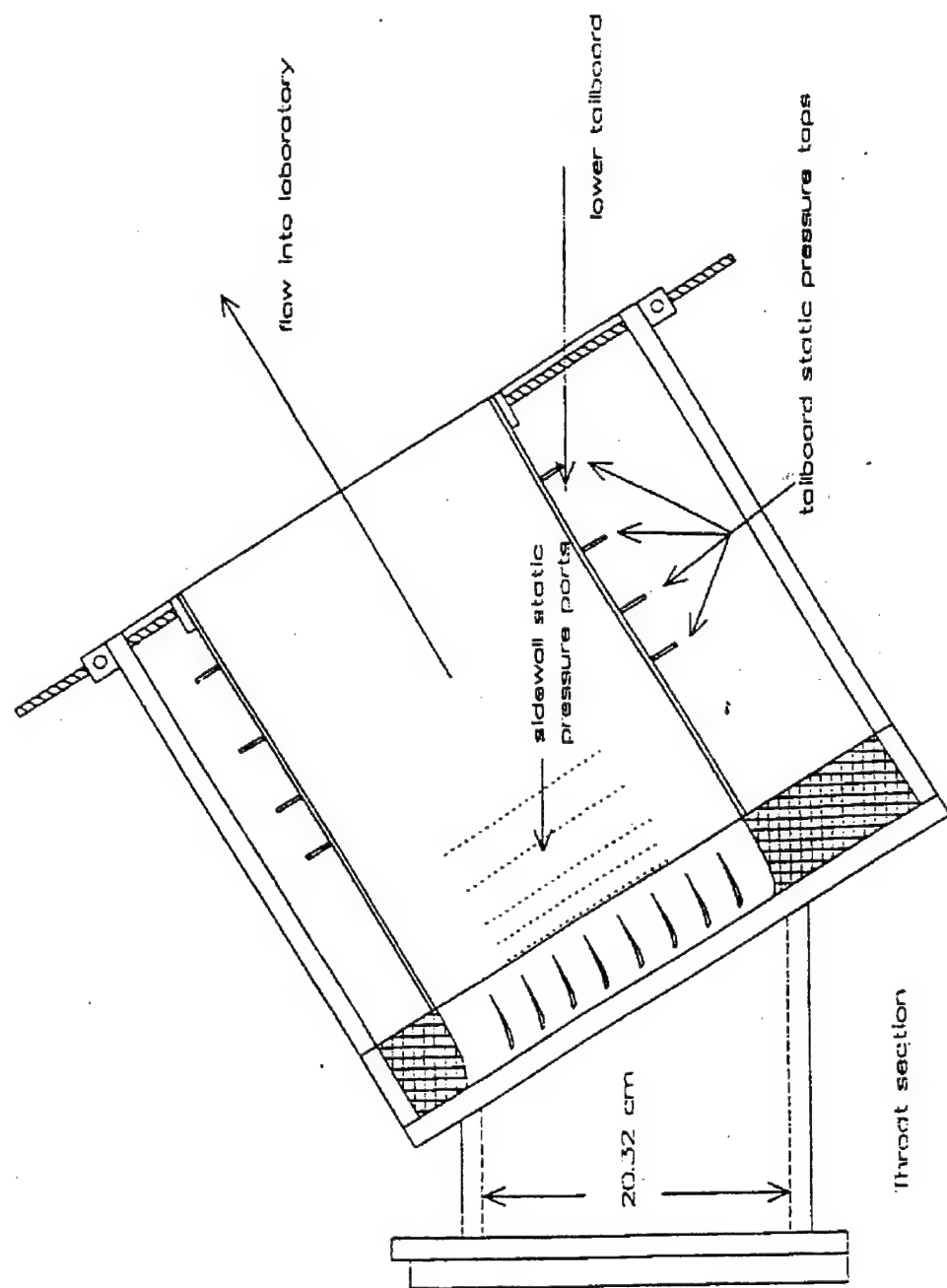


Figure 3-2. Cascade Test Section (Peter, 1995:7-6)

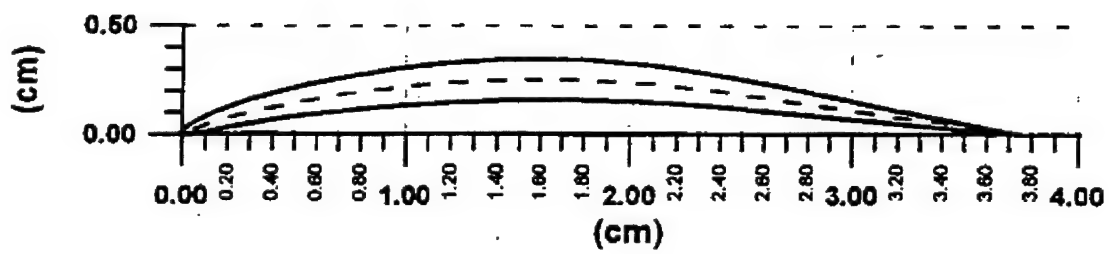


Figure 3-3. Blade Profile NACA 64-A905 (Peter, 1995:7-8)

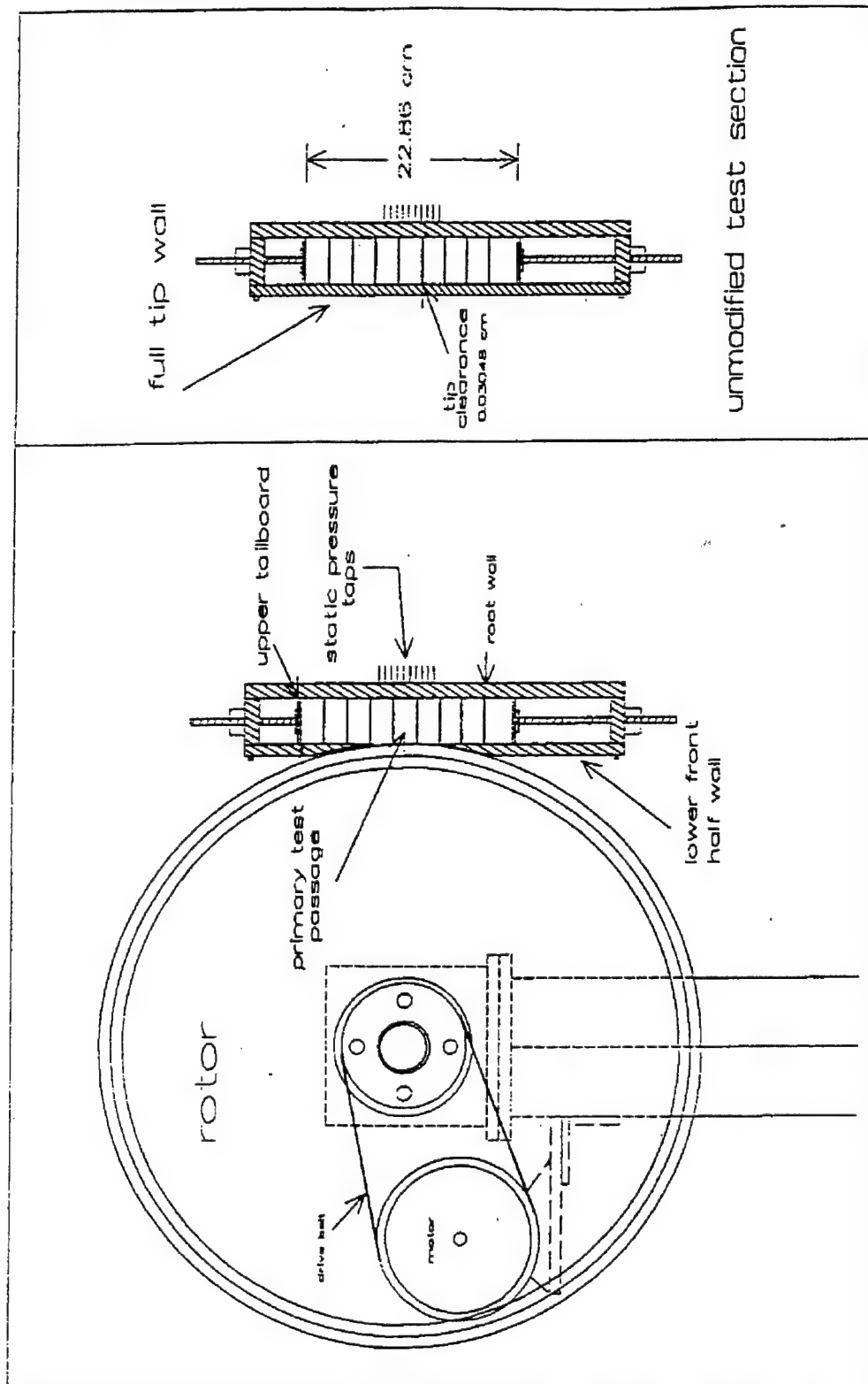


Figure 3-4. Rotor and Test Section Integration (Peter, 1995:7-4)

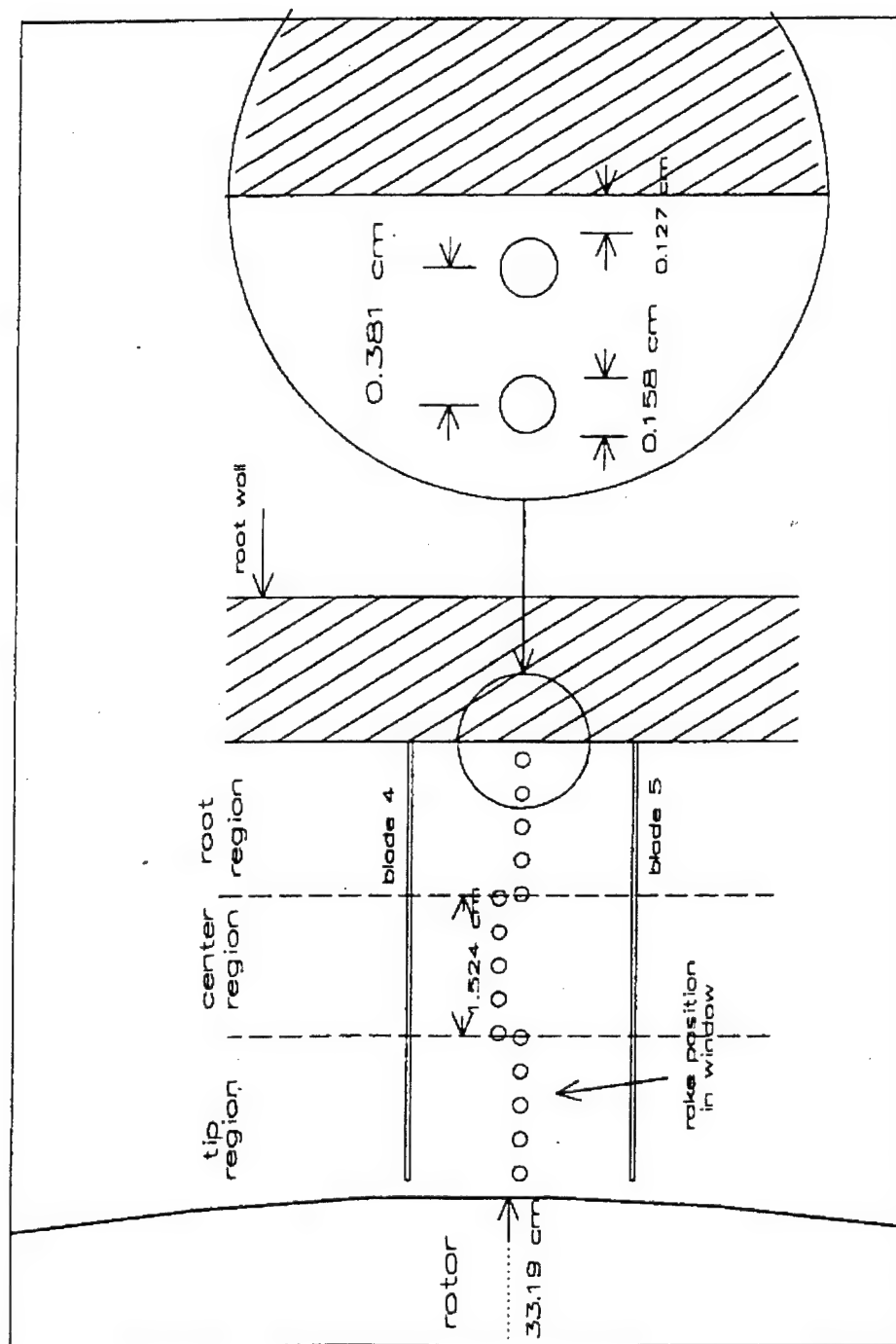


Figure 3-5. Total Pressure Rake Testing Region (McMullan, 1996:7-9)

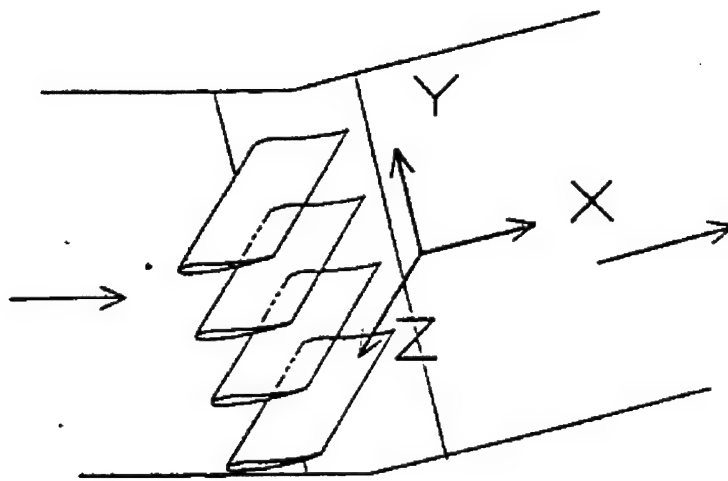


Figure 3-6. Cascade Coordinate System (Peter, 1995:7-5)

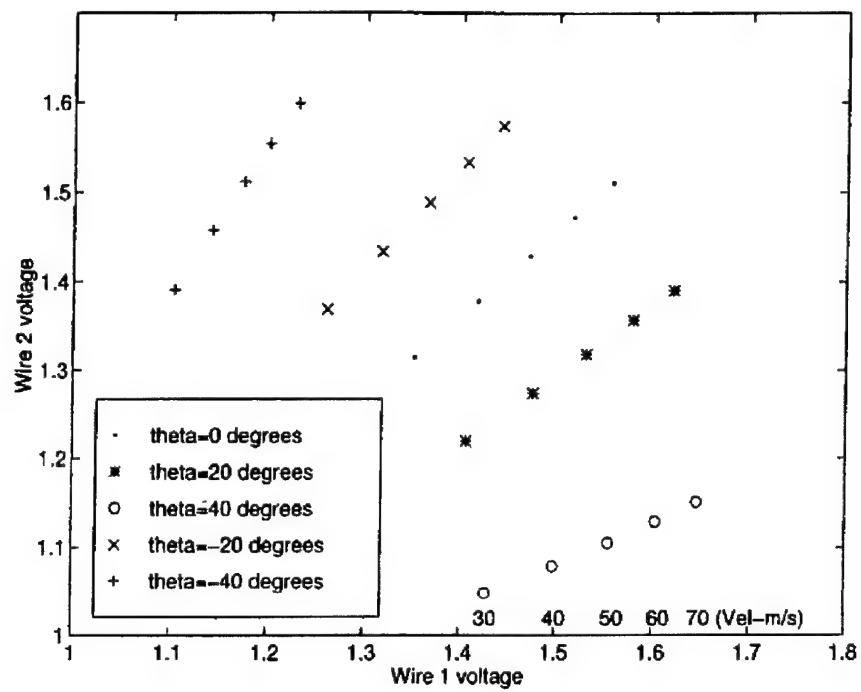


Figure 4-1. Hotwire Calibration Raw Voltage Data

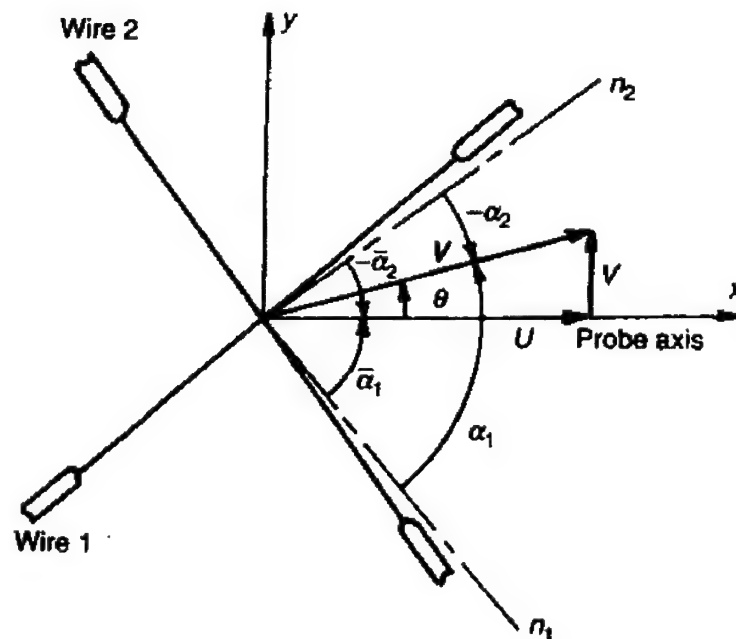


Figure 4-2. Hotwire Geometry (Bruun, 1995:148)

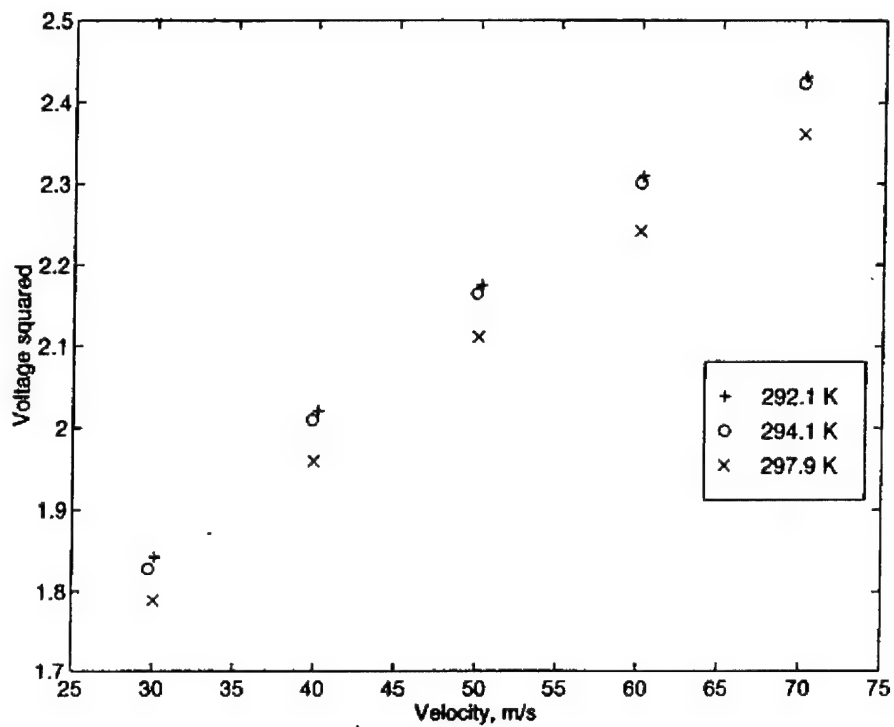


Figure 4-3. Hotwire 1 Voltage Variation with Fluid Temperature Change

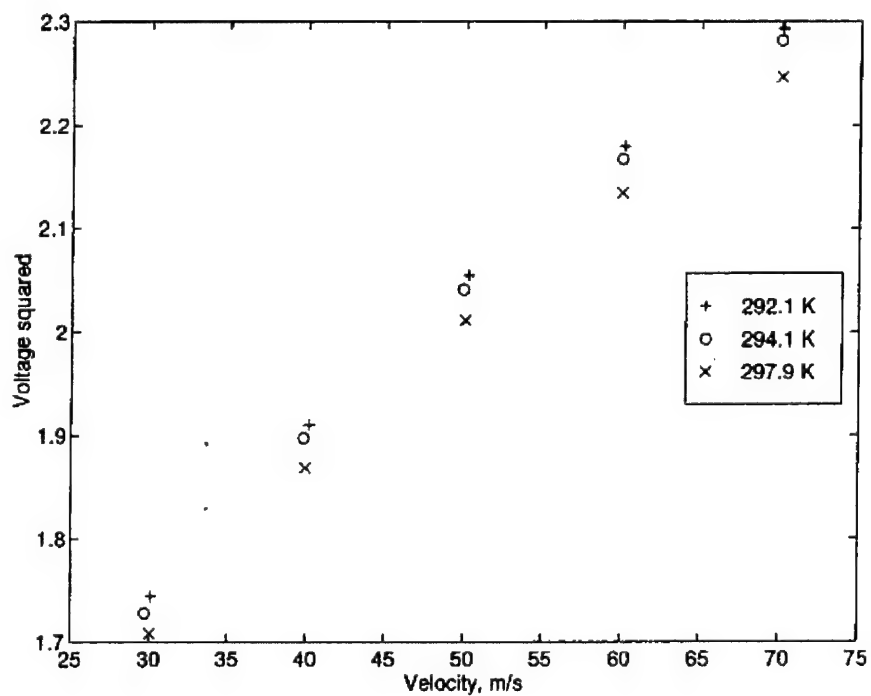


Figure 4-4. Hotwire 2 Voltage Variation with Fluid Temperature Change

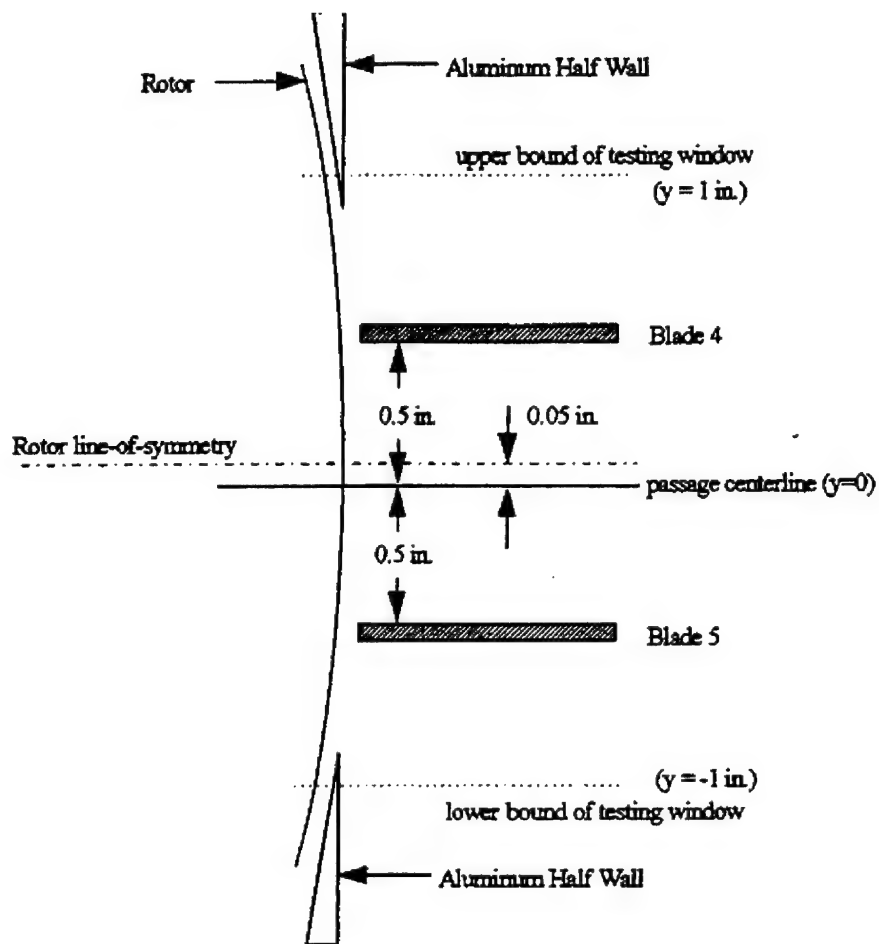


Figure 4-5. Cross-Section of Rotor and Middle Blade Passage (McMullan, 1996:7-5)

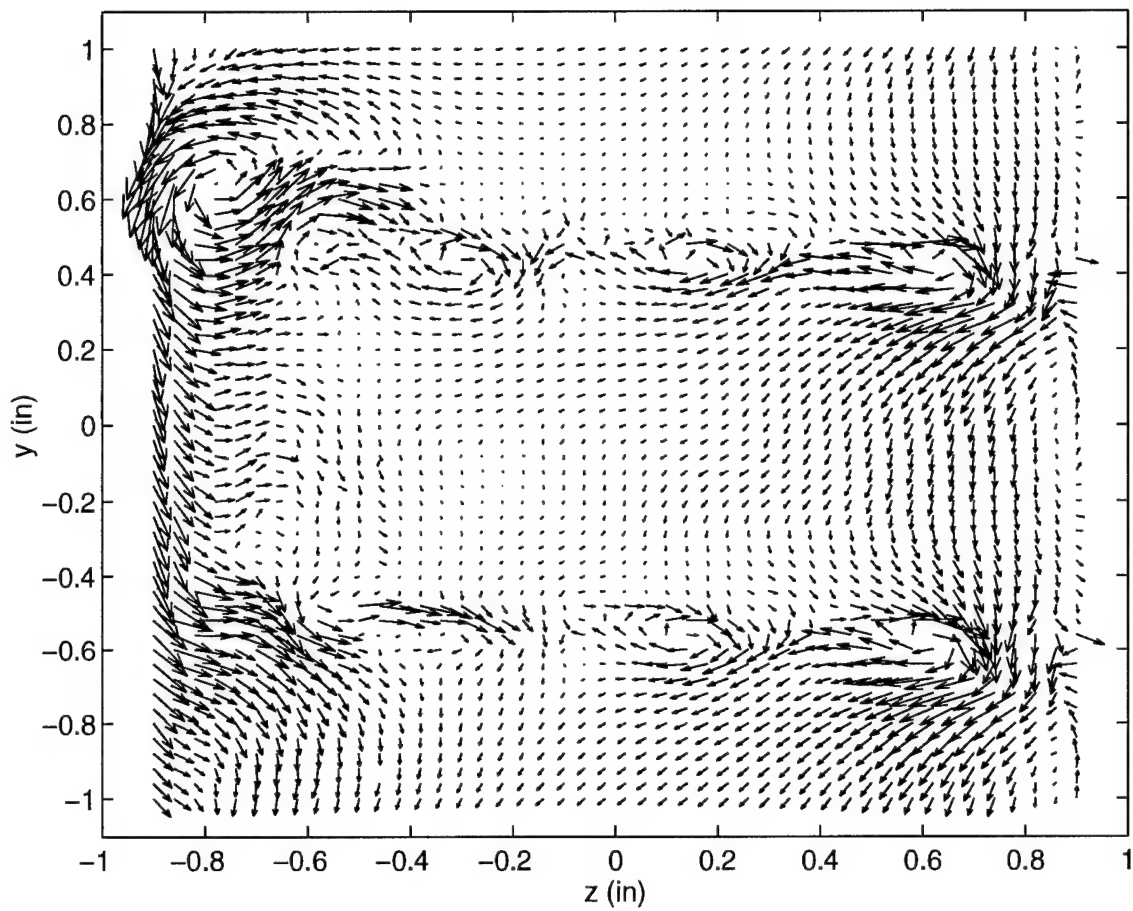


Figure 5-1. Velocity vectors - vw components $\phi = 0.52$ (Crenulated Blade)

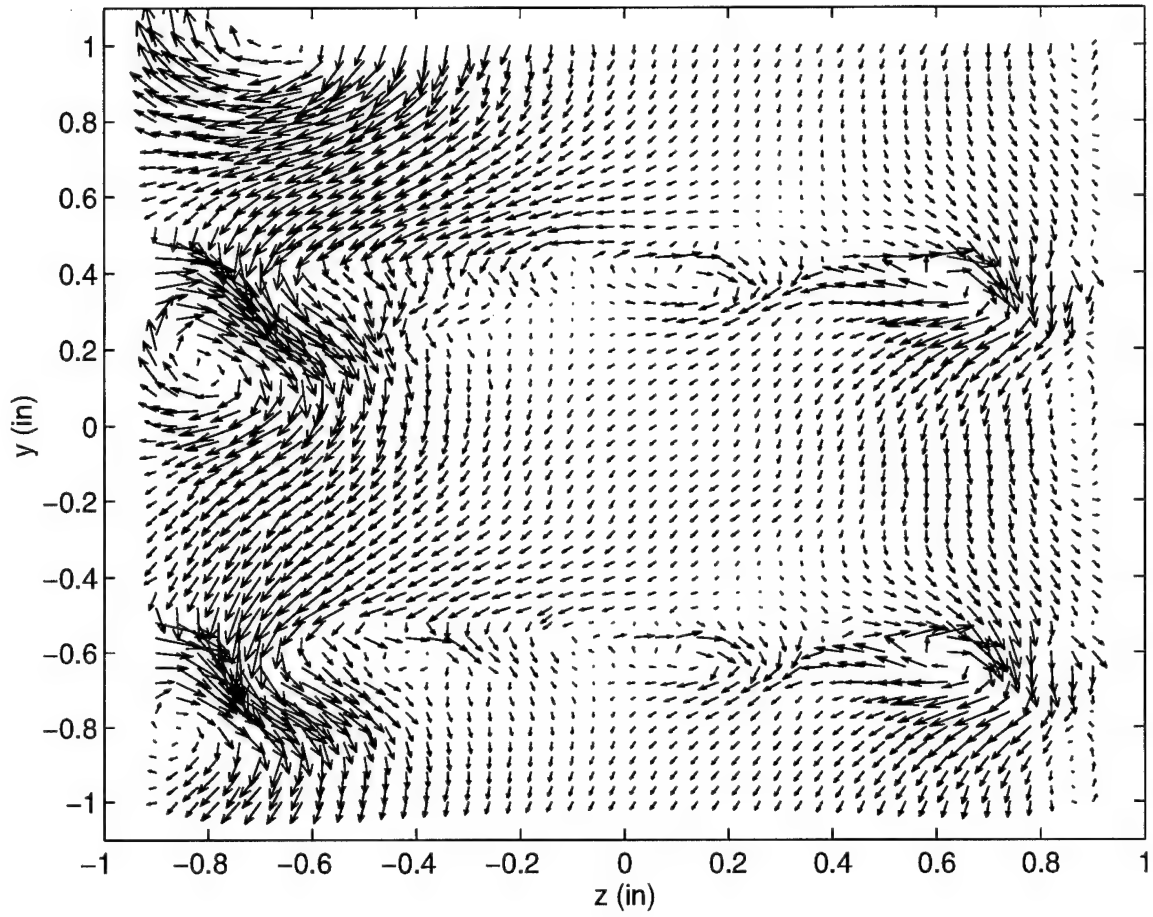


Figure 5-2. Velocity vectors - vw components $U_x = 164.3$ ft/s (Crenulated Blade-no rotor)

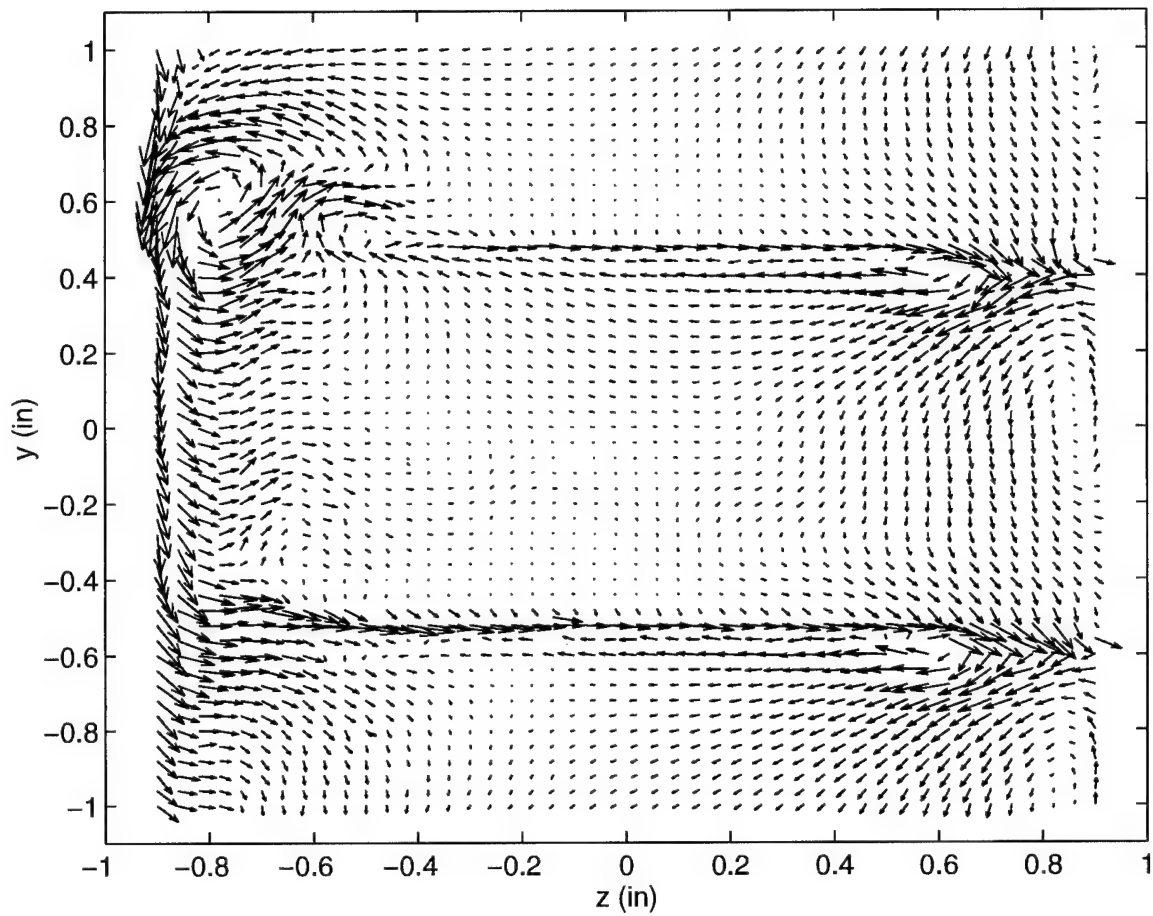


Figure 5-3. Velocity vectors - vw components $\phi = 0.52$ (Regular Blade)

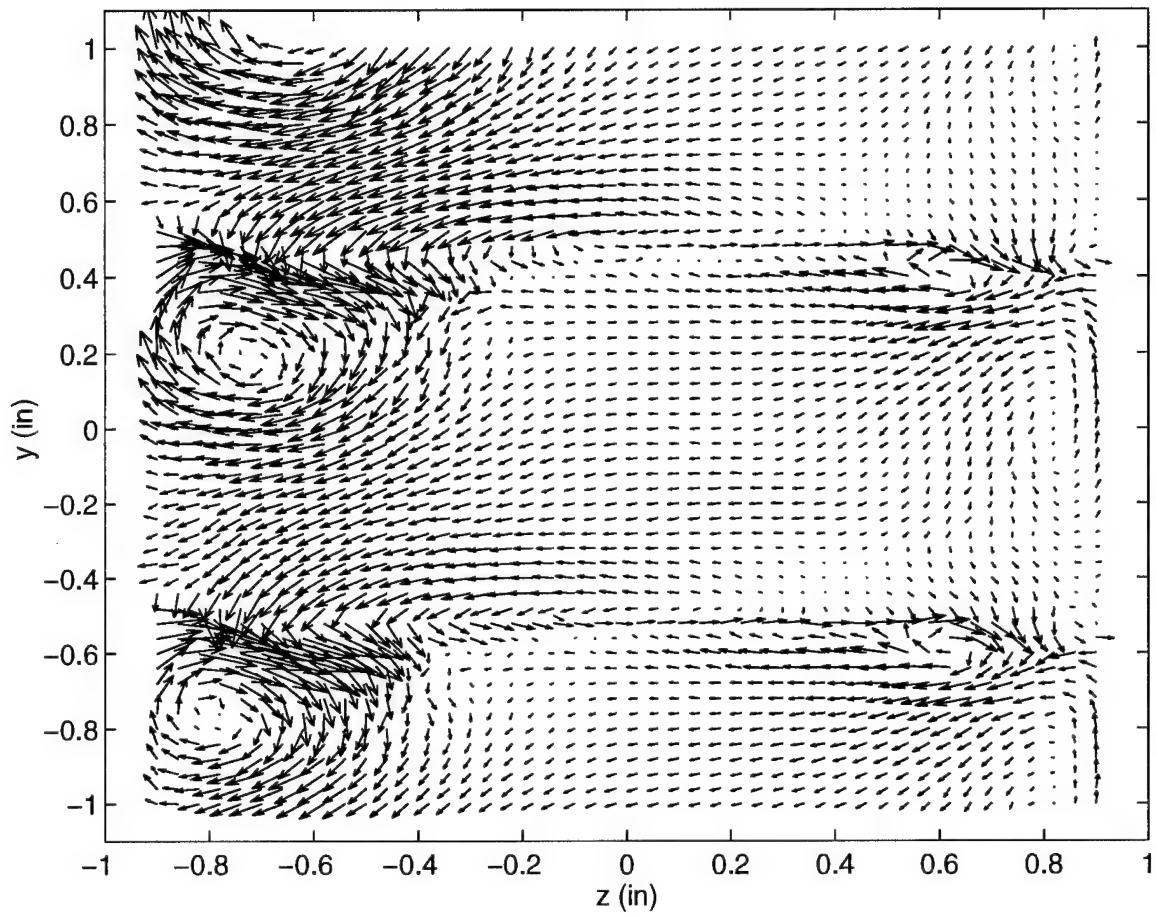


Figure 5-4. Velocity vectors - vw components $U_x = 164.3$ ft/s (Regular Blade-no rotor)

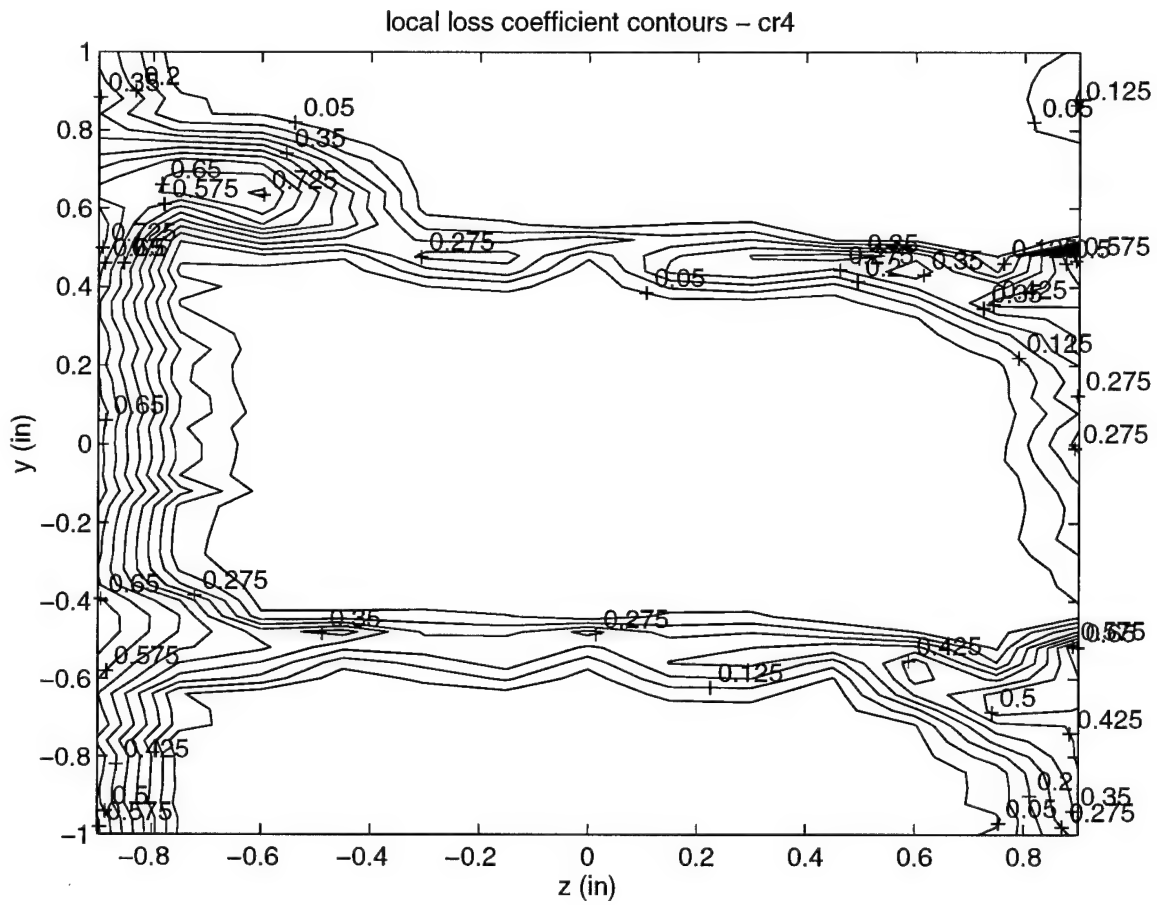


Figure 5-5. Local total pressure loss contour plot $\phi = 0.40$ (Crenulated Blade)

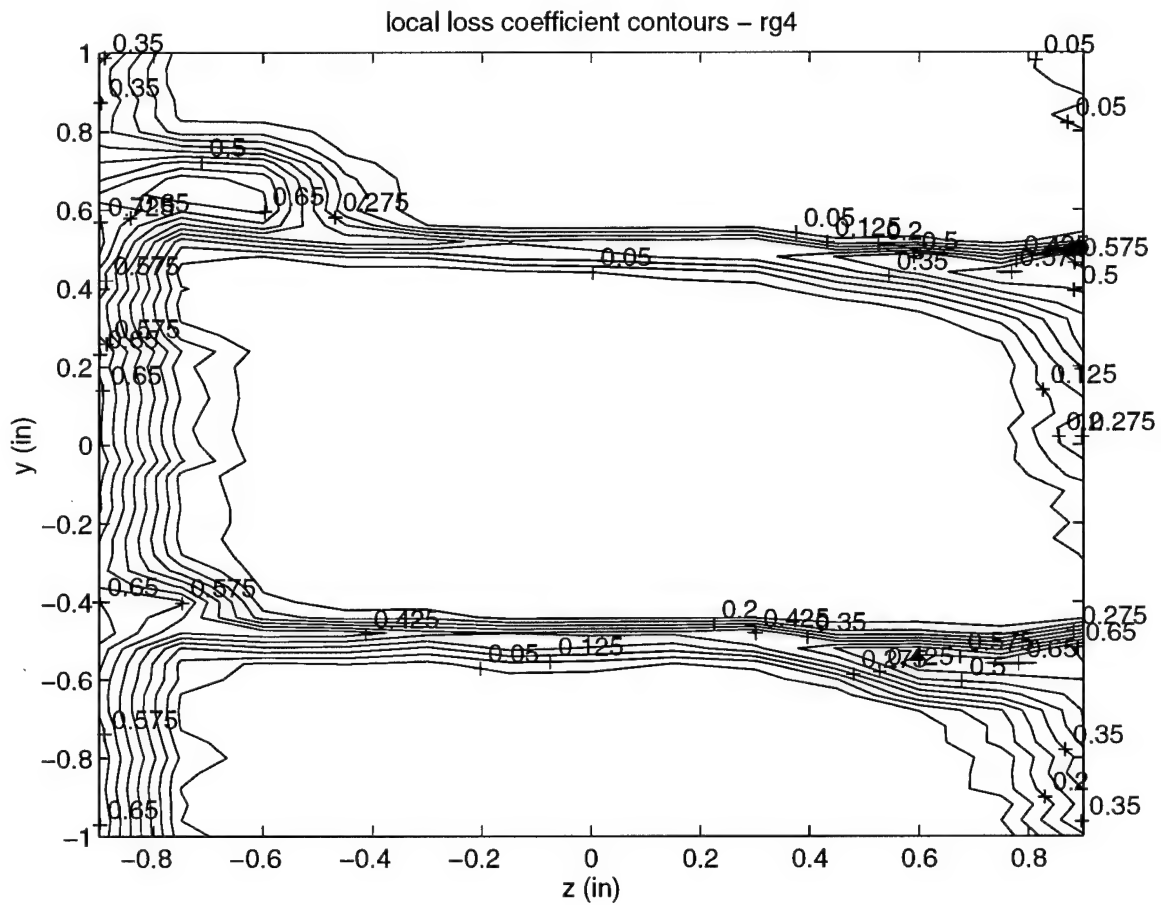


Figure 5-6. Local total pressure loss contour plot $\phi = 0.40$ (Regular Blade)

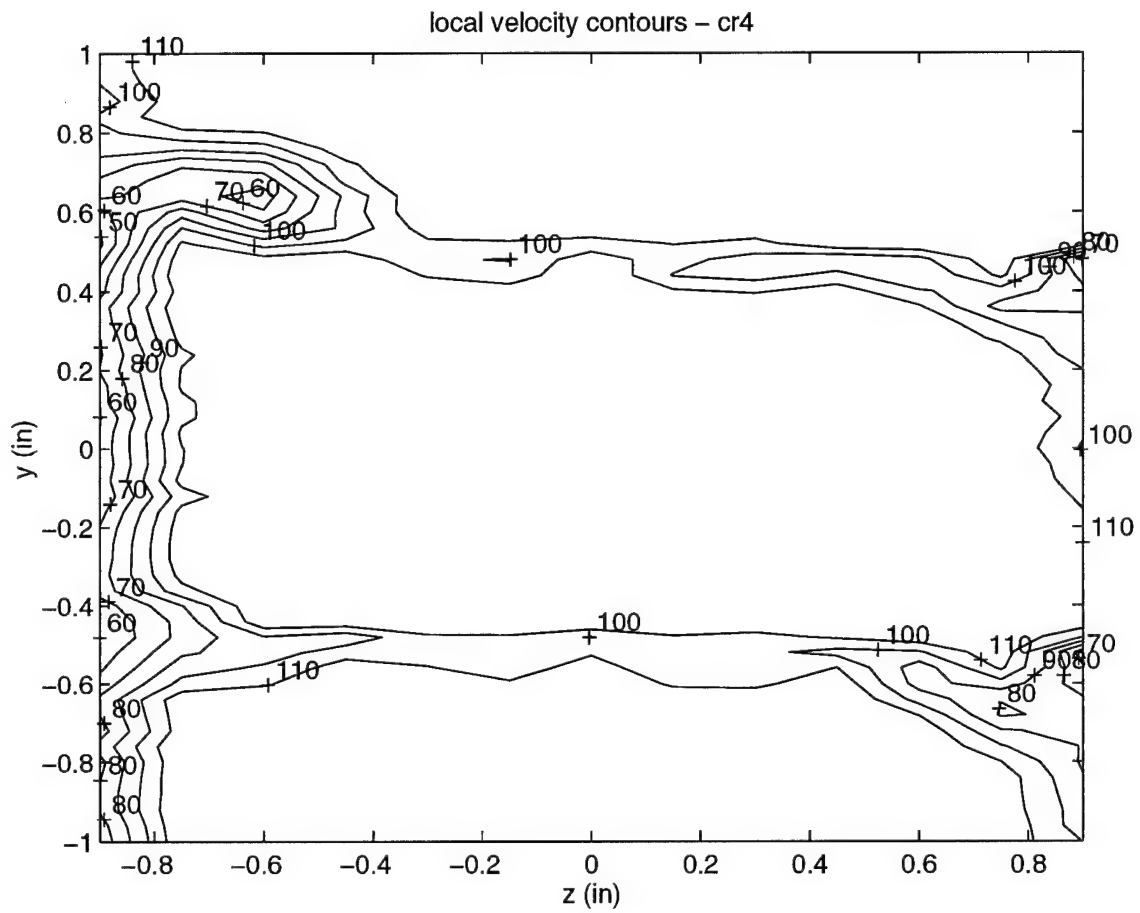


Figure 5-7. Local velocity contour plot $\phi = 0.40$ (Crenulated Blade)

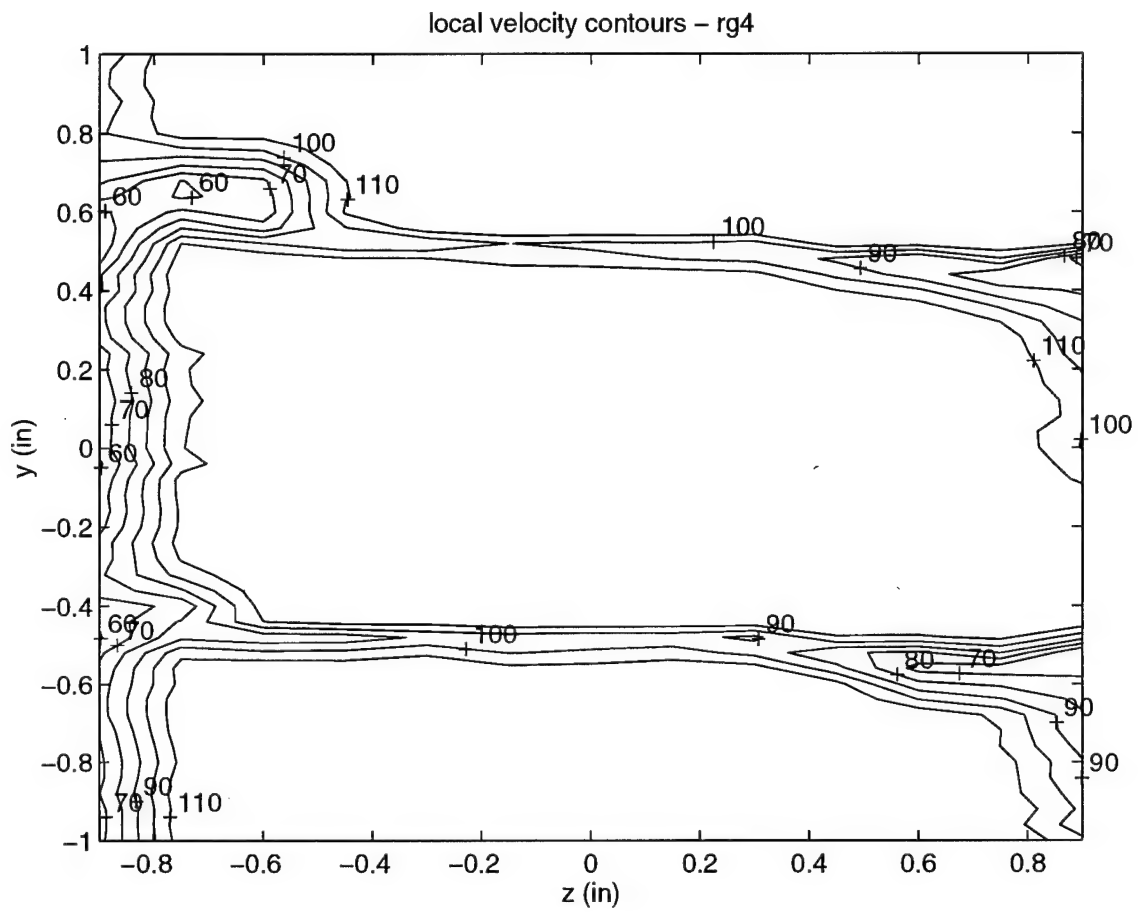


Figure 5-8. Local velocity contour plot $\phi = 0.40$ (Regular Blade)

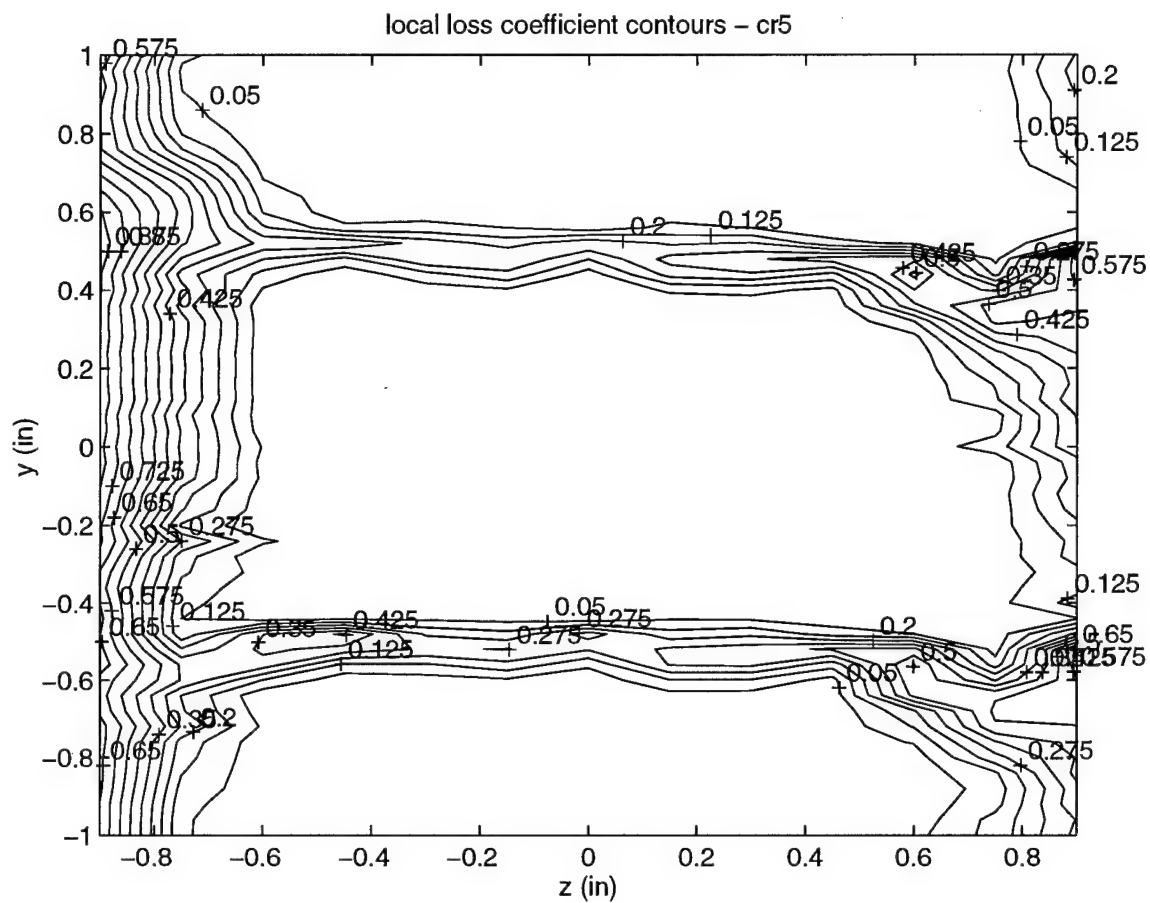


Figure 5-9. Local total pressure loss contour plot $\phi = 0.52$ (Crenulated Blade)

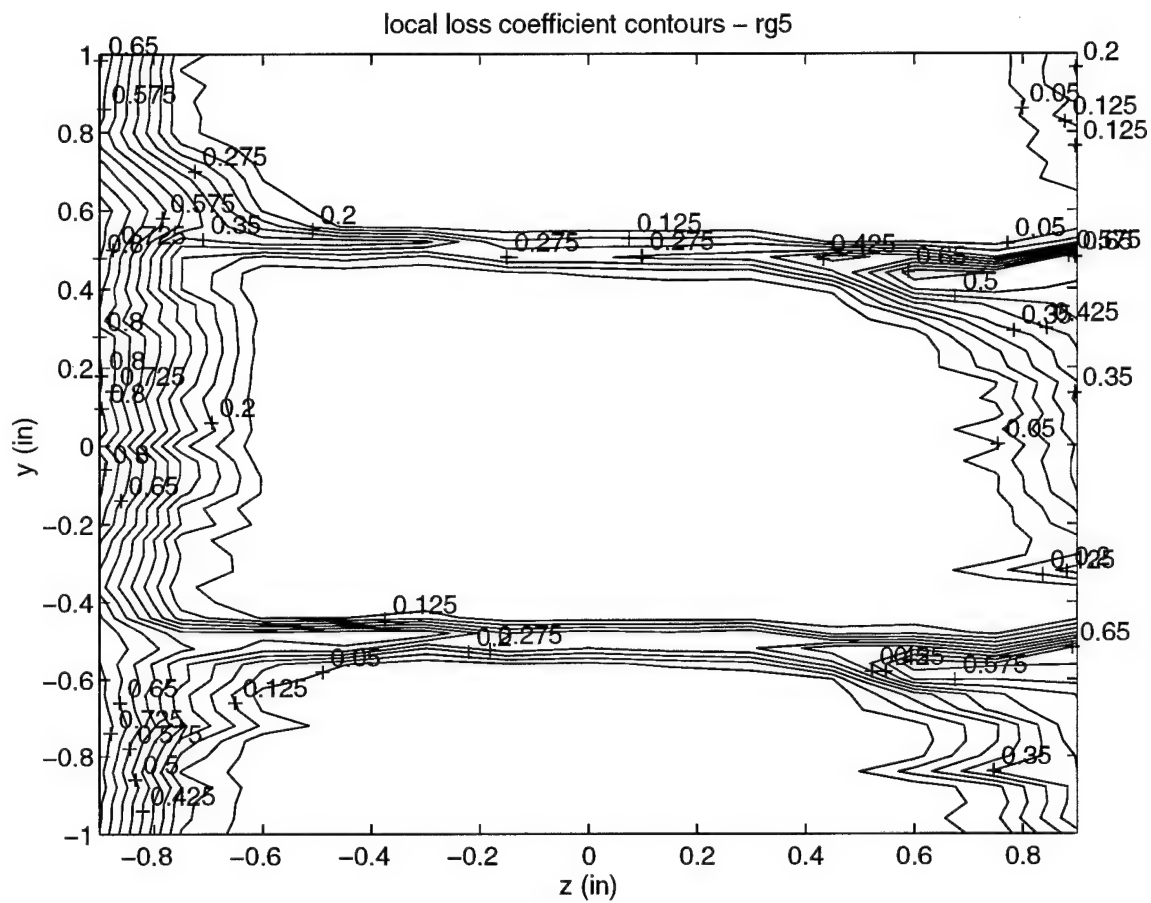


Figure 5-10. Local total pressure loss contour plot $\phi = 0.52$ (Regular Blade)

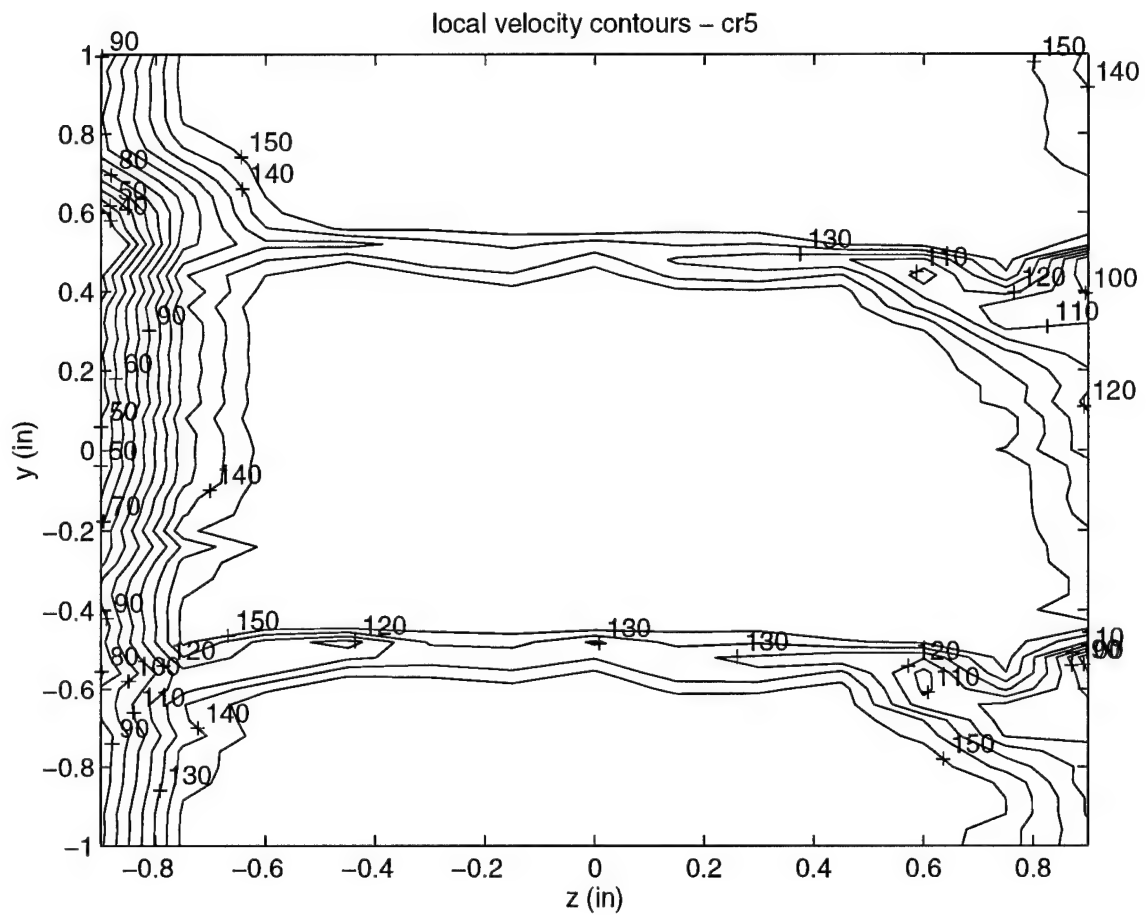


Figure 5-11. Local velocity contour plot $\phi = 0.52$ (Crenulated Blade)

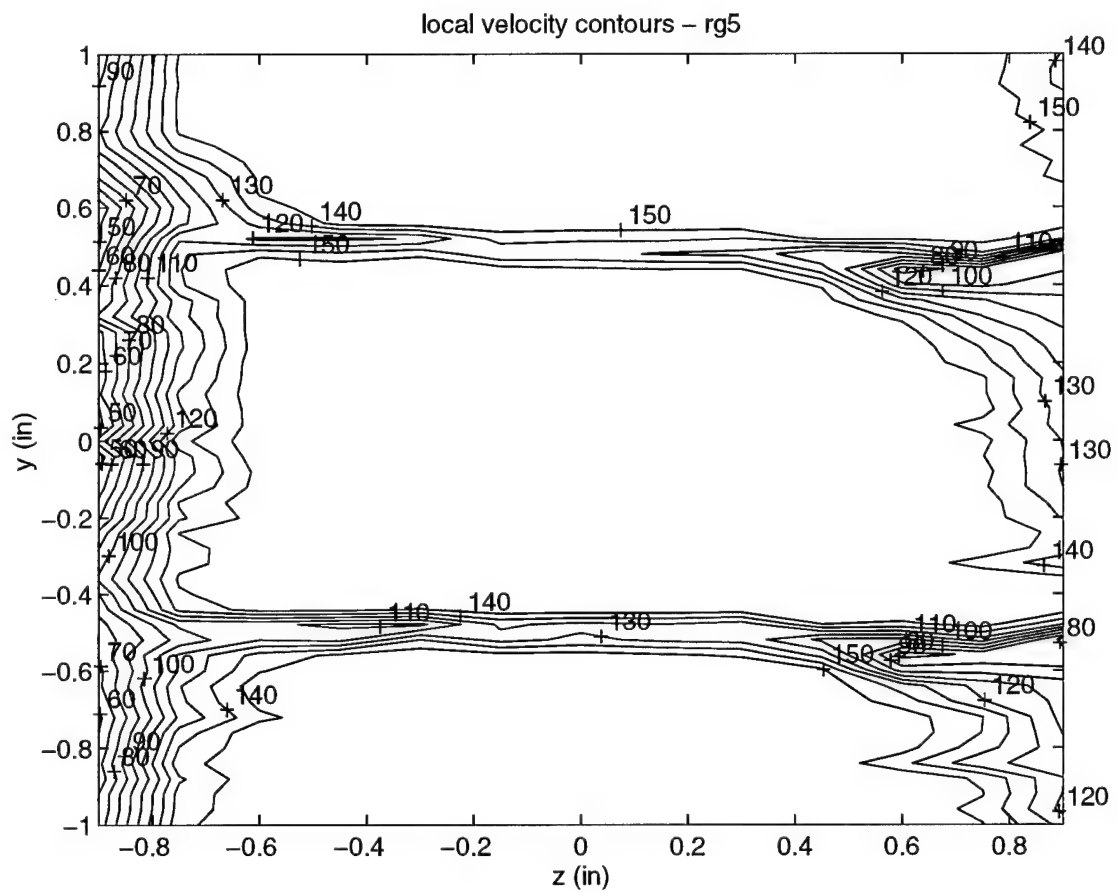


Figure 5-12. Local velocity contour plot $\phi = 0.52$ (Regular Blade)

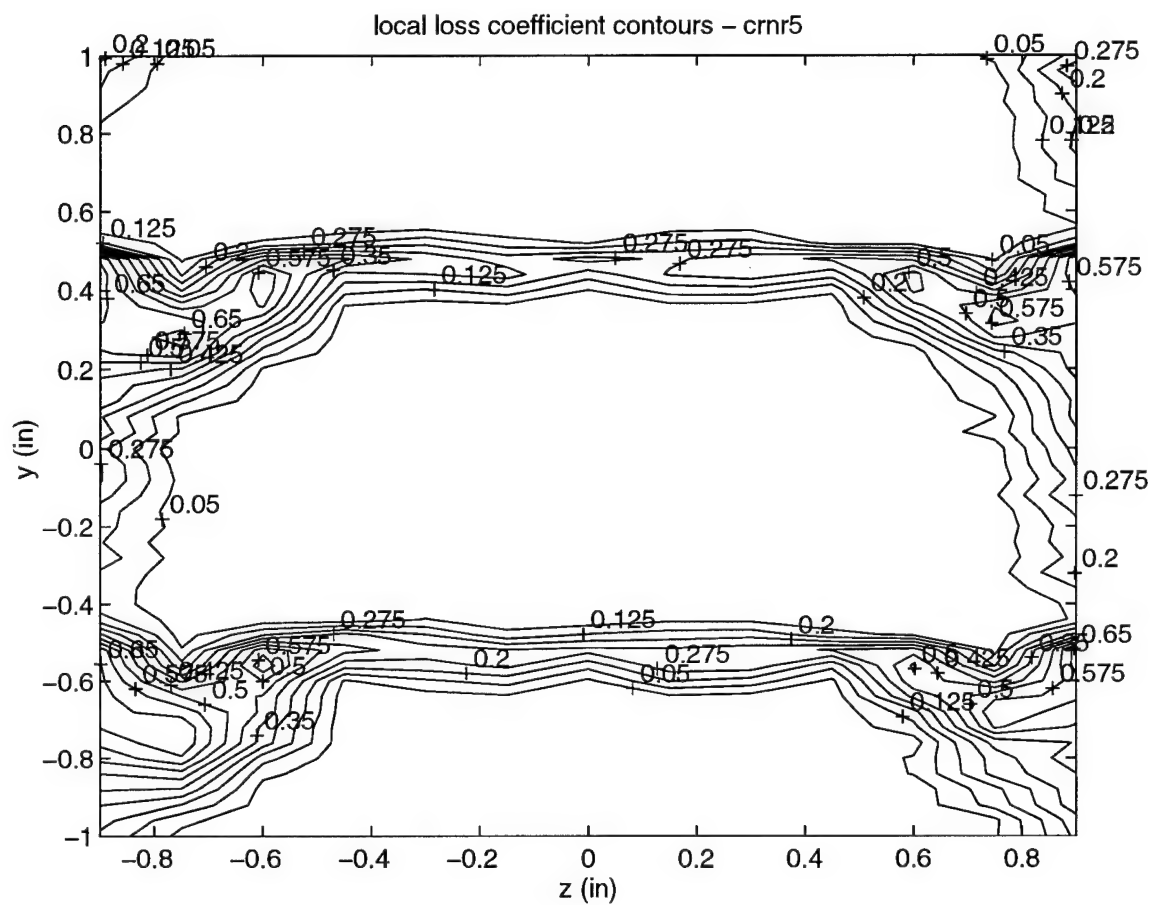


Figure 5-13. Local total pressure loss contour plot $U_x = 164.3$ ft/s (Cren. Blade-no rotor)

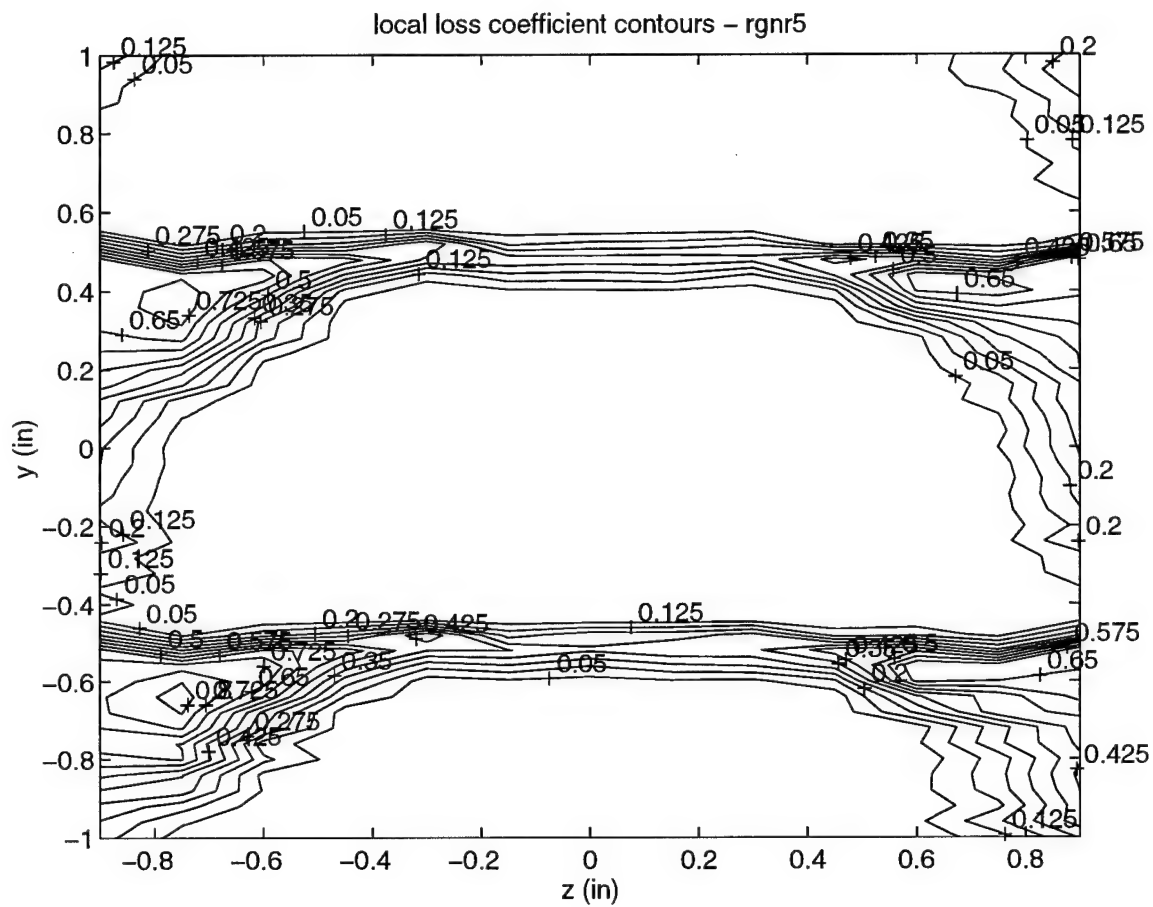


Figure 5-14. Local total pressure loss contour plot $U_x = 164.3$ ft/s (Reg Blade-no rotor)

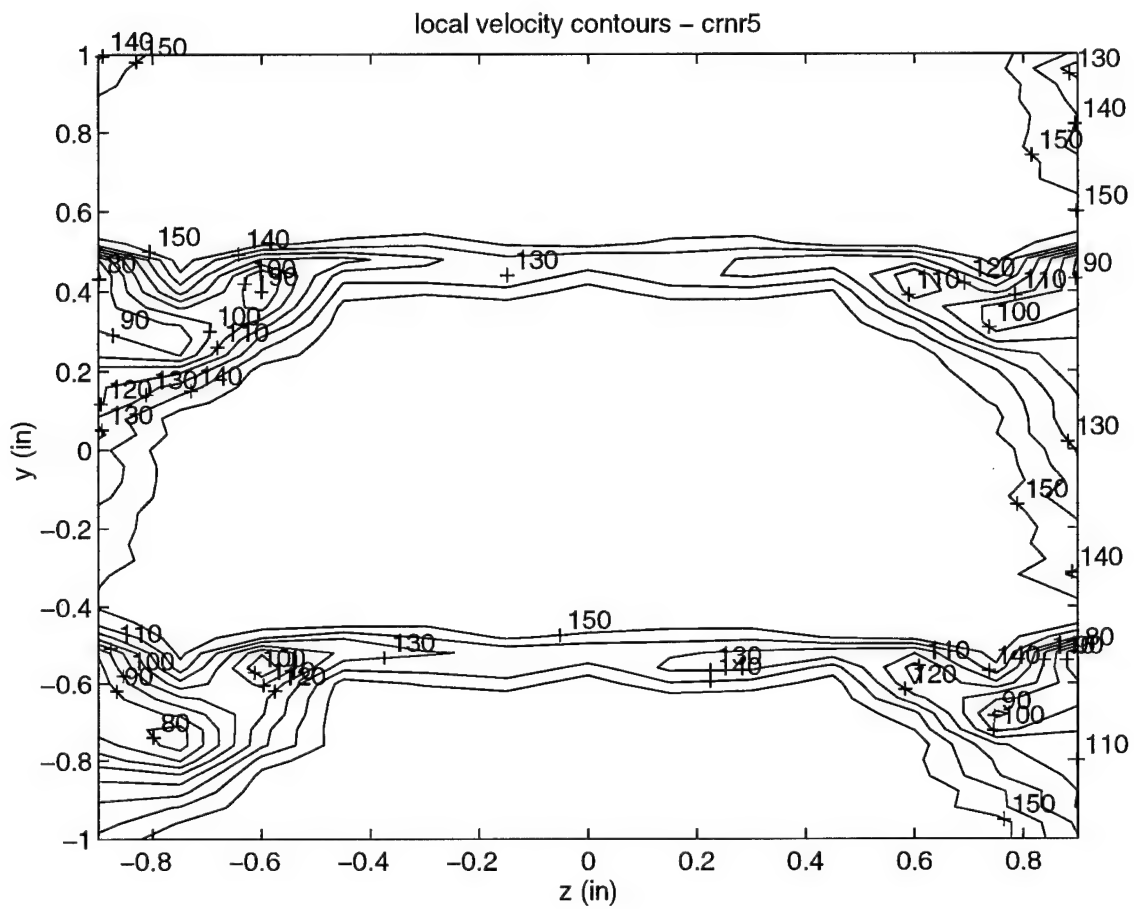


Figure 5-15. Local velocity contour plot $U_x = 164.3$ ft/s (Cren. Blade-no rotor)

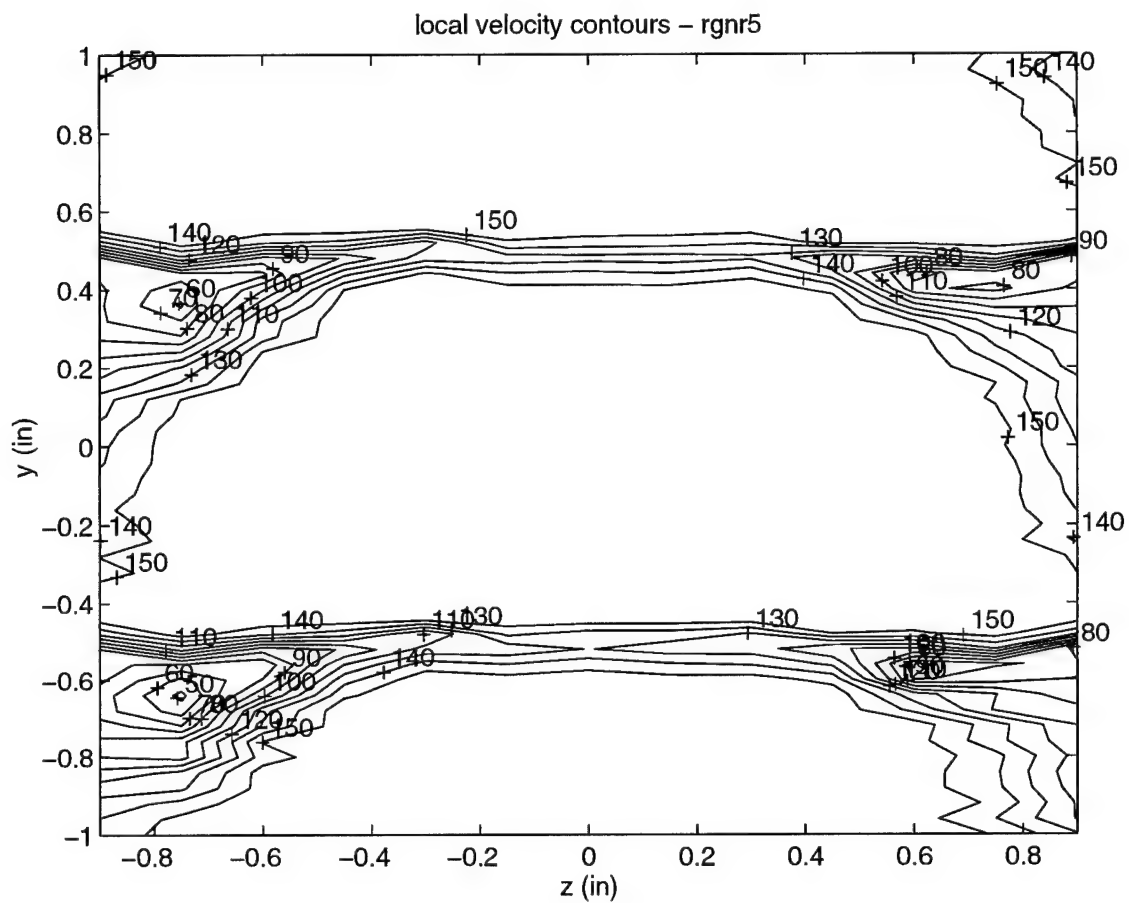


Figure 5-16. Local velocity contour plot $U_x = 164.3$ ft/s (Regular Blade-no rotor)

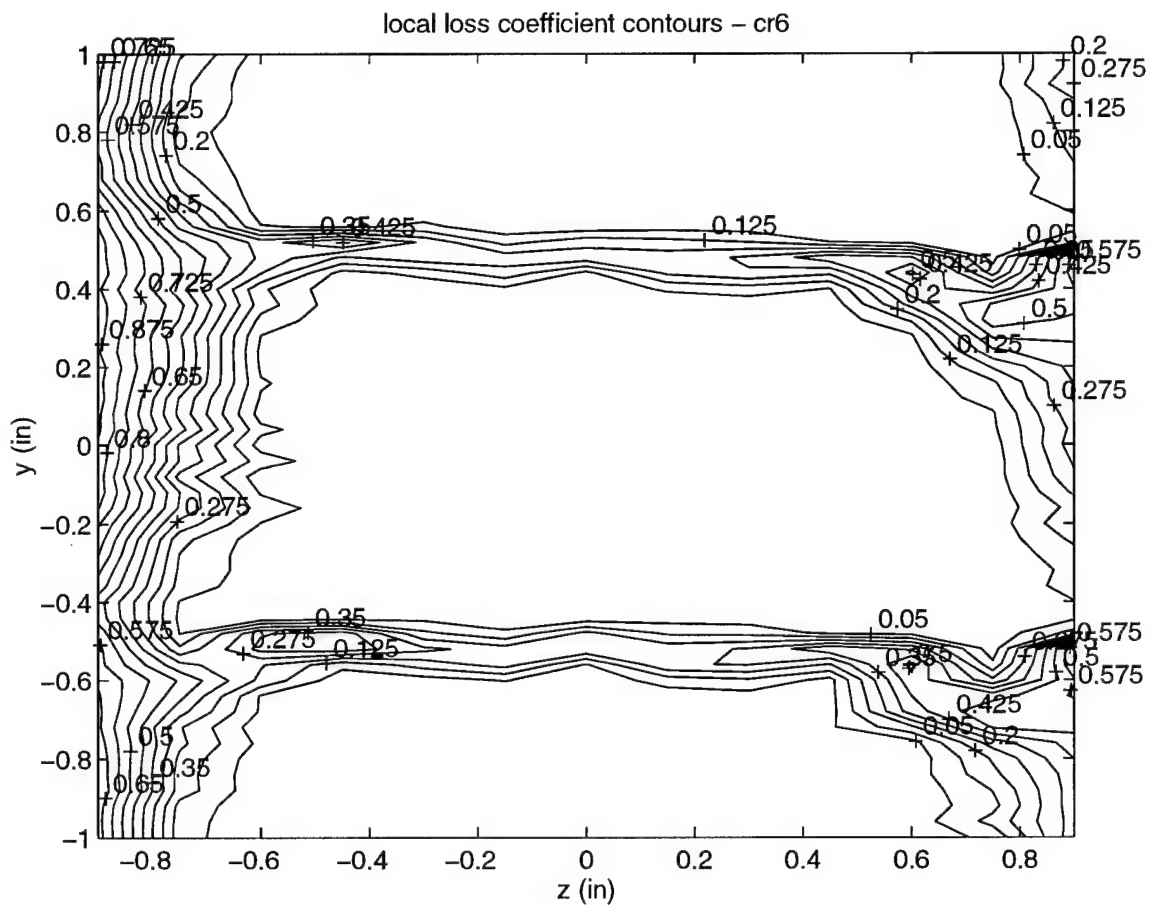


Figure 5-17. Local total pressure loss contour plot $\phi = 0.62$ (Crenulated Blade)

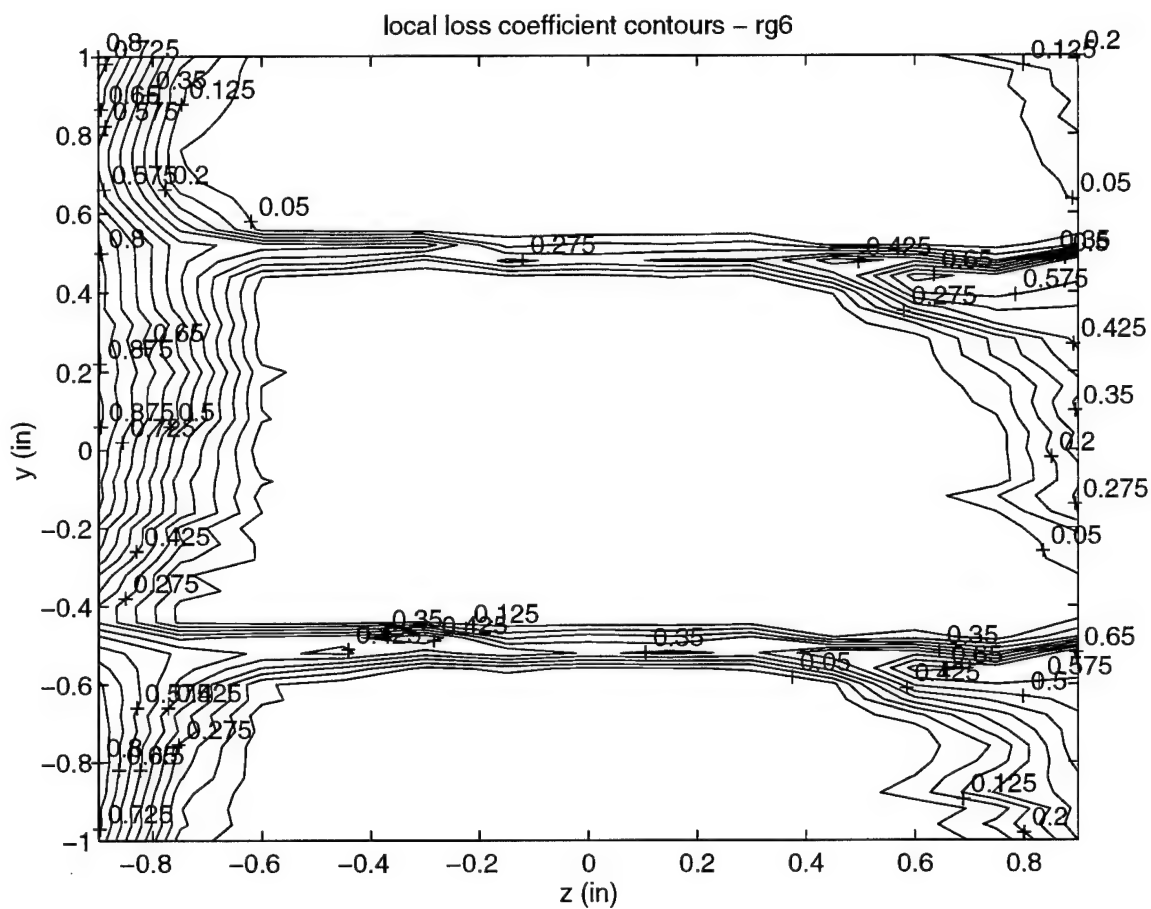


Figure 5-18. Local total pressure loss contour plot $\phi = 0.62$ (Regular Blade)

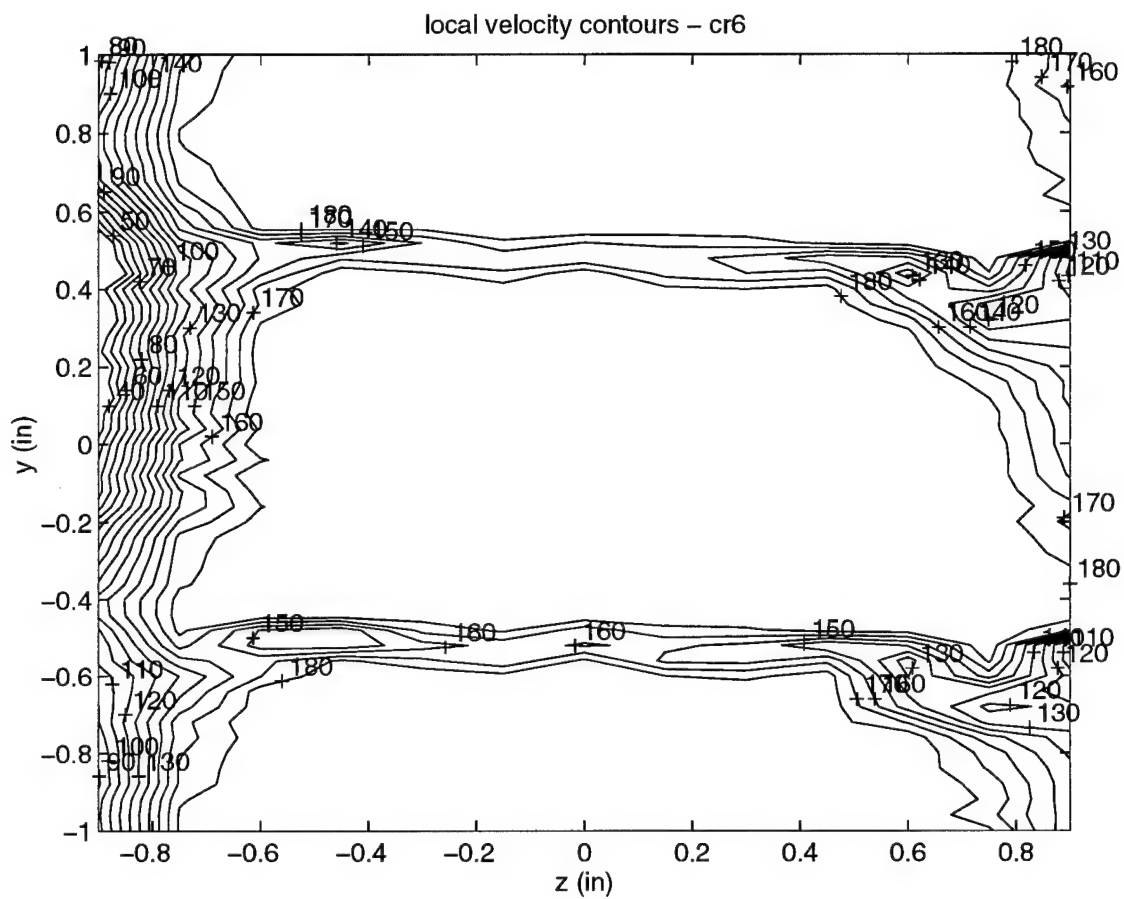


Figure 5-19. Local velocity contour plot $\phi = 0.62$ (Crenulated Blade)

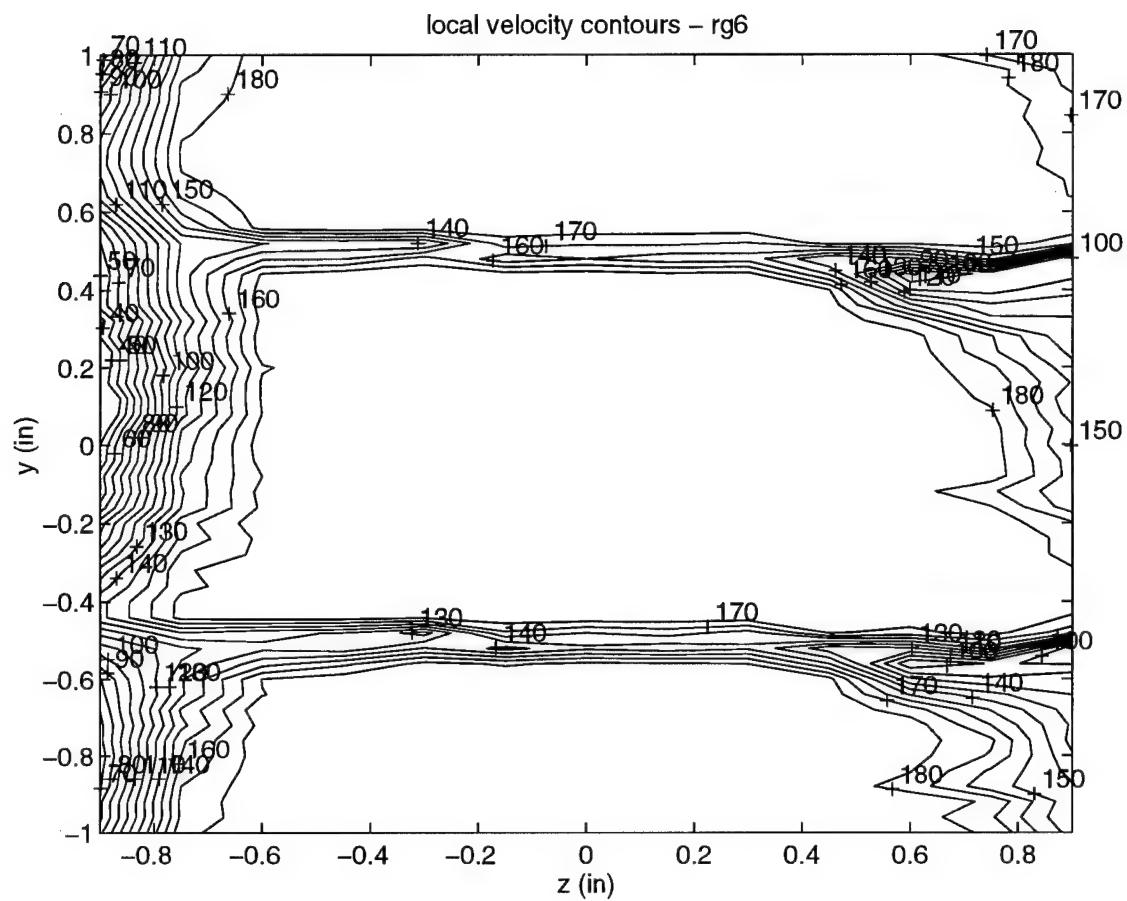


Figure 5-20. Local velocity contour plot $\phi = 0.62$ (Regular Blade)

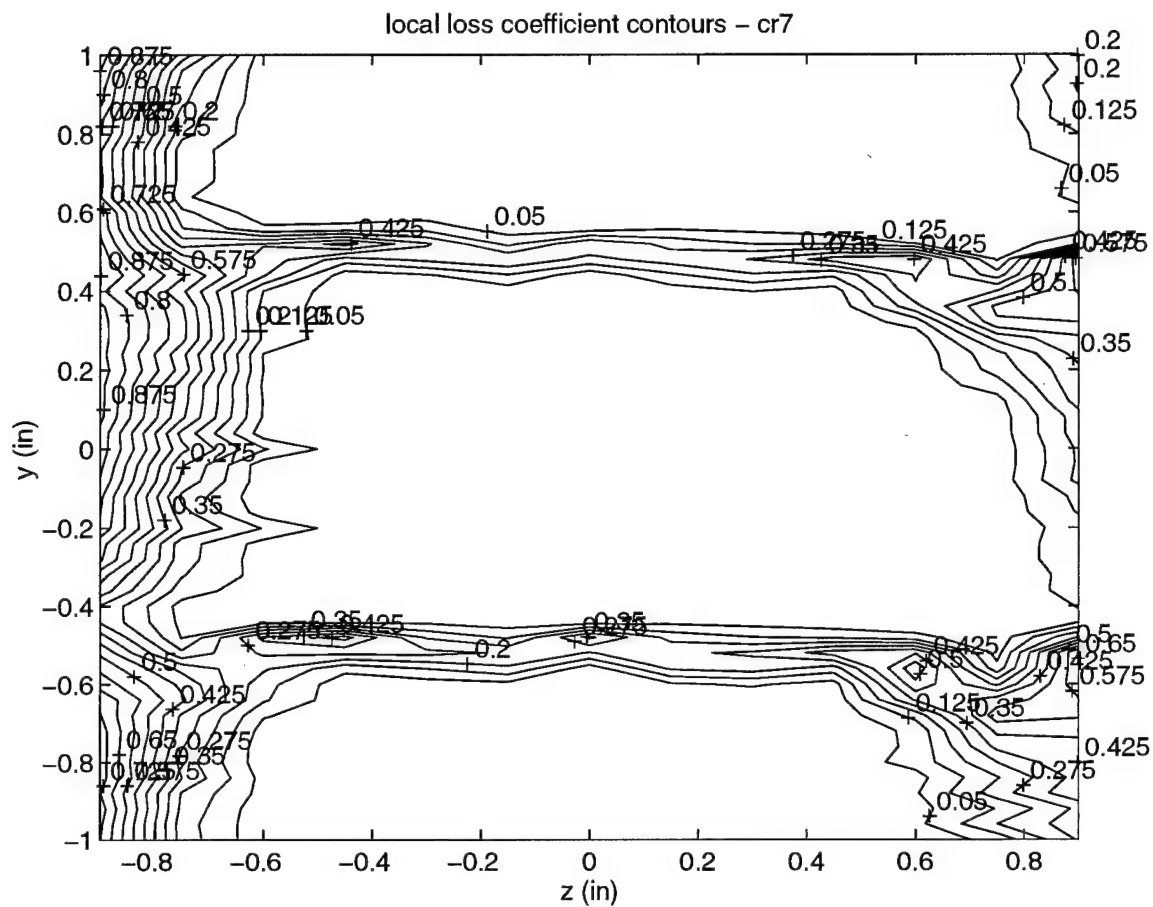


Figure 5-21. Local total pressure loss contour plot $\phi = 0.72$ (Crenulated Blade)

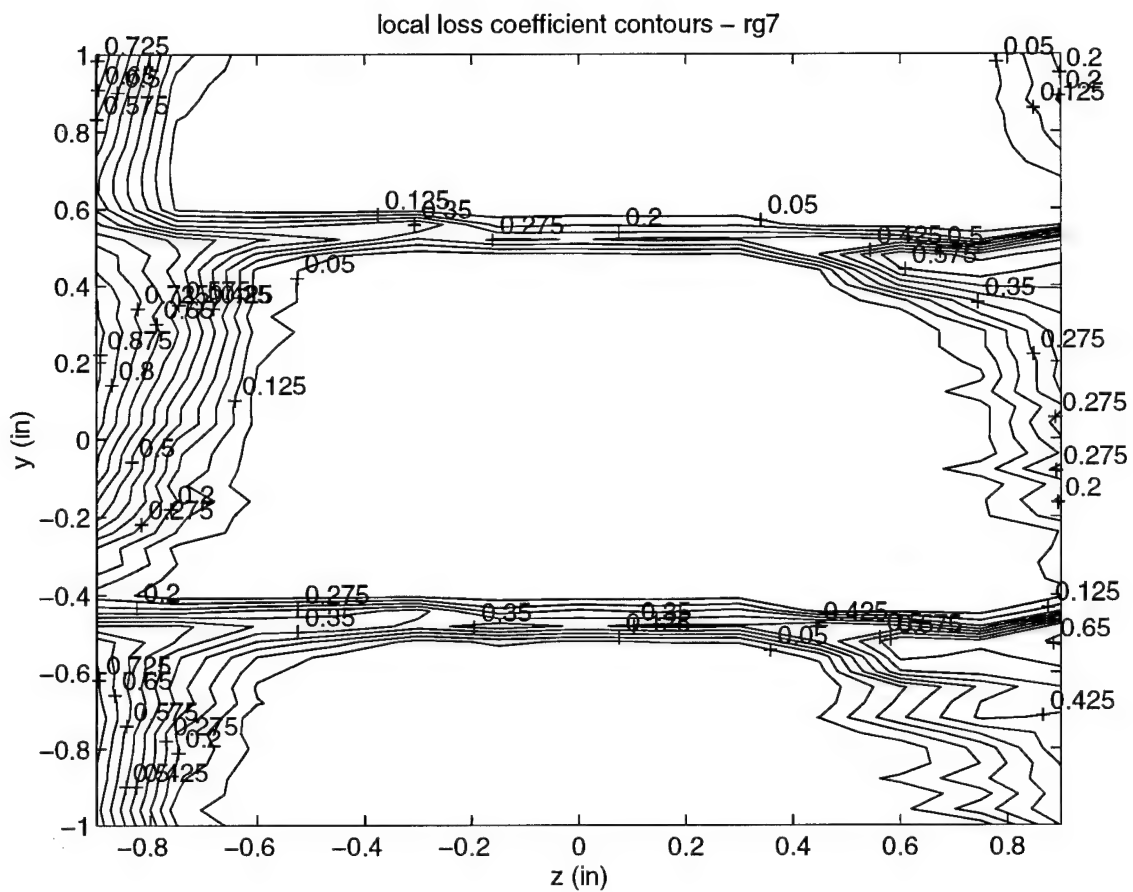


Figure 5-22. Local total pressure loss contour plot $\phi = 0.72$ (Regular Blade)

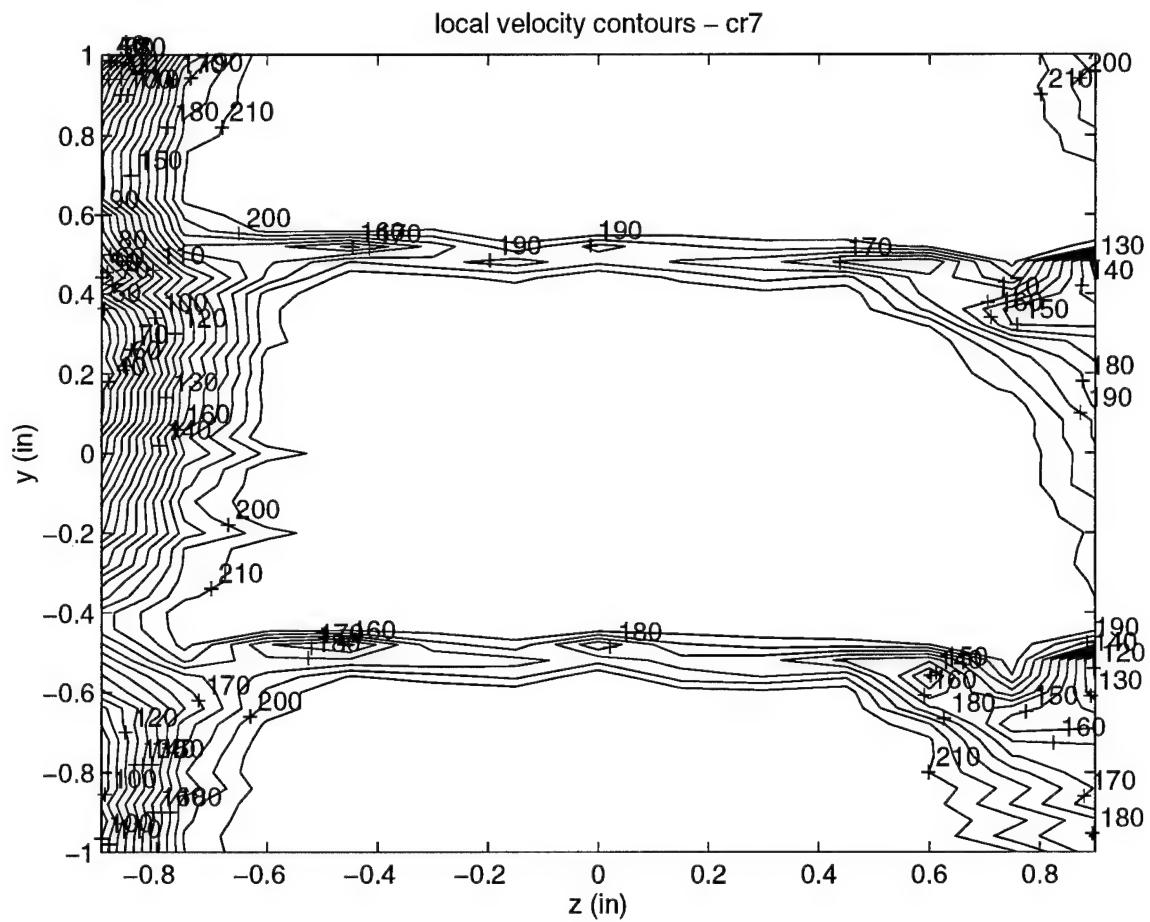


Figure 5-23. Local velocity contour plot $\phi = 0.72$ (Crenulated Blade)

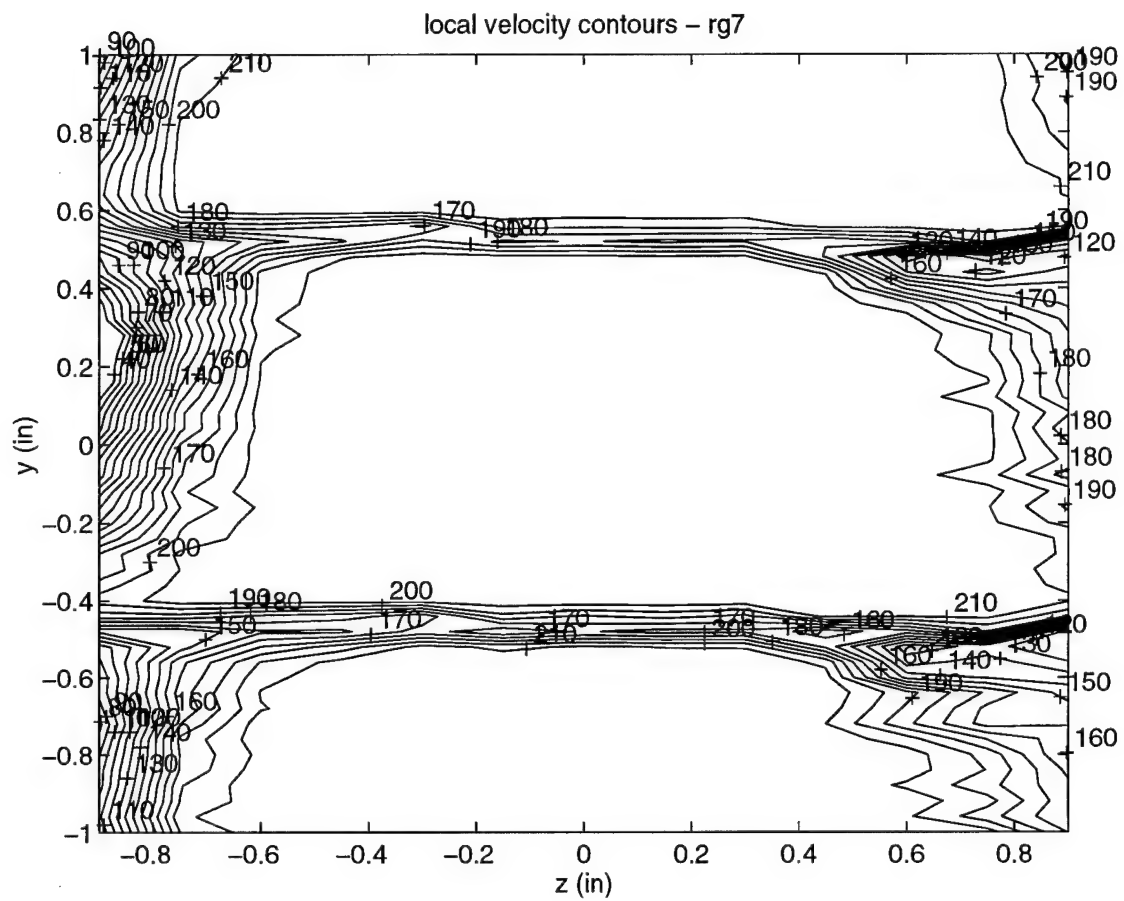


Figure 5-24. Local velocity contour plot $\phi = 0.72$ (Regular Blade)

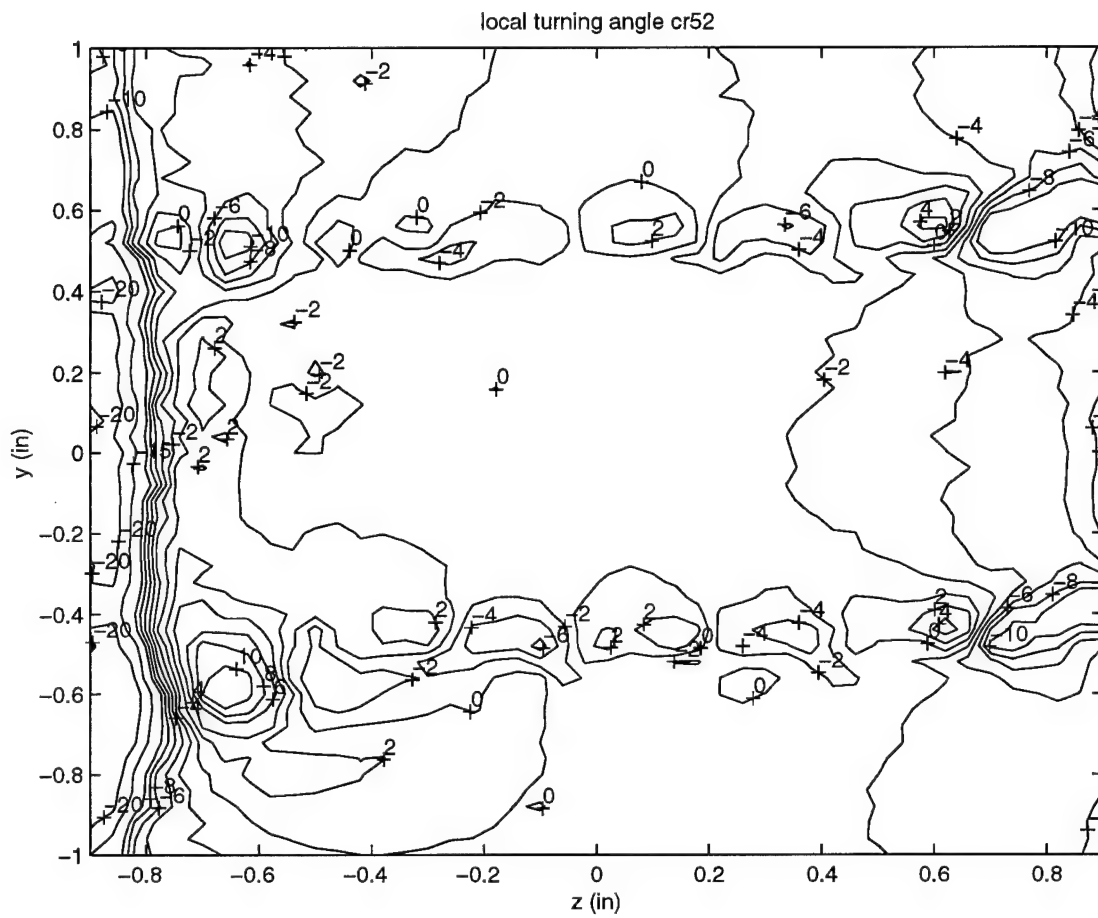


Figure 5-25. Local flow turning angle (degrees) $\phi = 0.52$ (Crenulated blade)

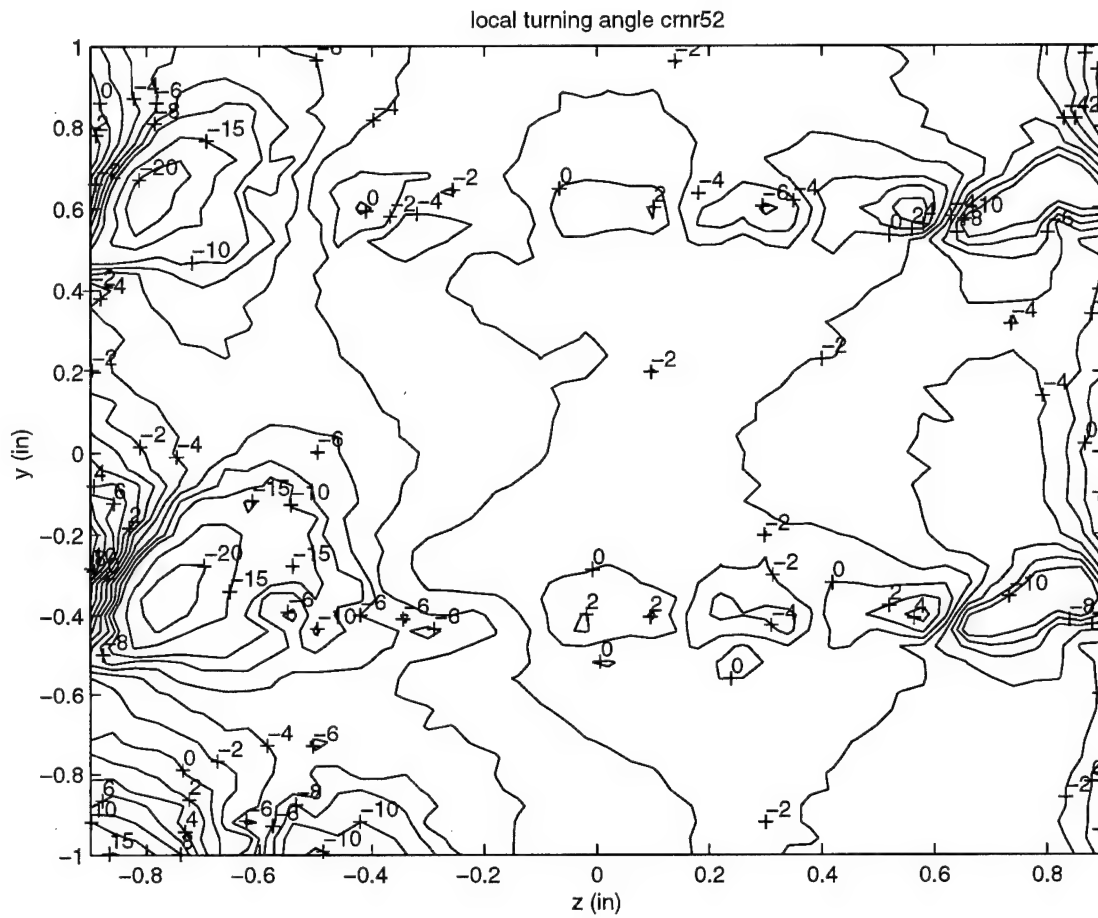


Figure 5-26. Local flow turning angle (degrees) $U_x = 164.3$ ft/s (Cren. blade-no rotor)

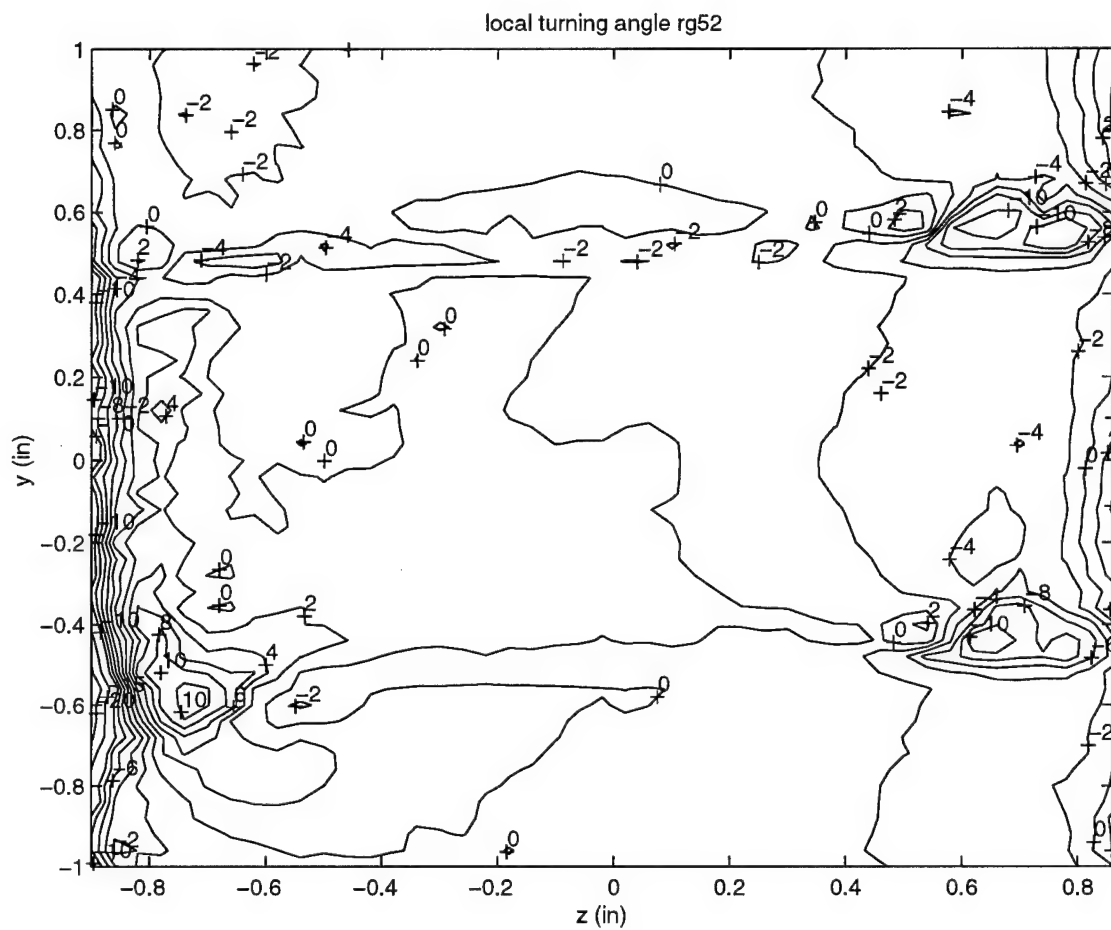


Figure 5-27. Local flow turning angle (degrees) $\phi = 0.52$ (Regular blade)

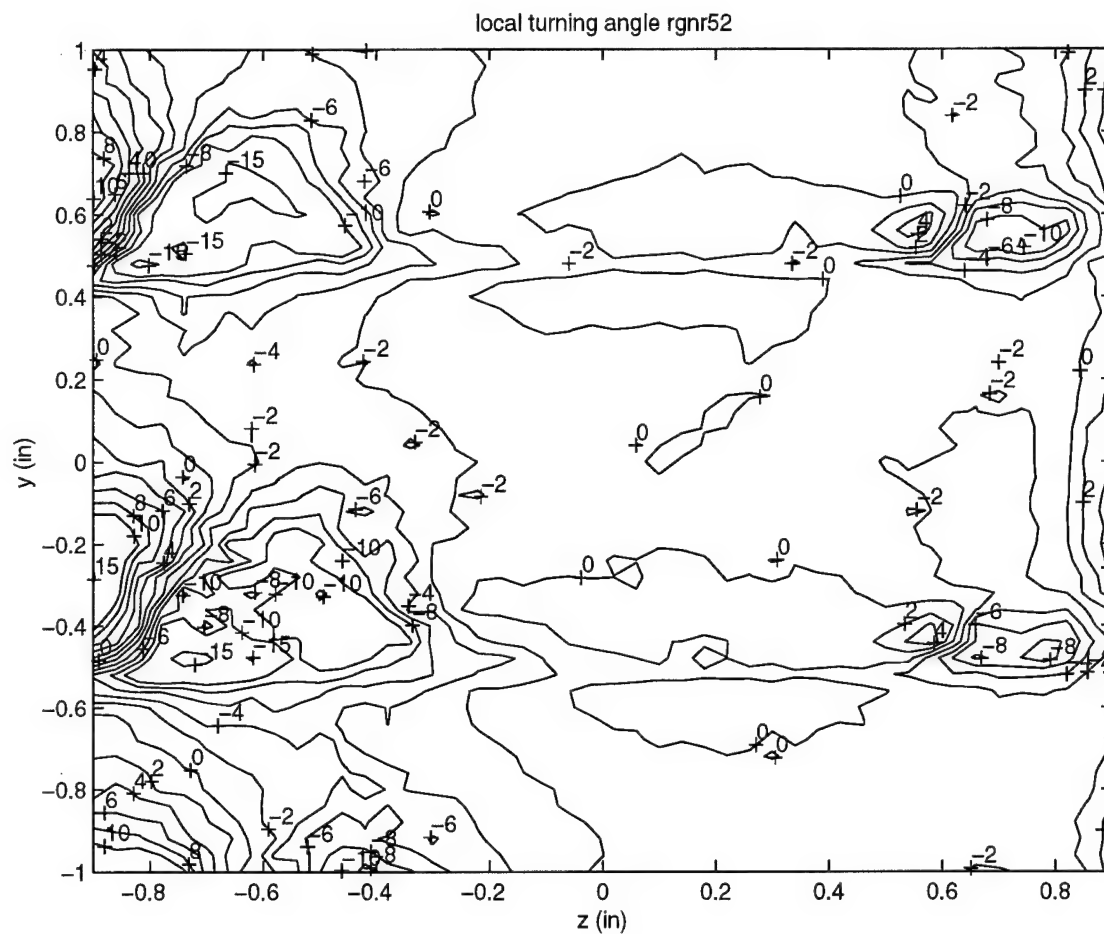


Figure 5-28. Local flow turning angle (degrees) $U_x = 164.3$ ft/s (Reg. blade-no rotor)

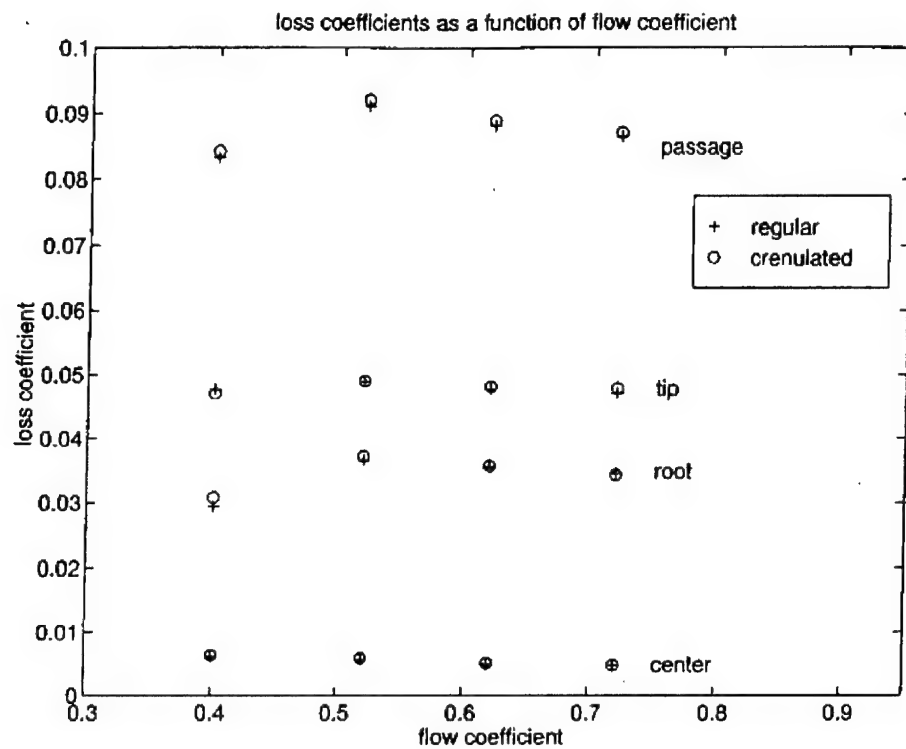


Figure 5-29. Total pressure loss coefficient comparisons (Region and passage)

Appendix A: Hotwire Information

Origin of the Governing Equations

The equations which govern the relationship between the voltage passing through the wires and the velocity of the local flowfield starts with basic heat transfer concepts.

Neglecting radiation and assuming that conduction of heat through the wire end supports was minimal, convective heat transfer follows the general relationship

$$\dot{q} = hA\Delta T \quad (\text{A-1})$$

Setting this equal to the electrical power required to keep the wire at a constant temperature begins the analysis, with the subscript w referring to hotwire values.

$$I^2 R_w = \frac{V_w^2}{R_w} = hA_w(T_w - T_a) \quad (\text{A-2})$$

The convection coefficient, h can be related to the Nusselt number

$$Nu = \frac{hD}{k} \quad (\text{A-3})$$

where D is the diameter of the wire and k is the wire's heat conduction coefficient.

Solving Eq (A-3) for h , inserting it into Eq (A-2) and rearranging,

$$Nu = \frac{V_w^2 D}{R_w k A_w (T_w - T_a)} \quad (\text{A-4})$$

From Bruun (1995), a general form of the Nusselt number may be written in terms of the Reynolds number

$$Nu = A + B Re^n \quad (\text{A-5})$$

where the Reynolds number is in this form:

$$Re = \frac{\rho V_{eff} D}{\mu} \quad (A-6)$$

Plugging this into Eq (A-5) and setting the two expressions for the Nusselt number equal to each other gives the encompassing relationship.

$$\frac{V_w^2 D}{R_w k A_w (T_w - T_a)} = A + B \left(\frac{\rho V_{eff} D}{\mu} \right)^n \quad (A-7)$$

Bruun (1995) explains that the anemometer output voltage V , is related to the wire voltage (for a balanced Wheatstone bridge) as

$$V = \frac{R_1 + R_L + R_w}{R_w} V_w \quad (A-8)$$

where R_L is the probe and cable resistance and R_1 is a portion of the bridge. For a constant temperature probe these values are assumed constant and will be rolled into the overall equation constants. The diameter, D and wire cylindrical area, A_w are also included in the constants as applicable. For this flow regime, as a by-product of the pressure measurements it was found that the density changes of the flow are negligible so ρ is also assumed constant in this analysis. This information gives the final form of the equation relating the output voltage to the velocity of the flow across the wire, V_{eff} .

$$V^2 = k(T_w - T_a) \left(A + B \left(\frac{V_{eff}}{\mu} \right)^n \right) \quad (A-9)$$

The temperature dependent values of k and μ are the same as DeCook (1991):

$$k = k_0 \left(\frac{T_f}{T_0} \right)^{0.8} \quad (A-10)$$

$$\mu = \mu_0 \left(\frac{T_f}{T_0} \right)^{\frac{3}{2}} \left(\frac{T_0 + S_1}{T_f + S_1} \right) \quad (\text{A-11})$$

with $k_0 = 0.242 \text{ J/(m}\cdot\text{s}\cdot\text{K)}$, $\mu_0 = 1.7456 \times 10^{-5} \text{ kg/(kg}\cdot\text{s)}$ both at $T_0 = 273.15 \text{ K}$. The film temperature T_f , not a universally agreed upon quantity, was defined in Bruun (1995) as simply

$$T_f = \frac{T_w + T_a}{2} \quad (\text{A-12})$$

with the ambient temperature of the fluid T_a used in all calculations. In order for different series of data to fall on a single line, Collis and Williams (1959) introduced a temperature loading factor to take into account varying temperature, modifying the original relationship.

$$Nu \left(\frac{T_f}{T_a} \right)^b = A + B \text{Re}^n \quad (\text{A-13})$$

Calibration Procedure

This procedure is a step by step checklist to provide guidance for future calibrations.

Many of the steps are taken directly from McMullan (1996) but there are several differences related to the implementation of the new software.

- Select the x-configuration hotwire desired.
- Measure the geometry of the hotwire, using Figure 4.2 as a guide. The following items are required for this process: straight edge, tape, overhead projector, protractor, pencil.
- Turn on the projector and shine it on the wall.

- Tape the sensor on the projector such that the outline of the probe is projected clearly on the wall. The side of the probe with TSI on it should be face up. Two prongs should appear in the image on the wall.
- Tape a piece of paper on the wall, centered about the image of the probe.
- With the image focused, trace the sensor wires and probe body onto the paper with the straight edge and pencil.
- Draw a line indicating the axis of the probe body. Measure the angles $\overline{\alpha_1}$ and $\overline{\alpha_2}$ relative to the axis.
- Plug in the vacuum pump. Make sure the air supply for the pressure system is on.
- Activate file c:\shark\cal shark.vi. The pressure acquisition system must be initialized and calibrated as per the procedure in Appendix B. Do that now.
- Turn on the data acquisition equipment for the hotwire by turning on the master switch at the top right of the HP 3052A module cabinet.
- Set up the IFA 100 for voltage acquisition.
 - On the back of the IFA 100, set the BRIDGE SEL switch to STD 1. Set the SENSOR switch to either wire or film. Connect the coaxial cables to the probe support on the TSI 1125 Probe Calibrator and the Probe Standard connections on the back of the IFA 100 (Channel 1-Channel 1 and Channel 2-Channel 2).
- Find the resistance of the cables and probe support for each channel. Same procedure for each channel.

- Put the shorting probe in to the probe support on the calibrator. This corresponds to the longest of the four prongs coinciding with the notch cut in the probe tube. The FAULT light on the IFA 100 will go out.
- Press the RES MEAS button on the front of the IFA 100. The NULL DSPL will light up.
- Null the digital reading on the front screen to zero by turning the OPERATE RES knob counterclockwise. Expect several revolutions and extreme resistance. A good technique is to overshoot slightly in the negative range and come back to zero.
- Press the RES MEAS button again. The resistance displayed is the cable resistance for that channel. Press enter to record this resistance.
- Insert the hotwire sensor into the probe support of the calibrator. This should correspond again to the longest of the four prongs matching the notch on the support tube, but there is also an inscribed line on the collar of the sensor that lines up (approximately) with the notch. Set the operating resistance of each wire. Same procedure for each wire.
 - Press the OPERATE RES button.
 - Turn the OPERATE RES knob clockwise until the operating resistance shown on the screen is the value given on the top of the sensor probe box for Recommended Oper Res. Hit enter.
 - Set the BRIDGE COMP for each sensor channel. Hit enter. For information on the BRIDGE COMP settings see IFA 100 manual.

- Set gain at 5.0. Hit enter.
- Set offset to 1.0. Hit enter.
- Turn on the calibrator's air supply system. With a velocity readout in the middle of the calibration range, place both Channels to RUN.
- Determine the cooling ratios.
 - Lower probe to within 0.05 in of the calibrator, centered over the nozzle.
 - Take measurements at several velocities and angles, hitting save after the voltage readout on the computer plots have settled out. Ranges of both are dependent on the flowfield expected. See Chapter 4 for values used in this research. For the angle readings, the value must be entered manually into the box marked P. Make sure you hit enter after typing in the value of the angle and before you save the data point. (When the desired range of data points was completed, the data was imported into Matlab where a least squares routine computed the values of A, B, n, and k for each wire.)
- Determine the temperature loading factors.
 - The heating equipment was inoperative during the time period of this research, but an alternate method worked equally well. Using the temperature of the air supply system, as is, at various times of the day worked well enough to give the needed temperature range. At zero angle incidence to the flow exiting the throat, at each temperature, take data points across the desired velocity range. Use a minimum of three temperatures for the different data runs with an overall range of

at least 6-7° K. (Another least squares MATLAB file using temperature

dependence in the equations and adding b as an unknown gave the proper results.)

- Calibration verification.

- Once all the calibration constants are evaluated, place the probe in the calibrator and take data points across the velocity and angle ranges expected in the flowfield. The obtained voltages can be plugged into transformation equations to compute the resulting angle and velocity information. The next section will explain this procedure in detail.

Hotwire Transformation Equations

Bruun (1995) describes four different methods to transform voltages back into velocity and angle information. The equations chosen for this research were selected because they are solely a function of the hotwire geometry. The following equations can be used to transform recorded voltages either from calibration verification or research data runs.

In general, the two velocity components are recovered using these equations:

$$U = \frac{\left[\frac{V_{e1}}{f_1(\alpha_1)} \right] g_2(\alpha_2) + \left[\frac{V_{e2}}{f_2(\alpha_2)} \right] g_1(\alpha_1)}{g_1(\alpha_1) + g_2(\alpha_2)} \quad (A-14)$$

$$V = \frac{\left[\frac{V_{e2}}{f_2(\alpha_2)} \right] - \left[\frac{V_{e1}}{f_1(\alpha_1)} \right]}{g_1(\alpha_1) + g_2(\alpha_2)} \quad (A-15)$$

where U and V are as depicted in Figure A-. The yaw functions f and g are defined as:

$$f(\bar{\alpha}) = (\cos^2 \bar{\alpha} + k^2 \sin^2 \bar{\alpha})^{\frac{1}{2}} \quad (\text{A-16})$$

$$g(\bar{\alpha}) = \frac{(1 - k^2) \cos^2 \bar{\alpha}}{\cos^2 \bar{\alpha} + k^2 \sin^2 \bar{\alpha}} \tan \bar{\alpha} \quad (\text{A-17})$$

The subscripts 1 and 2 refer to the designated wire with k being the applicable cooling ratio for that wire. V_{e1} and V_{e2} are computed by solving the governing equations with the recorded voltages input from data.

Appendix B: Pressure Rake Information

Pressure System Start-up

This procedure is presented in a step by step form to facilitate future use of the tunnel's updated software. This procedure is required for both pressure rake and hotwire data acquisition from the tunnel. For hotwire calibration procedures see Appendix A.

- The computer used is the Z-Station 510. With it turned on, double-click on the icon labeled "Shortcut to supper shark.vi". (Don't ask). While the system is booting up, plug in the vacuum pump, and ensure that the room's air supply valve is open. It's the X-shaped knob to the left of the large pressure indicator on the west wall over the desk. Turn on the nuDrive motor controller, POWER first, then ENABLE switch. The supper shark.vi graphic interface panel should be on the computer screen.

- Click on the white arrow at the left edge of the control bar at the top of the screen. The bar should shorten, with the arrow going black.

- Click on the PSI box in the upper left, blue panel. (blue box w/white outline will appear)

- Click on INIT. Open shark\new shark\shark 8400 init.txt. Yellow box will appear.

Ensure that the code that will appear in the yellow box is readable (i.e. command completed). If not re-initialize. System will return to blue panel w/white outline.

- Click on CAL. If you did the above, click "Yes, continue." When "command completed" appears, hit enter. Click on CANCEL.

- Below the blue panel in the upper left, hit the ENABLE button, then CONTINUE. Find location and name file desired for data run. Hit save.

- Click on the ENABLE DRIVE (OFF) button. It will turn on and show any deviation in the location of the probe (POS column) in relation to desired (left side XYZ column).

Red lights indicate position deviation. Click on the OFF buttons in between the XYZ indicators to make everything green. You should still be in MANUAL drive mode.

- Go to upper left blue panel and click on ACQ data. This only means that the system is picking up the signals and displaying them, not saving them. At this point, you can read the velocity at the inlet of the tunnel (v) and make any adjustments required. To the right of the blue control panel is a box marked PRES. This means that you will save data in the pressure rake format, either manually or automatically, your choice (coming up soon). If you click on that button, it will read HOTWIRE, which among other things will change the automatic array for data taking, and what items of information to save to file. Make sure you know what data you are about to pick up.

- Data is taken in one of two ways. If you are in MANUAL mode, one line of data will be taken every time you hit the SAVE button up in the FILE information area. This way if you have taken a data set and need to repeat a section of the points, you can drive the probe anywhere in the tunnel and take data at your discretion. Click on the MANUAL button and it will read AUTO. Now the system is slaved to the start/stop button and the index numbers indicated below that button. The reset button will put the counter (x+y) back to the number indicated in the start indicator window. For PRES the range 0-154 is the complete window for data acquisition if the rake is initially placed midway in the tunnel spanwise, 0.5 inches above blade 4. For HOTWIRE 0-2442 is the entire testing window if the probe is placed 0.5 inches above blade 4 as close to the root wall as

possible. Watch for bent probe holders that may limit your range. The one weakness of the automatic system is that the controller runs one axis at a time safely so there is one data point per column that is repeated as the probe transits the data field. After a data run look at the data lines or page through the array on the graphic interface and you'll see the redundancies.

When finished with the data run, click on the ACQ data button, then the STOP button. Now you're ready for data reduction. The following section explains the method used to compare pressure losses with McMullan (1996).

Passage Total Pressure Loss Calculations

This is included only to clarify the method used to compare numbers between researchers. Although seemingly obvious, the techniques of finite elements methods can produce varying answers.

Once the data set was taken as a .dat file it was input into c:\stugger\prdatred.xls of the left computer, which ultimately computes the information for both the ω contours and velocity contours, along with the information required to compute the region and passage loss coefficients. The appropriate information was copied and pasted to another spreadsheet so that the resultant file was a 51 row, 13 column data set (you should have four new data files - mass flows, ω *massflow, ω , and velocities). Rows 14-38 inclusive were determined to represent the passage between blades 4 and 5. When computing the passage loss coefficient, the values for mass flow are taken at a point, although representing a "box" about the point. At the extreme left and right columns of the data

field, this box extends beyond the data point field. Although there are many methods used in determining the proper weighting of values at the edge of a data field, in order to remain consistent with McMullan the full weighting of the mass flows at each point was included without any averaging of values to remain within the data field. The sum of ω *massflow divided by the sum of the mass flows gives the passage loss coefficient.

Appendix C explains the velocity and ω data file reduction for MATLAB.

Appendix C: Data Reduction Codes

This section explains the computer code used in determining various parameters used for the hotwire equations and accuracy measurements. There are many available alternatives to MATLAB that will do an equally fine job in the tasks described here. If you are well versed in other programs that do similar routines, read no further. This is included merely to show the means by which the data in my research may be reproduced.

Hotwire calibration

The first requirement for the calibration procedure was to take both angle and velocity ranges at whatever ambient temperature the air supply system is operating at that day (The determination of the cooling ratios is temperature independent). The following are lines of code with comments following the line.

Example filename: hwcal.m

```
global u1n u1t u2n u2t e1 e2 Tbot Tr theta vf y
```

This makes these variables available to the function (called later)

```
y=[];
```

This is the matrix generated by the calshark program. Empty here for simplicity, it's length is as long as the number of data points you want to calibrate with.

```
vf=y(:,1);
```

```
e2=y(:,2);
```

```
e1=y(:,3);
```

```
Tbot=y(:,4);
```

```
theta=y(:,5);
```

In order, the velocity of the flow, voltage from wire 2, voltage from wire 1 (it just happened that way), air supply ambient temperature, and flow angle (manually input)

```
a1bar=44/57.3;
```

```
a2bar=45/57.3;
```

Geometry of the wire, measured as described in Appendix A.

```
for i=1:length(y)
```

```
    a1(i)=a1bar+(theta(i)/57.3);
```

```
    a2(i)=a2bar-(theta(i)/57.3);
```

```
    u1n(i)=vf(i)*cos(a1(i));
```

```
    u1t(i)=vf(i)*sin(a1(i));
```

```
    u2n(i)=vf(i)*cos(a2(i));
```

```
    u2t(i)=vf(i)*sin(a2(i));
```

```
    Tr(i)=0.5*(523.15+Tbot(i));
```

```
end
```

This loop computes the flow angle relative to each wire and the corresponding normal and tangential velocities across each wire. The last line is the film temperature, which is the average of the ambient temperature of the fluid and the temperature of the wire.

Normal operating temperature of the hotwire used in this research was 250° C, and was considered constant throughout operation.

```
x=leastsq('fun',[1,1,0.5,0.2],[1 0 0 0 0 0 0 0 0 0 0 0 0 0 1000 0 0])
```

This calls the least squares routine using the file fun.m to locate the equations in question. The length four vector are initial guesses and the second vector is a setup to monitor the residual of the equations as MATLAB crunches to a solution using 1000 iterations to come to a solution. Below is the description of the file fun.m

Example filename:fun.m

```
function q=fun(p)

global u1n u1t u2n u2t e1 e2 Tbot Tr theta vf y

a=p(1);b=p(2);n=p(3);k=p(4);

q=zeros(length(y),1);

for j=1:length(y)

q(i)=(a+b*((u1n(i)^2+k^2*u1t(i)^2)^0.5)^n)-((e1(i)/5+1)^2);

%q(i)=(a+b*((u2n(i)^2+k^2*u2t(i)^2)^0.5)^n)-((e2(i)/5+1)^2);

end
```

Since both wires are independent of each other, calculation of the constants for each wire was conducted separately. The first q(i) line is read by the function and returns the values of the four constants a, b, k, n. These are for the first wire. The percent sign in front of the second q(i) line masks the line's information and is not read by the program. In order to get the second wire's constants move the percent sign to the first q(i) line and the return will be the four constants for wire two. Note that the voltages for both wires have been recomputed to their raw values (The IFA 100 was set with a gain of 5 and offset of 1). Now it's time to include temperature dependence.

Example filename: tempload.m

```
global u1n u1t u2n u2t e1 e2 Tbot Tr theta vf y

y=[];

vf=y(:,1);

e2=y(:,2);

e1=y(:,3);

Tbot=y(:,4);

theta=y(:,5);

a1bar=44/57.3;

a2bar=45/57.3;

for i=1:length(y)

    a1(i)=a1bar+(theta(i)/57.3);

    a2(i)=a2bar-(theta(i)/57.3);

    u1n(i)=vf(i)*cos(a1(i));

    u1t(i)=vf(i)*sin(a1(i));

    u2n(i)=vf(i)*cos(a2(i));

    u2t(i)=vf(i)*sin(a2(i));

    Tr(i)=0.5*(523.15+Tbot(i));

end
```

All this should look familiar. The only difference is that the matrix y is probably a pasted set of data points taken at different times to ensure a temperature range from the air supply.

```
x=leastsq('fun1',[.1],[1 0 0 0 0 0 0 0 0 0 0 0 1000 0 0])
```

Again this looks familiar but calls the function with fun1.m as the reference file. The only initial guess is the temperature loading constant, with the remaining parameters held constant. This is a product of choice. The small temperature changes associated with the flow regime studied didn't warrant the added complexity of updating the a, b, n constants with the small changes associated with viscosity or thermal conductivity. Bruun (1995) notes that any reduction in accuracy with this method is negligible in most practical hotwire applications.

Example filename: fun1.m

```
function q=fun1(p)

global u1n u1t u2n u2t e1 e2 Tbot Tr theta vf y

t=p(1)

q=zeros(length(y),1);

for j=1:length(y)

q(i)=(a1+b1*((u1n(i)^2+k1^2*u1t(i)^2)^0.5)^n1)-

((e1(i)/5+1)^2)*(Tr(i)/Tbot(i))^t;

%q(i)=(a2+b2*((u2n(i)^2+k2^2*u2t(i)^2)^0.5)^n2)-

((e2(i)/5+1)^2)*(Tr(i)/Tbot(i))^t;

end
```

This again looks familiar with the same procedure as before to get the temperature loading constants for each wire. To keep in the spirit of generality the a, b, n, k constants

have been left in their variable form. Obviously the values previously computed from fun.m would be input in the appropriate locations.

Finally, the verification for the hotwire constants involves simply placing the probe in the calibrator and running a series of angles and velocities across the hotwire. This data set is placed in the following program, which inverts the equations developed in Appendix A and uses the yaw parameters to calculate the predicted angles and velocities. These are simply checked from the known inputs for comparison.

Example filename: calver.m

```
y=[];
vf=y(:,1);
e2=y(:,2);
e1=y(:,3);
Tbot=y(:,4);
theta=y(:,5);
a1bar=44/57.3;
a2bar=45/57.3;
for i=1:length(y)
    Tr(i)=0.5*(523.15+Tbot(i));
end
a1bar=44/57.3;
a2bar=45/57.3;
a1=
```



```

b1=

k1=

n1=

t1=

a2=

b2=

k2=

n2=

t2=

f1=((cos(a1bar))^2+k1^2*(sin(a1bar))^2^0.5;

f2=((cos(a2bar))^2+k2^2*(sin(a2bar))^2^0.5;

g1=((((cos(a1bar))^2+k1^2*(1-k1^2))/f1^2)*(tan(a1bar);

g2=((((cos(a2bar))^2+k2^2*(1-k2^2))/f2^2)*(tan(a2bar);

for j=1:length(y)

    Ve1(j)=((((e1(j)/5)+1)^2*(Tr(j)/Tbot(j))^t1-a1)/b1)^(1/n1);

    Ve2(j)=((((e2(j)/5)+1)^2*(Tr(j)/Tbot(j))^t2-a2)/b2)^(1/n2);

    U(j)=((Ve1(j)/f1*g2+(Ve2(j)/f2)*g1)/(g1+g2);

    V(j)=((Ve2(j)/f2)-(Ve1(j)/f1))/(g1+g2);

    Vf1(j)=(U(j)^2+V(j)^2)^0.5;

    theta1(j)=57.3*atan(V(j)/U(j));

end

```

These equations are explained in Appendix A and in Bruun (1995). A couple of important tips may be useful. Watch out for local minima when computing by checking the residual and make sure it's as low as it can get. After the program arrives at a value, manually pick a value and monitor the residual as you change b . Also, measure the skew angle of the probe with the x-axis of the tunnel. Probes are often bent and so when graphed, the entire flowfield will look like its leaning in one direction. If you place a straight edge along the corner of the throat area you can also see that the exit axis is not entirely aligned with the axial direction of the throat. When reducing data I found it easier to put the skew angle in MATLAB when plotting and not in the general program (approximately 3°).

Appendix D: Equipment Listing

Subsystem	Model Number/Description
Pressure Measurement	Pressure Systems Inc. Model 8400 Pressure Scanner (20 kHz maximum sample rate) Model 8415 Scanner Interface Unit Model 8420 Scanner Digitizer Unit Model 8440 Analog Input Unit Model 8433 Pressure Calibration Unit (1 psid) Model 8433 Pressure Calibration Unit (5 psid) Certified Standard Transducer (0.2-18 psi range, 0.00001 psi accuracy)
	Transducer block P/N 32RG-0301 (1 psid range, 0.0005 psi accuracy)
	Transducer block P/N 3201B (1 psid range, 0.0005 psi accuracy)
	Transducer block P/N 3205B (5 psid range, 0.0005 psi accuracy)
	Pressure Rake (5 ports spaced 0.381 cm) (0.158 cm OD, 0.1016 cm ID)
	Endevco Model 4428A Digital Barometer (13.00-15.51 psia range, 0.005 psi accuracy)
	ALC-TEC OME 25S Vacuum Pump
	TSI Model IFA 100 System Intelligent Flow Analyzer Model 150 Anemometer Modules (2) Model 157 Signal Conditioner Modules (2)
	TSI Model 1241-T1.5 X-Wire Sensor
	TSI Model 1155-36 Probe Support
	TSI Model 1125 Probe Calibrator
Velocity and Temperature Measurement	

	Omega T-type Thermocouples (copper-constantan, 0.3° C accuracy)
	Omega DP25-TC Programmable Digital Thermocouple Meters (3)
Traverse Control	nuLogic, Inc., pcStep 4A Stepper Controller
	Oriental Motor Company Stepper Motors (2) (400 steps/revolution resolution)
Central Computer	Zenith Z-Station 510 (486-50 processor) National Instruments Model ATGPIB General Purpose IEEE Interface Board
	Software Labview operating with National Instruments MIO-16 Data Acquisition Board
Rotor System	Baldor CDP-3450 Motor (1 HP DC permanent magnet, 2500 rpm)
	KB electronics DC controller KBPC-240D
	Cole-Palmer Instrument Co. 08210 Series Pistol Grip Phototachometer (50 - 20,000 rpm, ± 1.0 rpm)

Vita

Captain Barry Warren St. Germain was born on 12 October 1965 in Leominster, Massachusetts. He graduated from North Middlesex Regional High School, Townsend, Massachusetts in 1983. In 1987, he earned a Bachelor of Science degree in Aerospace Engineering from Purdue University and was commissioned a Second Lieutenant in the United States Air Force.

Captain St. Germain entered Undergraduate Pilot Training at Williams Air Force Base (AFB), Arizona and, following graduation, remained there as a T-38 Instructor Pilot in the 97th Flying Training Squadron. In 1993, he moved to Dover AFB, Delaware where he flew the C-5 Galaxy as a member of the 3d Airlift Squadron, and earned his Master of Science degree in the Aeronautical Sciences from Embry-Riddle University.

In 1996, Captain St. Germain was assigned to the Air Force Institute of Technology, Wright-Patterson AFB, Ohio to pursue a Master of Science in Aeronautical Engineering as a precursor to his attendance in Class 98A at the Air Force Test Pilot School, Edwards AFB, California.

Permanent Address: 8 Ryan Rd
West Townsend, MA 01474

REPORT DOCUMENTATION PAGE			Form Approved OMB No. 0704-0188	
Public reporting burden for the collection of information is estimated to average 1 hour per response, including the time for reviewing instructions, searching existing data sources, gathering and maintaining the data needed, and completing and reviewing the collection of information. Send comments regarding this burden estimate or any other aspect of this collection of information, including suggestions for reducing this burden, to Washington Headquarters Services, Directorate for Information Operations and Reports, 1215 Jefferson Davis Highway, Suite 1204, Arlington, VA 22202-4302, and to the Office of Management and Budget, Paperwork Reduction Project (0704-0188), Washington, DC 20503.				
1. AGENCY USE ONLY (Leave blank)		2. REPORT DATE March 1999		3. REPORT TYPE AND DATES COVERED Final Master's Thesis
4. TITLE AND SUBTITLE TIP VORTEX AND CRENULATION EFFECTS IN A COMPRESSOR CASCADE WITH MOVING ENDWALL			5. FUNDING NUMBERS	
6. AUTHOR(S) St. Germain, Barry W., Captain, USAF				
7. PERFORMING ORGANIZATION NAME(S) AND ADDRESS(ES) Air Force Institute of Technology WPAFB, OH 45433-6583			8. PERFORMING ORGANIZATION REPORT NUMBER AFIT/GAE/ENY/99M-02	
9. SPONSORING / MONITORING AGENCY NAME(S) AND ADDRESS(ES) Dr. W. Copenhaver WL/POTF			10. SPONSORING / MONITORING AGENCY REPORT NUMBER	
11. SUPPLEMENTARY NOTES				
12a. DISTRIBUTION / AVAILABILITY STATEMENT Approved for public release; distribution unlimited			12b. DISTRIBUTION CODE	
13. ABSTRACT (Maximum 200 words) The effects of changing Reynolds number and flow coefficients on the velocity and pressure flowfields within a linear cascade with moving endwall were investigated in this experimental thesis. All flowfield measurements were taken at a constant compressor blade tip gap clearance of 1.0 % chord and endwall speed of 318.6 ft/s (97.1 m/s), with flow coefficients of 0.40, 0.52, 0.62 and 0.72. All data acquisition occurred in a plane 23 % chord downstream of the trailing edge plane of the linear cascade. Hotwire probes determined the complete passage, three-dimensional flowfield behind both crenulated and regular blade geometries. Vector plots showed that the mid-span crenulations aligned the flow axially, increasing the wake mixing and reducing the spanwise flow evident in the regular blade's wake region. A total pressure rake measured the pressure flowfield behind the blades, showing that the crenulated blade geometry produced larger, less intense areas of total pressure loss than for the regular blades. Overall, the crenulated blade tested showed equal passage total pressure losses, increased wake mixing, reduced wake deficit and a reduced flow turning angle compared to a regular blade of similar overall dimensions.				
14. SUBJECT TERMS axial flow compressor blades, cascades, compressor losses, tip clearance, tip leakage vortex velocity vectors, vortices			15. NUMBER OF PAGES 120	
			16. PRICE CODE	
17. SECURITY CLASSIFICATION OF REPORT UNCLASSIFIED	18. SECURITY CLASSIFICATION OF THIS PAGE UNCLASSIFIED	19. SECURITY CLASSIFICATION OF ABSTRACT UNCLASSIFIED	20. LIMITATION OF ABSTRACT UL	